

Production of Highly-Ordered Nanocellular Foams by UV-Induced
Chemical Foaming with Self-Assembled Block Copolymers

Podchara Rattanakawin

2022

Table of Contents

Chapter 1 General Introduction	4
1.1 Polymer foam introduction	4
1.2 Nanocellular polymer foams	6
1.2.1 Nanocellular foam properties	6
1.2.2 Progress and challenges in nanocellular polymer foam production	8
1.3 Thesis overview and objectives	11
1.4 Reference	15
Chapter 2 Synthesis of High Molecular Weight Photocleavable Block Copolymer for UV-Induced Chemical Foaming	22
2.1 Introduction	22
2.2 Methods	23
2.2.1 Materials	23
2.2.2 Homogeneous polymerization of PS-b-PtBMA by TERP	24
2.2.3 Emulsion polymerization of PMMA-b-PtBA	25
2.2.4 ¹ H NMR Analysis	27
2.2.5 SEC measurement	30
2.2.6 DSC measurement	30
2.3 Results and Discussion	30
2.3.1 Homogeneous TERP polymerization of PS-b-PtBMA	30
2.3.2 Emulsion TERP polymerization of PMMA-b-PtBA Under Photo-Irradiated Conditions	32
2.3.3 Emulsion TERP polymerization of PMMA-b-PtBA Under Azo-Initiated Thermal Conditions	35
2.4 Conclusion	39
2.5 References	40
Chapter 3 Preparation of Highly-Ordered Nanocellular Foams by UV-induced Chemical Foaming from Self-Assembled PMMA-b-PtBA	42
3.1 Introduction	42
3.2 Methods	44

3.2.1 Sample preparation	44
3.2.2 Foaming of the self-assembled PMMA-b-PtBA film	44
3.2.3 Characterization of the self-assembled morphology	44
3.2.4 Thermal property measurement for determining a foaming condition	45
3.2.5 Characterization of the cell structure	46
3.2.6 Change of the chemical structure before and after foaming	46
3.2.7 Evaluation of the density of the polymer foam.....	46
3.2.8 Rheological properties measurement	47
3.2.9 UV penetration depth measurement.....	47
3.3 Results and Discussion	47
3.3.1 Self-assembly of PMMA-b-PtBA by solution casting.....	47
3.3.2 Suitable foaming conditions	49
3.3.3 Formation of the PMMA-b-PtBA nanocellular foams.....	51
3.2.4 Effect of PAG concentration on the cell structure	55
3.2.5 Effect of foaming temperature on the cell structure.....	56
3.2.5 Estimation of the UV penetration depth	61
3.4 Conclusion	63
3.5 References	64
Chapter 4 Effects of Self-Assembled Block Copolymer Morphology on Nanocellular Foams Prepared by UV- induced Chemical Foaming	67
4.1 Introduction	67
4.2 Methods	68
4.2.1 Materials	68
4.2.2 Foaming of the self-assembled PMMA-b-PtBA film	69
4.2.3 Characterization of the self-assembled morphology	69
4.2.4 Characterization of the cell structure	70
4.2.5 Isobutene gas generation.....	70
4.2.6 Density and expansion ratio evaluation	70

4.3 Results and Discussion	71
4.3.1 Effect of the self-assembled morphology on the cell structure	71
4.3.2 Effect of the molecular weight on the cell structure	75
4.4 Conclusion	80
4.5 References	81
Chapter 5 General Conclusion	85
5.1 Summary of Chapters	85
5.2 Future Prospects	86
5.3 References	89
Appendix: Supporting Information.....	91
A.1 Matlab Codes for the SEC peak normalization.....	91
A.2 Matlab Codes for the TEM image FFT analysis	92
A.3 Estimation of the gas pressure inside the cells.....	95
A.4 References.....	97
List of Figures and Tables	98
Figures	98
Tables	102
Acknowledgement	103
List of Achievements.....	105
Publication.....	105
Peer-reviewed Full Papers	105
Peer-reviewed International Conference Proceedings	105
Presentation	106
International Conferences.....	106
Domestic Conferences.....	106
Awards.....	106

Chapter 1 General Introduction

1.1 Polymer foam introduction

Polymer foams are materials where a gaseous phase is dispersed within a polymer matrix. By incorporating the gaseous phase, polymer foams have various properties, including being lightweight,¹ low thermal conductivity,^{2,3} high impact resistance,^{4,5} and high sound isolation.⁶⁻⁸ Because of these features, polymer foams have been used for a wide array of applications incorporating all aspects of our daily life. For instance, expanded polystyrene foams (EPS) and rigid polyurethane (PU) foams have been used as thermal insulating materials for building and construction applications.⁹⁻¹³ Flexible polyurethane foams can be found in various consumer products, such as clothing, shoes, sporting equipment, and furniture cushions.¹⁴ Polypropylene (PP) foams have been used in the automotive and home electrical appliance sector as high-service temperature insulation materials.^{15,16} Engineering plastic foams such as polyimide foams (PI) have been used in the aerospace and aircraft industry due to their thermal stability.¹⁷

Polymer foams are produced mainly by two schemes, chemical foaming and physical foaming, depending on how the gaseous phase in the polymers is generated, as illustrated in Figure 1.1. In the chemical foaming, chemical blowing agents (CBA) are added to the polymer. These chemical blowing agents create gas upon thermal decomposition or chemical reactions and expand the polymer matrix. Chemical blowing agents could be generally classified as inorganic and organic blowing agents. Inorganic blowing agents include carbonates such as sodium bicarbonate (NaHCO_3) producing carbon dioxide (CO_2), and hydrides, such as sodium borohydride (NaBH_4) producing hydrogen (H_2).^{14,18} Organic blowing agents are the majority of the CBA used in the industry due to their good dispersibility in the polymer and stable gas output.¹⁴ Commonly used organic blowing agents include isocyanate and water systems which produces CO_2 at room temperature, and Azo-compounds such as Azodicarbonamide (ADCA) and Azobisisobutyronitrile (AIBN), which produces nitrogen (N_2), carbon monoxide (CO), carbon dioxide (CO_2), and ammonia (NH_3) upon heating.¹⁸

In physical foaming, non-reactive gases, e.g., carbon dioxide, nitrogen, and isobutene, are injected directly in the polymers. The physical foaming process involves 4 major steps: (1) saturation of physical blowing agent (PBA) in the polymer, (2) cell nucleation induced by phase separation of the PBA, (3) cell growth, and (4) cell stabilization.¹⁹ The gas saturation process is done by dissolving the PBA into the polymer at high pressure and a defined temperature depending on the glass transition temperature and the melting temperature of the polymer to be foamed.²⁰ During the saturation, the physical blowing agent also acts as a plasticizer and allows the process to be operated at low temperatures. After the gas saturation process, a sudden decrease in pressure or increase in temperature induces the phase separation of the gaseous phase resulting in cell nucleation. Further gas diffusion causes the cell growth from the nuclei, gradually forming the foam structure. These foam structures are then stabilized by cooling the polymer matrix. Physical foaming is more widely used in industries when compared to chemical foaming due to recyclability and toxicity free.^{14,20} However, physical foaming requires a special molding machine that can handle processing at high pressure.

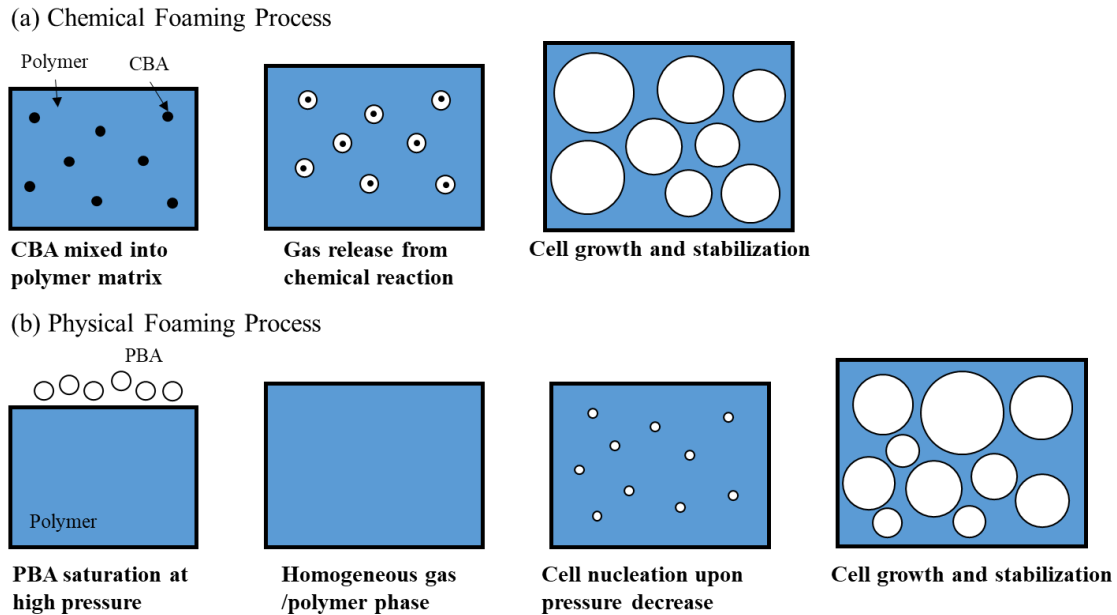


Figure 1.1 Schematic of (a) chemical and (b) physical foaming processes

The property of polymer foams is highly dependent on the cell structure, i.e., expansion ratio, cell morphology, cell size, and cell density. The expansion ratio is defined by the ratio between the volume of the polymer foam and the solid (non-foamed) material. Using the expansion ratio, the polymer foams could be categorized into the following: high density (expansion < 4 fold), medium density (4 < expansion < 10 fold), low density (10 < expansion < 40 fold) and ultra-low density (expansion > 40 fold). By increasing the expansion ratio, the volume of the gaseous phase in the material increases, resulting in weight reduction and lower material cost. Furthermore, since the gaseous phase has lower thermal conductivity when compared to the polymer phase, the thermal conductivity of the foam significantly decreases with the expansion ratio.^{21,22} However, the cell walls decrease with foam's expansion ratio, resulting in a drastic decrease in mechanical property.²³

From the viewpoint of the cell morphology, the polymer foams can be categorized as closed-cell and open-cell foams, as shown in Figure 1.2. The closed-cell foams are defined as polymer foam in which the polymeric cell walls separate each cell. Because of this, the close-cell foams are rigid and could be used for automotive and aerospace applications.²¹ Open-cell foams have interconnected pores that are formed by collapsing the cell walls at higher expansion ratios. As a result, open-cell foams are more flexible when compared to closed-cell foams. Apart from that, the tortuous interconnected pore structures also help dampen the sound waves entering the foam.^{6,8,21} Due to these properties, open-cell foams are used in furniture, sound-insulations, and tissue-engineering applications.

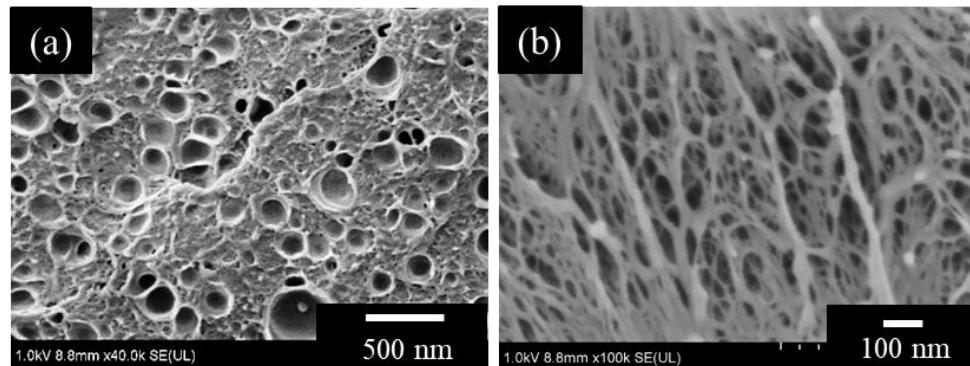


Figure 1.2 Cell morphology of polymer foams: (a) closed-cell and (b) open-cell structure

The cell size (d) and the number of cell density (N) are two crucial parameters used to evaluate the cell structure. By using the cell size and the cell density, polymer foams could be also categorized as the following: conventional foams ($d > 100 \mu\text{m}$, $N < 10^6 \text{ cells/cm}^3$), fine-cell foams ($10 < d < 100 \mu\text{m}$, $10^6 < N < 10^9 \text{ cells/cm}^3$), microcellular foams ($1 < d < 10 \mu\text{m}$, $10^9 < N < 10^{12} \text{ cells/cm}^3$), and nanocellular foams ($d < 1 \mu\text{m}$, $N > 10^{12} \text{ cells/cm}^3$).^{20,21,24} The cell size and density have been shown to affect the mechanical property of the foams significantly. The conventional foams have significantly lower mechanical strength than that of the neat material due to large voids in the polymer matrix.²⁵ To mitigate this problem, Suh et al.²⁶ proposed the concept of microcellular foams, which have cell sizes smaller than the critical flaw size of the neat polymer. Expanding this concept, they proposed three main strategies for improving the mechanical property of polymer foams: reduction of the cell size, an increase of the cell density, and improvement of the uniformity of cellular structure. Based on these strategies, various studies have reported microcellular foams with mechanical properties comparable to neat polymers.^{4,26-29} By reducing the cell size to the nanometer scale, nanocellular foams have shown further improvement in the mechanical strength, elongation at break, and toughness.³⁰⁻³³

1.2 Nanocellular polymer foams

1.2.1 Nanocellular foam properties

In the past decade, much attention has been given to the development of nanocellular foams. Apart from the improved mechanical properties, nanocellular foams also have superior thermal insulation and optical properties due to the highly dense nanoscale size pores inside the material. These properties enable nanocellular foams to be utilized in various applications, such as high-performance thermal insulating materials,³⁴ nanoporous membrane filters,³⁵ or gas storage materials.³⁶

As mentioned in the previous section, the mechanical properties of the polymer foams are highly dependent on cell size and cell density. Multiple studies have been conducted to compare between microcellular and nanocellular foams and understand how to improve the mechanical property. Miller et al.³⁰ conducted tensile and impact test on microcellular ($d = 2\text{-}5 \mu\text{m}$) and nanocellular ($d = 50\text{-}100 \text{ nm}$) polyetherimide (PEI) foams. The tensile test results

indicated that while the yield stress and elastic modulus of the nanocellular foams were similar to that of microcellular foams with similar densities, the stress and elongation at break were higher for nanocellular foams. The elongation at break was even higher than that of the bulk material, indicating significant improvement in the material toughness. Impact strength tests showed similar behavior, where nanocellular foams showed higher impact strength than the neat material, whereas microcellular foams had lower impact strength. The fracture mechanism best explains this behavior in the foam. During the material deformation, cracks appear and propagate in the foam. As the crack propagates in the nanocellular structure, the cells will yield and densify. As a result, nanoscale size cells provide stress relief, prevention of further crack propagation, and a higher degree of toughness. In microcellular foams, cell densification will not occur resulting in a reduction in stress relief. Notario et al.³¹ and Yeh et al.³² individually reported similar mechanical properties behaviors for polymethyl methacrylate (PMMA) and thermoplastic polyurethane (TPU). Apart from the effect of the highly-dense cell structure on the crack propagation, an increase in the glass transition temperature (T_g) was reported in nanocellular foams due to the molecular confinement at the cell walls and struts,³⁷⁻³⁹ which may further improve the elastic modulus of nanocellular foams.

The thermal properties of nanocellular foams are highly dependent on cell size and overall porosity of the foams. The thermal conductivity of the material (k_{tot}) for nanocellular foams is mainly expressed by Equation (1.1), where k_{con} and k_{rad} are the thermal conductivity contributed by the conduction and radiation, respectively. The conductive thermal transport is contributed by the solid (k_{sol}) and gaseous (k_{gas}) phase conductivities. Two major strategies have been utilized to minimize the thermal conductivity of the material to improve the thermal insulation of nanocellular foams. First, reducing the cell size to less than the mean free path of air (l_g), approximately 70 nm, the gas phase thermal conductivity significantly decreases due to the Knudsen effect.^{33,36,40,41} The relationship between k_{gas} and the cell size can be expressed by Equation (1.2). k_{air} is the thermal conductivity of air ($k_{air} = 26$ mW/mK, at 25 °C), β is a parameter that takes account of the energy transfer between the gas molecules and the cell wall. β is approximately 2 for air. K_n is the Knudsen number obtained by dividing the mean free path of the gas molecules by the cell size, i.e., $K_n = l_g/d$.⁴¹ Second, creating polymer foams with a higher expansion ratio will increase the porosity, which has less thermal conductivity than the solid phase.^{36,42,43} Using these strategies, Wang et al.,³³ produced super-insulating PMMA/TPU nanocellular foams with the cell size around 205 nm and eight times expansion ratios, showing thermal conductivity of 24.8 mW/mK, less than that of air (26 mW/mK). Costeux³⁶ suggested that nanocellular foams with a cell size of less than 100 nm and an expansion ratio of more than 5 are required to maximize the thermal insulation of nanocellular foams, based on thermal conductivity observations in aerogels. However, recent simulations on the thermal properties of nanocellular foams, taking the effect of the k_{rad} into account, have shown that excessive gas expansion will make the cell walls too thin, which results in higher radiative thermal conductivity of the material.^{42,44} Thus, an appropriate control of the cell structure is required to maximize the thermal insulation of nanocellular foams by increasing the Knudsen effect on k_{gas} and decreasing k_{rad} caused by the cell wall thinning. Other mechanisms to decrease the effect of the thinning of the cell wall on the thermal conductivity may be also be implemented, such as using polymers or adding nanoparticles with high radiative extinction properties.^{41,42,44}

$$k_{tot} = k_{con} + k_{rad} = k_{gas} + k_{sol} + k_{rad} \quad (1.1)$$

$$k_{gas} = \frac{k_{air}}{(1 + \beta K_n)} \quad (1.2)$$

Besides the thermal and mechanical properties, the optical properties of nanocellular foams have recently been studied, especially the production of transparent nanocellular foams. Pérez-Tamarit et al.,⁴⁵ studied the transmittance of PMMA foams with cell sizes ranging from 25-11000 nm and relative density of 0.4-0.55. The transmittance increased with larger cells for microcellular foams due to the decrease in solid-gas interfaces, which act as a scattering point for visible light. However, the opposite trend was observed for nanocellular foams due to the decreased light scattering at the nano-sized pores; higher transmittance was observed for nanocellular foams with smaller cell sizes. Martín-de León et al.⁴⁶ similarly produced nanocellular PMMA foams with 94% transmittance by reducing the cell size to 14 nm while maintaining a relative density of 0.46 and film thickness of 0.05 mm. The transmittance in the nanocellular foam showed strong dependence on the wavelength and can be fitted to the Rayleigh scattering model, similarly observed in aerogels. It is suggested that when the cell size is small enough, less than one-tenth of the wavelength, light is allowed to travel through the cells with negligible scattering directly.

While much progress has been made for elucidating the effect of the cell structure on the properties of nanocellular foams, little research has been conducted to investigate the influence of the cell order. It is mainly because cell ordering cannot be achieved by reducing cell size and increasing the expansion ratio. Producing highly ordered nanocellular foams is still a challenging issue, further discussed in section 1.2.2. Nevertheless, the effect of the ordered cell structure on the material property has been widely studied for nanoporous materials produced by sol-gel⁴⁷⁻⁴⁹ and selective etching of block copolymers.⁵⁰⁻⁵³ The mechanical property of highly-ordered nanoporous materials was significantly improved by ordering the cells.⁴⁷⁻⁴⁹ Li et al.,⁴⁸ reported that by increasing the cell ordering and orientation in mesoporous silica with similar porosities, a significant increase in Young's modulus was observed, from 0.5 to 3.1 GPa. It was mainly due to the more homogeneous cell size and cell wall thickness, which improved the stress distribution throughout the material. As a result, materials with unique mechanical properties could be prepared.⁵³ The optical properties of nanoporous films could also be improved by increasing the long-range ordering and orientation of the cells. Feng et al.,⁵⁰⁻⁵² reported that highly transparent films could be created in vertically aligned nanopores, whereas haze was observed for randomly oriented pores (cells). The increased scattering mainly occurred at the grain boundary between the randomly orientated porous domains. From these examples, the production of nanocellular foams with highly ordered cell structures could further improve the material properties of polymer foams.

1.2.2 Progress and challenges in nanocellular polymer foam production

Currently, the majority of the nanocellular foams have been predominantly produced by physical foaming. Most of these studies were conducted with CO₂ as an environmentally friendly blowing agent with high solubility within the polymer matrix. To produce a nanocellular foam successfully, a foam with a cell density of 10¹⁴ nuclei/cm³, much higher than 10⁹ nuclei/cm³ of microcellular foams, must be produced, expanded, and stabilized during the

foaming process.^{21,31,36} Three major strategies have been developed to maximize the number of nuclei and achieve high cell density, including optimizing the homogeneous nucleation process, adding the nucleating agents to induce heterogeneous nucleation, and using block copolymers as a template for the nucleation.

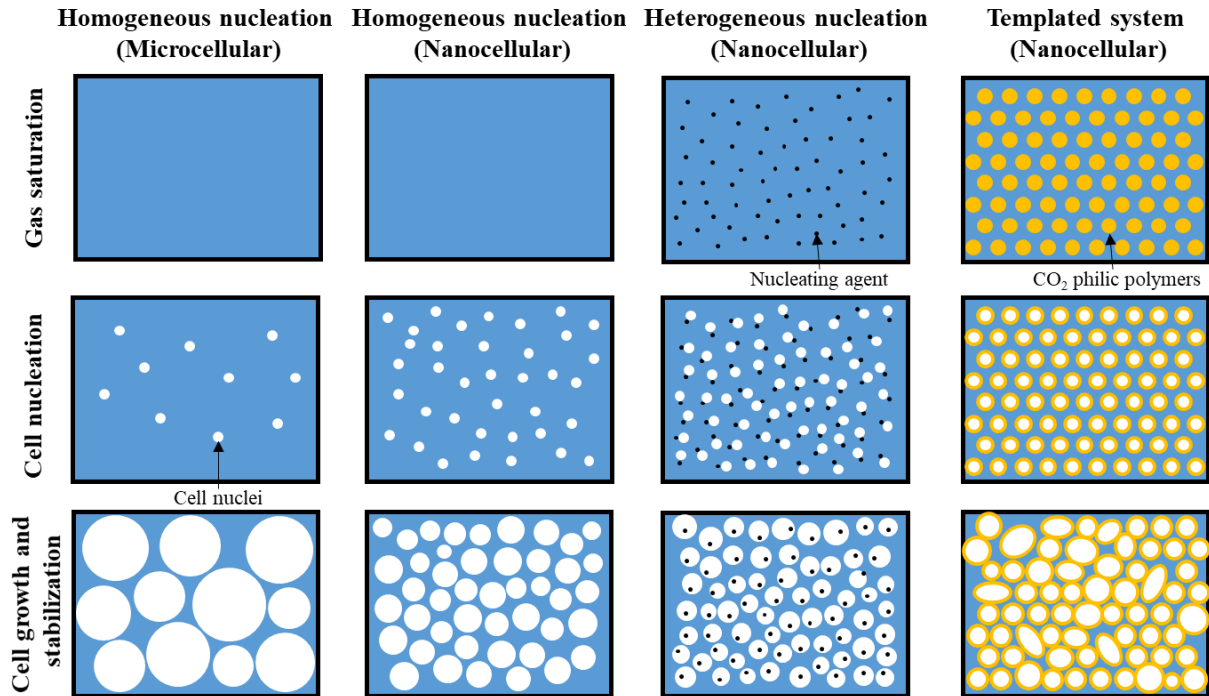


Figure 1.3 Strategies for creating nanocellular foams; homogeneous nucleation, heterogeneous nucleation and templated systems.

The homogeneous nucleation in the physical foaming processes can be maximized by adjusting process parameters, such as the polymer properties and operating conditions. According to Classical Nucleation Theory (CNT), the Gibbs free energy barrier (ΔG) for the homogeneous nucleation could be expressed by Equation (1.3), where γ_{cp} is the surface tension between the cell and bulk polymer phase, and ΔP is the pressure difference between the cell (P_c) and the polymer (P_p). The concentration of physical blowing agents (PBA)s, like CO_2 (C), could be incorporated in Equation (1.3) through Henry's law ($P_c = CH$), where H is Henry's constant, which depends on the solubility of the gas in the polymer. The critical cell size (R^*), which is needed for the nuclei to grow in the polymer, and the homogeneous nucleation rate (J) could be expressed by Equations (1.4) and (1.5), where the f_0 is the nuclei production constant and C_0 is the initial concentration of physical blowing agent dissolved in the polymer.

Using CNT as a guideline, the homogeneous cell nucleation could be enhanced by higher PBA concentrations or the depressurization rate during the foaming process. Since most nanocellular foaming experiments are conducted by batch foaming, where an equilibrium state of PBA and polymer can be easily achieved, the PBA concentration can be controlled by increasing the pressure and dissolution time or decreasing the temperature during the gas saturation

process. Guo et al.,⁵⁴ demonstrated that the equilibrium CO₂ concentration in PMMA could be increased from 11.4% at 40 °C to 39.3% at -30 °C at a gas saturation pressure of 5 MPa. At these gas saturation conditions microcellular foams ($d = 96 \mu\text{m}$, $N = 3.86 \times 10^5 \text{ cells/cm}^3$) and nanocellular foams ($d = 35 \text{ nm}$, $N = 3.01 \times 10^{14} \text{ cells/cm}^3$), were observed as a result of the different CO₂ concentrations. CO₂ concentration where the transition between micro and nanocellular foams was identified at 32.6 %. Martín-de León et al.⁵⁵ similarly demonstrated that the cell size and cell density of the nanocellular foam could be adjusted by increasing the gas saturation pressure from 6-20 MPa at -32 °C. Under these conditions, the gas concentration increased from 39-48 %, where the cell size decreased from 39 to 14 nm, and the cell density increased from 1.2×10^{16} to $6.9 \times 10^{16} \text{ cells/cm}^3$. Recent development in ultra-high gas saturation pressure ($P > 50 \text{ MPa}$) and rapid depressurization ($dP/dt > 1.25 \text{ GPa/s}$) enabled Ono et al.⁵⁶ to produce nanocellular foams with highly dense nanocellular foams with cell size less than 100 nm without the cooling requirement during the gas saturation stage.

$$\Delta G = \frac{16\pi}{3\Delta P^2} \gamma_{cp} = \frac{16\pi}{3(P_c - P_p)^2} \gamma_{cp} = \frac{16\pi}{3(CH - P_p)} \gamma_{cp} \quad (1.3)$$

$$R^* = \frac{2\gamma_{cp}}{\Delta P} = \frac{2\gamma_{cp}}{CH - P_p} \quad (1.4)$$

$$J = f_0 C_0 \exp \left[-\frac{\Delta G}{kT} \right] \quad (1.5)$$

Heterogeneous nucleation systems were employed to relax the gas saturation requirements and are considered one of the most effective strategies to create nanocellular foams.²¹ By adding nano-sized fillers, such as nanoclay,^{32,57,58} SiO₂,^{59,60} POSS,⁵⁹ and graphene,^{61,62} the Gibbs free energy barrier for nucleation at the interface between the nucleating agent and the polymer considerably decreases. Because of this, the energy required for the growth of the cells until its critical radius decreases and more cells can grow, as illustrated in Figure 1.3. Since the amount of nano-fillers correlates to the number of nucleating sites, the cell size and the cell density of the nanocellular foam be controlled.⁵⁹ Apart from inducing heterogeneous nucleation, the nano-sized fillers could also improve the property of the nanocellular foam. Yeh et al.,³² reported an improvement in Young's modulus and yield strength of nanocellular PMMA foams reinforced with nano-clay. Wang et al.,⁶³ demonstrated the production of poly(ether-block-amide)(PEBA)/multi-wall carbon nanotubes(MWCNT) nanocellular foams with electromagnetic interference shielding properties. However, due to the low compatibility of the inorganic nucleating agents with the polymer matrix, an optimum compounding scheme is required to allow a nucleating agent to have a uniform dispersion.

In contrast to heterogeneous nucleating systems, self-assembled block copolymer allows the effective dispersion of the nucleating sites throughout the polymer matrix. In the process, block copolymers structured with PBA(CO₂) philic block, such as poly(perfluorooctylethyl methacrylate) (PFMA),⁶⁴⁻⁶⁷ poly(4-(perfluorooctylpropyloxy)styrene) (PFS),⁶⁸ poly(1,1,2,2-tetrahydroperfluorodecyl acrylate) (PFDA)⁶⁹ and poly(ethylene glycol) (PEG),⁷⁰⁻⁷² are self-assembled and can be used as a template for foaming. The high solubility of the physical blowing agent in the CO₂-philic block and the heterogeneous nucleation either in the CO₂-philic block

polymer domain or at the interface between the two block-domains result in the production of nanocellular foams with relatively uniform cell structures.⁶⁶⁻⁶⁸ However, there are two significant drawbacks to this process. First, due to the selective swelling of the physical blowing agent in the CO₂-philic domains, the effective volume fraction of the block copolymer may change, and the adequate segregation strength between the two blocks decreases. These changes may result in reconstructing the self-assembled structure, or transition to a disordered structure, depending on the amount of CO₂ dissolved in the two polymers. Secondly, the plasticization effect of CO₂ may cause cell coalescence between two or more different CO₂-philic domains, as shown in Figure 1.3. Because of this, the cell structure does not represent the original self-assembled template, and the cell density is much less than the expected value assuming one nucleus is created per CO₂-philic domains.^{66-68,70,73} Despite these drawbacks, the concept of using a phase-separated polymer with CO₂-philic domains has proven effective in inducing heterogeneous nucleation through the polymer. For this reason, it has been expanded to various homo and block copolymer blends, such as PMMA/ poly(methyl methacrylate-*b*-butyl acrylate-*b*-methyl methacrylate) (MAM),⁷⁴⁻⁷⁷ polycarbonate (PC)/poly(lactic acid) (PLA),⁷⁸ PP/thermoplastic polystyrene (TPS),⁷⁹ and PP/poly(propylene-co-ethylene) rubber (PER)⁸⁰ foams.

Despite the success in creating nanocellular foams with various cell size, density, and expansion ratio, scarce progress have been made towards the mass production of nanocellular foams by physical foaming. The nanocellular foams discussed above were mainly created by the batch foaming processes. The batch foaming process can easily realize the high CO₂ concentrations by increasing gas saturation pressure and saturation time and decreasing the saturation temperatures. Due to these saturation requirements, it has been challenging to scale up the batch process to a continuous or semi-continuous process. To the author's knowledge, only two cases have been reported for nanocellular foams produced by such a process. Costeux et al.,⁸¹ demonstrated the first successful production of nanocellular foams by an extrusion foaming process, where PMMA foams with a cell size of 300 nm and expansion ratio of 3-4 times were produced. Meanwhile, Wang et al.,⁸² produced nanocellular PP/polytetrafluoroethylen (PTFE) with a cell size of 150 nm and cell density of 5.1×10^{13} cells/cm³ by a mold-opening foam injection molding process.

Chemical foaming is an alternative method to create nanocellular foams. Due to the gas being created from a chemical reaction, the process does not require the challenging gas saturation requirement used in physical foaming. However, chemical foaming is mainly limited by the specification of the blowing agents. In conventional chemical foaming processes, the blowing agent decomposes and generates gaseous compounds, which fill and expand the space initially occupied by the blowing agent, as previously shown in Figure 1.1(b). Since the size of the chemical blowing agent is typically in the order of 1-10 μm,^{83,84} it remains challenging to produce nano-sized cells. Furthermore, the low dispersibility of the chemical blowing agent in the polymer may result in nanocellular foams with significantly low cell density.

1.3 Thesis overview and objectives

The thesis research aims to develop a novel foaming process to produce nanocellular foam with a highly ordered cell structure. Based on the discussion in Section 1.2, nanocellular foams can be used in a wide array of applications.

Depending on their cell structure and cell order, the thermal, mechanical, and optical properties of the nanocellular foams could be adjusted to be suitable for high-performance thermal insulating materials, nanoporous membrane filters, or gas storage materials applications. However, the harsh processing conditions currently limit the production of nanocellular foams on an industrial scale. For this reason, we proposed a nanocellular foaming method that addresses these two major issues: (1) creating nanocellular foams at relatively mild processing conditions and (2) achieving good control over the cell structure and the cell order.

To address the first issue, we applied the UV-induced chemical foaming process to create the nanocellular foam. The UV-induced chemical foaming process, proposed by Kojima et al. initially,⁸⁵ is a chemical foaming process with a polymeric chemical blowing agent. Since the gas is generated directly from the polymer through a chemical reaction, it does not require the harsh processing conditions used in physical foaming while also mitigating the CBA size and dispersibility disadvantage of conventional chemical foaming. The UV-induced chemical foaming process is summarized in Figure 1.4(a). In this process, a copolymer containing tert-butyl ester functionalized polymers, such as poly(tert-butyl acrylate) (PtBA) and poly(tert-butyl methacrylate) (PtBMA), is mixed with a small amount of photoacid generators (PAGs). Acids are then created from the PAG by UV irradiation. Upon heating, these acids will diffuse around and deprotect the tert-butyl ester functional group in the polymer (Figure 1.4(c)). Consequently, isobutene gas is generated and expanded within the polymer to create nano-sized cells.

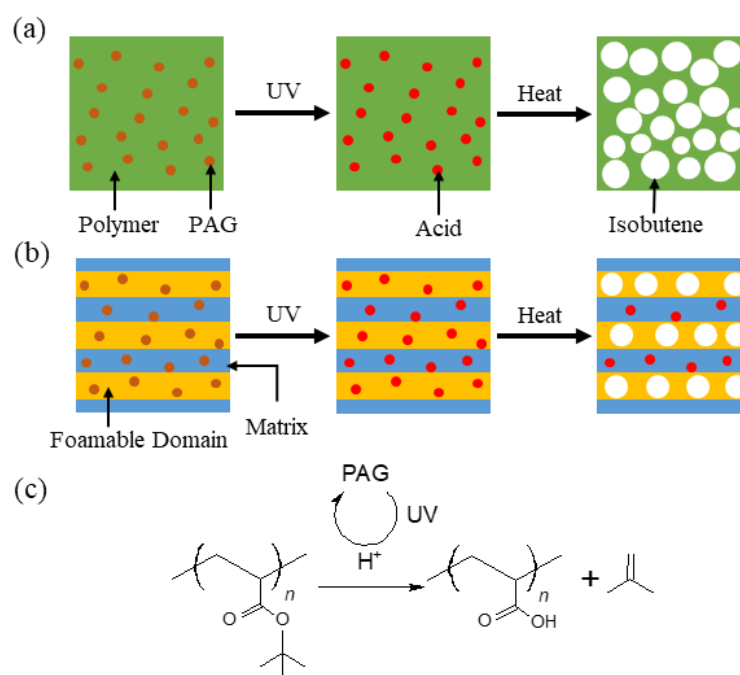
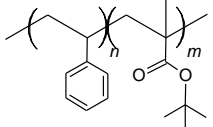
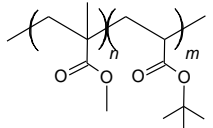


Figure 1.4 Schematic of the UV induced chemical foaming process with (a) homopolymer/ random copolymers (Kojima et al.⁸⁴) and (b) self-assembled block copolymers (this study). (c) Acid catalyzed tert-Butyl ester deprotection reaction.

For the second issue, we proposed the incorporation of self-assembled block copolymer templates with the UV-induced chemical foaming process to control the cell structure and cell ordering of the nanocellular foam. The self-assembled block copolymer template should consist of a tert-butyl ester functionalized foamable block and a stable (rigid) matrix domain. A stable matrix domain, consisting of high T_g polymers such as PS or PMMA, is necessary to avoid the structural reconstruction and plasticization effect observed in physical foaming with self-assembled block copolymers (Section 1.2.2). By taking advantage of the relatively low foaming temperature for the UV-induced chemical foaming process, this can be achieved conducting the foaming well below the T_g of the matrix polymer. As a result, the stable matrix domain can prevent cell coalescence during the foaming, and the gas is generated and expanded in only the foamable domain (Figure 1.4(b)). This results in the production of highly-ordered nanocellular foams, with cell size and structure depending on the morphology of the self-assembled block copolymer template.

Table 1.1 Outline of each main chapter in this thesis

Chapter	Block copolymer/ Specification	Focus
Chapter 2 Photocleavable polymer synthesis	<p>PS-b-PtBMA</p>  <p>PMMA-b-PtBA</p> 	TERP polymerization of PS-b-PtBMA and PMMA-b-PtBA with well controlled M_n , D , ϕ_A .
Chapter 3 Effect of process parameters	<p>PMMA-b-PtBA</p> <p>$M_n = 59,000 / \phi_{PtBA} = 30.5 \text{ wt\%}$</p> <p>Self-assembly: Cylindrical PtBA morphology</p>	Determine the effect of the foaming time, foaming temperature, PAG concentration and UV-irradiation depth on the cell structure.
Chapter 4 Effect of the self- assembled morphology	<p>PMMA-b-PtBA</p> <p>$M_n = 25,500-233,00 / \phi_{PtBA} = 30.5-66.7 \text{ wt\%}$</p> <p>Self-assembly: Cylindrical PtBA morphology Lamella PtBA morphology Cylindrical PMMA morphology</p>	Determine the effect of the self-assembled structure and M_n on the cell structure.

This thesis undertook fundamental research on the UV-induced chemical foaming with self-assembled block copolymer templates to create nanocellular foams with controllable cell structure and cell ordering, as summarized in Table 1.1. It includes the synthesis of photocleavable block copolymers for the UV-induced chemical foaming (Chapter 2), investigation of the formation of highly ordered nanocellular foams, and evaluation of the effect of process parameters (Chapter 3) as well as the self-assembled morphology (Chapter 4) on the cell structure and the cell order.

In Chapter 2, photocleavable block copolymers, PS-*b*-PtBMA and PMMA-*b*-PtBA, were synthesized by organotellurium-mediated living radical polymerization (TERP). Since the morphology of the self-assembled block copolymer is highly dependent on the specification of the block copolymers, the M_n , dispersity (\mathcal{D}), polymer weight fraction (ϕ_A), and the number of dead polymers were carefully monitored during the polymerization. In the case of PS-*b*-PtBMA, the polymerization was conducted a homogeneous solution. While well-controlled polymerization was achieved for PS-*b*-PtBMA with low M_n , deactivation of the chain transfer agent occurred for high M_n due to the high viscosity of the polymerization solution. This resulted in a relatively large number of dead polymers and high \mathcal{D} . To mitigate the effect of the polymerization solution viscosity, PMMA-*b*-PtBA was synthesized by TERP in an emulsion system, where well-controlled polymerization was achieved for PMMA-*b*-PtBA with M_n ranging from 25,500 to 233,200.

In Chapter 3, PMMA-*b*-PtBA with hexagonally packed cylindrical PtBA morphology was prepared by solution casting, and nanocellular foams were created from the self-assembled morphology by UV-induced chemical foaming. Suitable foaming conditions were determined as 80-120 °C for 0-10 minutes, based on the T_g of the PMMA and PtBA blocks, as well as the decomposition of the tert-butyl ester group. Under these foaming conditions, highly-ordered spherical cells with cell size and density of ~16–25 nm and $\sim 0.8\text{--}1.9 \times 10^{16}$ cells/cm³ were created. The effects of the process parameters, such as PAG concentration, foaming temperature, and UV-penetration, on the cell structure were investigated to further insight into how the process could be further optimized or scaled up.

In Chapter 4, the effect of different PMMA-*b*-PtBA self-assembled morphologies on the formation of the nanocellular foams is investigated. Self-assembled templates with cylindrical and lamella PtBA-rich morphologies, as well as short-ranged order cylindrical PMMA-rich morphologies were created by solvent casting PMMA-*b*-PtBA with different PtBA weight fractions (ϕ_{PtBA}). Nanocellular foams with a higher degree of expansion were created from self-assembled morphologies with larger PtBA domains due to the increased gas generation in the PtBA-foamable domain and the decreased stability of the PMMA-matrix domain. The relation between the domain size of PtBA and the expandability was also investigated for PtBA-rich lamella morphologies with M_n from 73,800 to 233,000. While larger cells were observed in PMMA-*b*-PtBA with higher M_n at 80 °C, the cell expansion at higher foaming temperature decreased due to the higher viscosity of the PMMA-rich domains.

Finally, in Chapter 5, the results obtained in this thesis are summarized, and the prospects of using UV-induced chemical foaming to create highly ordered nanocellular foams are discussed.

1.4 Reference

- (1) Wang, L.; Hikima, Y.; Ishihara, S.; Ohshima, M. Fabrication of Lightweight Microcellular Foams in Injection-Molded Polypropylene Using the Synergy of Long-Chain Branches and Crystal Nucleating Agents. *Polymer (Guildf)*. **2017**, *128*, 119–127. <https://doi.org/10.1016/j.polymer.2017.09.025>.
- (2) Tomasko, D. L.; Burley, A.; Feng, L.; Yeh, S. K.; Miyazono, K.; Nirmal-Kumar, S.; Kusaka, I.; Koelling, K. Development of CO₂ for Polymer Foam Applications. *J. Supercrit. Fluids* **2009**, *47* (3), 493–499. <https://doi.org/10.1016/j.supflu.2008.10.018>.
- (3) Zhao, J.; Zhao, Q.; Wang, L.; Wang, C.; Guo, B.; Park, C. B.; Wang, G. Development of High Thermal Insulation and Compressive Strength BPP Foams Using Mold-Opening Foam Injection Molding with in-Situ Fibrillated PTFE Fibers. *Eur. Polym. J.* **2018**, *98*, 1–10. <https://doi.org/10.1016/j.eurpolymj.2017.11.001>.
- (4) Bao, J. B.; Nyantakyi Junior, A.; Weng, G. S.; Wang, J.; Fang, Y. W.; Hu, G. H. Tensile and Impact Properties of Microcellular Isotactic Polypropylene (PP) Foams Obtained by Supercritical Carbon Dioxide. *J. Supercrit. Fluids* **2016**, *111*, 63–73. <https://doi.org/10.1016/j.supflu.2016.01.016>.
- (5) A Valle, M.; Scattina, A. Mechanical Properties and Impact Behavior of a Microcellular Structural Foam. *Lat. Am. J. Solids Struct.* **2014**, *11* (2), 200–222. <https://doi.org/10.1590/S1679-78252014000200004>.
- (6) Tiuc, A. E.; Vermeşan, H.; Gabor, T.; Vasile, O. Improved Sound Absorption Properties of Polyurethane Foam Mixed with Textile Waste. *Energy Procedia* **2016**, *85*, 559–565. <https://doi.org/10.1016/j.egypro.2015.12.245>.
- (7) Notario, B.; Ballesteros, A.; Pinto, J.; Rodríguez-Pérez, M. A. Nanoporous PMMA: A Novel System with Different Acoustic Properties. *Mater. Lett.* **2016**, *168*, 76–79. <https://doi.org/10.1016/j.matlet.2016.01.037>.
- (8) Azahari, M. S. M.; Rus, A. Z. M.; Kormin, S.; Zaliran, M. T. Acoustic Properties of Polymer Foam Composites Blended with Different Percentage Loadings of Natural Fiber. *IOP Conf. Ser. Mater. Sci. Eng.* **2017**, *244* (1), 012009. <https://doi.org/10.1088/1757-899X/244/1/012009>.
- (9) Chen, W.; Hao, H.; Hughes, D.; Shi, Y.; Cui, J.; Li, Z. X. Static and Dynamic Mechanical Properties of Expanded Polystyrene. *Mater. Des.* **2015**, *69*, 170–180. <https://doi.org/10.1016/j.matdes.2014.12.024>.
- (10) Ramli Sulong, N. H.; Mustapa, S. A. S.; Abdul Rashid, M. K. Application of Expanded Polystyrene (EPS) in Buildings and Constructions: A Review. *J. Appl. Polym. Sci.* **2019**, *136* (20), 47529. <https://doi.org/10.1002/app.47529>.
- (11) Raps, D.; Hossieny, N.; Park, C. B.; Altstädt, V. Past and Present Developments in Polymer Bead Foams and Bead Foaming Technology. *Polymer (Guildf)*. **2015**, *56*, 5–19. <https://doi.org/10.1016/j.polymer.2014.10.078>.
- (12) Koo, M. S.; Chung, K.; Youn, J. R. Reaction Injection Molding of Polyurethane Foam for Improved Thermal Insulation. *Polym. Eng. Sci.* **2001**, *41* (7), 1177–1186. <https://doi.org/10.1002/pen.10819>.
- (13) Ma, X.; Tu, R.; Cheng, X.; Zhu, S.; Ma, J.; Fang, T. Experimental Study of Thermal Behavior of Insulation

- Material Rigid Polyurethane in Parallel, Symmetric, and Adjacent Building Façade Constructions. *Polymers (Basel)*. **2018**, *10* (10), 1104. <https://doi.org/10.3390/polym10101104>.
- (14) Jin, F.-L. L.; Zhao, M.; Park, M.; Park, S.-J. J.; Jin, F.-L. L.; Zhao, M.; Park, M.; Park, S.-J. J. Recent Trends of Foaming in Polymer Processing: A Review. *Polymers (Basel)*. **2019**, *11* (6), 953. <https://doi.org/10.3390/polym11060953>.
- (15) Pop-Iliev, R.; Liu, F.; Liu, G.; Park, C. B. Rotational Foam Molding of Polypropylene with Control of Melt Strength. *Adv. Polym. Technol.* **2003**, *22* (4), 280–296. <https://doi.org/10.1002/adv.10056>.
- (16) Bao, J. B.; Nyantakyi Junior, A.; Weng, G. S.; Wang, J.; Fang, Y. W.; Hu, G. H. Tensile and Impact Properties of Microcellular Isotactic Polypropylene (PP) Foams Obtained by Supercritical Carbon Dioxide. *J. Supercrit. Fluids* **2016**, *111*, 63–73. <https://doi.org/10.1016/j.supflu.2016.01.016>.
- (17) Weiser, E. S.; Johnson, T. F.; St Clair, T. L.; Echigo, Y.; Kaneshiro, H.; Grimsley, B. W. Polyimide Foams for Aerospace Vehicles. *High Perform. Polym.* **2000**, *12* (1), 1–12. <https://doi.org/10.1088/0954-0083/12/1/301>.
- (18) Coste, G.; Negrell, C.; Caillol, S. From Gas Release to Foam Synthesis, the Second Breath of Blowing Agents. *Eur. Polym. J.* **2020**, *140*, 110029. <https://doi.org/10.1016/j.eurpolymj.2020.110029>.
- (19) Taki, K.; Tabata, K.; Kihara, S. I.; Ohshima, M. Bubble Coalescence in Foaming Process of Polymers. *Polym. Eng. Sci.* **2006**, *46* (5), 680–690. <https://doi.org/10.1002/pen.20521>.
- (20) Okolieocha, C.; Raps, D.; Subramaniam, K.; Altstädt, V. Microcellular to Nanocellular Polymer Foams: Progress (2004-2015) and Future Directions - A Review. *Eur. Polym. J.* **2015**, *73*, 500–519. <https://doi.org/10.1016/j.eurpolymj.2015.11.001>.
- (21) Azdast, T.; Hasanzadeh, R. Increasing Cell Density/Decreasing Cell Size to Produce Microcellular and Nanocellular Thermoplastic Foams: A Review. *J. Cell. Plast.* **2020**, *57* (5), 769–797. <https://doi.org/10.1177/0021955X20959301>.
- (22) Wu, G.; Xie, P.; Yang, H.; Dang, K.; Xu, Y.; Sain, M.; Turng, L. S.; Yang, W. A Review of Thermoplastic Polymer Foams for Functional Applications. *Journal of Materials Science*. Springer 2021, pp 11579–11604. <https://doi.org/10.1007/s10853-021-06034-6>.
- (23) Wang, L.; Ishihara, S.; Hikima, Y.; Ohshima, M.; Sekiguchi, T.; Sato, A.; Yano, H. Unprecedented Development of Ultrahigh Expansion Injection-Molded Polypropylene Foams by Introducing Hydrophobic-Modified Cellulose Nanofibers. *ACS Appl. Mater. Interfaces* **2017**, *9* (11), 9250–9254. <https://doi.org/10.1021/acsami.7b01329>.
- (24) Eungkee Lee, R.; Hasanzadeh, R.; Azdast, T. A Multi-Criteria Decision Analysis on Injection Moulding of Polymeric Microcellular Nanocomposite Foams Containing Multi-Walled Carbon Nanotubes. *Plast. Rubber Compos.* **2017**, *46* (4), 155–162. <https://doi.org/10.1080/14658011.2017.1300210>.
- (25) Gibson, L. J. Modelling the Mechanical Behavior of Cellular Materials. *Mater. Sci. Eng. A* **1989**, *110* (C), 1–36. [https://doi.org/10.1016/0921-5093\(89\)90154-8](https://doi.org/10.1016/0921-5093(89)90154-8).
- (26) Kumar, V.; Suh, N. P. A Process for Making Microcellular Thermoplastic Parts. *Polym. Eng. Sci.* **1990**, *30*

- (20), 1323–1329. <https://doi.org/10.1002/pen.760302010>.
- (27) Sun, X.; Kharbas, H.; Peng, J.; Turng, L. S. A Novel Method of Producing Lightweight Microcellular Injection Molded Parts with Improved Ductility and Toughness. *Polymer (Guildf)*. **2015**, *56*, 102–110. <https://doi.org/10.1016/j.polymer.2014.09.066>.
- (28) Shimbo, M.; Higashitani, I.; Miyano, Y. Mechanism of Strength Improvement of Foamed Plastics Having Fine Cell. *J. Cell. Plast.* **2007**, *43* (2), 157–167. <https://doi.org/10.1177/0021955X06075585>.
- (29) Bao, J. B.; Liu, T.; Zhao, L.; Hu, G. H.; Miao, X.; Li, X. Oriented Foaming of Polystyrene with Supercritical Carbon Dioxide for Toughening. *Polymer (Guildf)*. **2012**, *53* (25), 5982–5993. <https://doi.org/10.1016/j.polymer.2012.10.011>.
- (30) Miller, D.; Kumar, V. Microcellular and Nanocellular Solid-State Polyetherimide (PEI) Foams Using Sub-Critical Carbon Dioxide II. Tensile and Impact Properties. *Polymer (Guildf)*. **2011**, *52* (13), 2910–2919. <https://doi.org/10.1016/j.polymer.2011.04.049>.
- (31) Notario, B.; Pinto, J.; Rodríguez-Pérez, M. A. Towards a New Generation of Polymeric Foams: PMMA Nanocellular Foams with Enhanced Physical Properties. *Polymer (Guildf)*. **2015**, *63*, 116–126. <https://doi.org/10.1016/j.polymer.2015.03.003>.
- (32) Yeh, S.-K. K.; Liu, Y.-C. C.; Chu, C.-C. C.; Chang, K.-C. C.; Wang, S.-F. F. Mechanical Properties of Microcellular and Nanocellular Thermoplastic Polyurethane Nanocomposite Foams Created Using Supercritical Carbon Dioxide. *Ind. Eng. Chem. Res.* **2017**, *56* (30), 8499–8507. <https://doi.org/10.1021/acs.iecr.7b00942>.
- (33) Wang, G.; Zhao, J.; Howe Mark, L.; Wang, G.; Yu, K.; Wang, C.; Park, C. B.; Zhao, G. Ultra-Tough and Super Thermal-Insulation Nanocellular PMMA/TPU. *Chem. Eng. J.* **2017**, *325*, 632–646. <https://doi.org/10.1016/j.cej.2017.05.116>.
- (34) Liu, S.; DuVigneau, J.; Vancso, G. J. Nanocellular Polymer Foams as Promising High Performance Thermal Insulation Materials. *Eur. Polym. J.* **2015**, *65*, 33–45. <https://doi.org/10.1016/J.EURPOLYMJ.2015.01.039>.
- (35) Pinto, J.; Dumon, M.; Rodriguez-Perez, M. A.; Garcia, R.; Dietz, C. Block Copolymers Self-Assembly Allows Obtaining Tunable Micro or Nanoporous Membranes or Depth Filters Based on PMMA; Fabrication Method and Nanostructures. *J. Phys. Chem. B* **2014**, *118* (9), 4656–4663. <https://doi.org/10.1021/jp409803u>.
- (36) Costeux, S. CO₂-Blown Nanocellular Foams. *J. Appl. Polym. Sci.* **2014**, *131* (23), 41293. <https://doi.org/10.1002/app.41293>.
- (37) Yeh, S. K.; Liao, Z. E.; Wang, K. C.; Ho, Y. T.; Kurniawan, V.; Tseng, P. C.; Tseng, T. W. Effect of Molecular Weight to the Structure of Nanocellular Foams: Phase Separation Approach. *Polymer (Guildf)*. **2020**, *191*, 122275. <https://doi.org/10.1016/j.polymer.2020.122275>.
- (38) Martín-de León, J.; Bernardo, V.; Rodríguez-Pérez, M. Low Density Nanocellular Polymers Based on PMMA Produced by Gas Dissolution Foaming: Fabrication and Cellular Structure Characterization. *Polymers (Basel)*. **2016**, *8* (7), 265. <https://doi.org/10.3390/polym8070265>.
- (39) Pinto, J.; Notario, B.; Verdejo, R.; Dumon, M.; Costeux, S.; Rodriguez-Perez, M. A. Molecular

- Confinement of Solid and Gaseous Phases of Self-Standing Bulk Nanoporous Polymers Inducing Enhanced and Unexpected Physical Properties. *Polymer (Guildf)*. **2017**, *113*, 27–33.
<https://doi.org/10.1016/J.POLYMER.2017.02.046>.
- (40) Cuadra-Rodríguez, D.; Barroso-Solares, S.; Pinto, J. Advanced Nanocellular Foams: Perspectives on the Current Knowledge and Challenges. *Nanomaterials* **2021**, *11* (3), 621.
<https://doi.org/10.3390/NANO11030621>.
- (41) Notario, B.; Pinto, J.; Solorzano, E.; De Saja, J. A.; Dumon, M.; Rodríguez-Pérez, M. A. Experimental Validation of the Knudsen Effect in Nanocellular Polymeric Foams. *Polymer (Guildf)*. **2015**, *56*, 57–67.
<https://doi.org/10.1016/j.polymer.2014.10.006>.
- (42) Wang, G.; Wang, C.; Zhao, J.; Wang, G.; Park, C. B.; Zhao, G. Modelling of Thermal Transport through a Nanocellular Polymer Foam: Toward the Generation of a New Superinsulating Material. *Nanoscale* **2017**, *9* (18), 5996–6009. <https://doi.org/10.1039/c7nr00327g>.
- (43) Wang, G.; Zhao, J.; Wang, G.; Mark, L. H.; Park, C. B.; Zhao, G. Low-Density and Structure-Tunable Microcellular PMMA Foams with Improved Thermal-Insulation and Compressive Mechanical Properties. *Eur. Polym. J.* **2017**, *95*, 382–393. <https://doi.org/10.1016/j.eurpolymj.2017.08.025>.
- (44) Buahom, P.; Wang, C.; Alshrah, M.; Wang, G.; Gong, P.; Tran, M. P.; Park, C. B. Wrong Expectation of Superinsulation Behavior from Largely-Expanded Nanocellular Foams. *Nanoscale* **2020**, *12* (24), 13064–13085. <https://doi.org/10.1039/d0nr01927e>.
- (45) Pérez-Tamarit, S.; Notario, B.; Solórzano, E.; Rodríguez-Pérez, M. A. Light Transmission in Nanocellular Polymers: Are Semi-Transparent Cellular Polymers Possible? *Mater. Lett.* **2018**, *210*, 39–41.
<https://doi.org/10.1016/j.matlet.2017.08.109>.
- (46) Martín-de León, J.; Pura, J. L.; Bernardo, V.; Rodríguez-Pérez, M. Á. Transparent Nanocellular PMMA: Characterization and Modeling of the Optical Properties. *Polymer (Guildf)*. **2019**, *170*, 16–23.
<https://doi.org/10.1016/j.polymer.2019.03.010>.
- (47) Lionello, D. F.; Ramallo, J. I.; Soler-Illia, G. J. A. A.; Fuertes, M. C. Mechanical Properties of Ordered Mesoporous Oxides Thin Films. *J. Sol-Gel Sci. Technol.* **2021**, *2021*, 1–26. <https://doi.org/10.1007/S10971-021-05626-7>.
- (48) Li, X.; Song, L.; Vogt, B. D. Tuning Mechanical Properties of Mesoporous Silicas Using Associating Homopolymers/ Block Copolymer Blends as Templates. *J. Phys. Chem. C* **2008**, *112* (1), 53–60.
https://doi.org/10.1021/JP0762727/SUPPL_FILE/JP0762727-FILE002.PDF.
- (49) Ng, K. Y.; Ngan, A. H. W. Effects of Pore-Channel Ordering on the Mechanical Properties of Anodic Aluminum Oxide Nano-Honeycombs. *Scr. Mater.* **2012**, *66* (7), 439–442.
<https://doi.org/10.1016/J.SCRIPTAMAT.2011.12.010>.
- (50) Feng, X.; Nejati, S.; Cowan, M. G.; Tousley, M. E.; Wiesenauer, B. R.; Noble, R. D.; Elimelech, M.; Gin, D. L.; Osuji, C. O. Thin Polymer Films with Continuous Vertically Aligned 1 Nm Pores Fabricated by Soft Confinement. *ACS Nano* **2019**, *10* (1), 150–158. <https://doi.org/10.1021/acsnano.5b06130>.

- (51) Feng, X.; Tousley, M. E.; Cowan, M. G.; Wiesenauer, B. R.; Nejati, S.; Choo, Y.; Noble, R. D.; Elimelech, M.; Gin, D. L.; Osuji, C. O. Scalable Fabrication of Polymer Membranes with Vertically Aligned 1 Nm Pores by Magnetic Field Directed Self-Assembly. *ACS Nano* **2014**, *8* (12), 11977–11986. <https://doi.org/10.1021/nn505037b>.
- (52) Feng, X.; Kawabata, K.; Kaufman, G.; Elimelech, M.; Osuji, C. O. Highly Selective Vertically Aligned Nanopores in Sustainably Derived Polymer Membranes by Molecular Templating. *ACS Nano* **2017**, *11* (4), 3911–3921. <https://doi.org/10.1021/acsnano.7b00304>.
- (53) Hsueh, H. Y.; Yao, C. T.; Ho, R. M. Well-Ordered Nanohybrids and Nanoporous Materials from Gyroid Block Copolymer Templates. *Chem. Soc. Rev.* **2015**, *44* (7), 1974–2018. <https://doi.org/10.1039/c4cs00424h>.
- (54) Guo, H.; Nicolae, A.; Kumar, V. Solid-State Poly(Methyl Methacrylate) (PMMA) Nanofoams. Part II: Low-Temperature Solid-State Process Space Using CO₂ and the Resulting Morphologies. *Polymer (Guildf)*. **2015**, *70*, 231–241. <https://doi.org/10.1016/j.polymer.2015.06.031>.
- (55) Martín-de León, J.; Bernardo, V.; Rodríguez-Pérez, M. Á. Key Production Parameters to Obtain Transparent Nanocellular PMMA. *Macromol. Mater. Eng.* **2017**, *302* (12), 1700343. <https://doi.org/10.1002/mame.201700343>.
- (56) Ono, T.; Wu, X.; Horiuchi, S.; Furuya, T.; Yoda, S. Two-Step Foaming Process for Production of PMMA Nanocellular Polymer Foams via Ultra-High Pressure and Rapid Depressurization. *J. Supercrit. Fluids* **2020**, *165*, 104963. <https://doi.org/10.1016/j.supflu.2020.104963>.
- (57) Fujimoto, Y.; Ray, S. S.; Okamoto, M.; Ogami, A.; Yamada, K.; Ueda, K. Well-Controlled Biodegradable Nanocomposite Foams: From Microcellular to Nanocellular. *Macromol. Rapid Commun.* **2003**, *24* (7), 457–461. <https://doi.org/10.1002/marc.200390068>.
- (58) Ito, Y.; Yamashita, M.; Okamoto, M. Foam Processing and Cellular Structure of Polycarbonate-Based Nanocomposites. *Macromol. Mater. Eng.* **2006**, *291* (7), 773–783. <https://doi.org/10.1002/MAME.200600075>.
- (59) Costeux, S.; Zhu, L. Low Density Thermoplastic Nanofoams Nucleated by Nanoparticles. *Polymer (Guildf)*. **2013**, *54* (11), 2785–2795. <https://doi.org/10.1016/j.polymer.2013.03.052>.
- (60) Zhai, W.; Yu, J.; Wu, L.; Ma, W.; He, J. Heterogeneous Nucleation Uniformizing Cell Size Distribution in Microcellular Nanocomposites Foams. *Polymer (Guildf)*. **2006**, *47* (21), 7580–7589. <https://doi.org/10.1016/J.POLYMER.2006.08.034>.
- (61) Yeh, S.-K.; Chen, Y.-R.; Kang, T.-W.; Tseng, T.-J.; Peng, S.-P.; Chu, C.-C.; Rwei, S.-P.; Guo, W.-J. Different Approaches for Creating Nanocellular TPU Foams by Supercritical CO₂ Foaming. <https://doi.org/10.1007/s10965-017-1419-9>.
- (62) Xiao, S. P.; Huang, H. X. Generation of Nanocellular TPU/Reduced Graphene Oxide Nanocomposite Foams with High Cell Density by Manipulating Viscoelasticity. *Polymer (Guildf)*. **2019**, *183*, 121879. <https://doi.org/10.1016/j.polymer.2019.121879>.

- (63) Wang, G.; Zhao, J.; Ge, C.; Zhao, G.; Park, C. B. Nanocellular Poly(Ether-Block-Amide)/MWCNT Nanocomposite Films Fabricated by Stretching-Assisted Microcellular Foaming for High-Performance EMI Shielding Applications. *J. Mater. Chem. C* **2021**, *9* (4), 1245–1258. <https://doi.org/10.1039/D0TC04099A>.
- (64) Yokoyama, H.; Li, L.; Nemoto, T.; Sugiyama, K. Tunable Nanocellular Polymeric Monoliths Using Fluorinated Block Copolymer Templates and Supercritical Carbon Dioxide. *Adv. Mater.* **2004**, *16* (17), 1542–1546. <https://doi.org/10.1002/adma.200400072>.
- (65) Yokoyama, H.; Li, L.; Dutriez, C.; Iwakura, Y.; Sugiyama, K.; Masunaga, H.; Sasaki, S.; Okuda, H. Horizontally and Vertically Aligned Polymeric Nanosheets: CO₂-Induced Morphological Changes of Block Copolymer Thin Films. *Macromolecules* **2008**, *41* (22), 8626–8631. <https://doi.org/10.1021/MA801487A>.
- (66) Shinkai, T.; Sugiyama, K.; Ito, K.; Yokoyama, H. Nanoporous Fabrication of Block Copolymers via Carbon Dioxide Swelling: Difference between CO₂-Swollen and Nanoporous Block Copolymers. *Polymer (Guildf)*. **2016**, *100*, 19–27. <https://doi.org/10.1016/j.polymer.2016.08.011>.
- (67) Li, L.; Nemoto, T.; Sugiyama, K.; Yokoyama, H. CO₂ Foaming in Thin Films of Block Copolymer Containing Fluorinated Blocks. *Macromolecules* **2006**, *39* (14), 4746–4755. <https://doi.org/10.1021/ma060325l>.
- (68) Yokoyama, H.; Sugiyama, K. Nanocellular Structures in Block Copolymers with CO₂-Philic Blocks Using CO₂ as a Blowing Agent: Crossover from Micro-to Nanocellular Structures with Depressurization Temperature. *Macromolecules* **2005**, *38* (25), 10516–10522. <https://doi.org/10.1021/ma051757j>.
- (69) Ruiz, J. A. R.; Cloutet, E.; Dumon, M. Investigation of the Nanocellular Foaming of Polystyrene in Supercritical CO₂ by Adding a CO₂-Philic Perfluorinated Block Copolymer. *J. Appl. Polym. Sci.* **2012**, *126* (1), 38–45. <https://doi.org/10.1002/APP.36455>.
- (70) Xu, Y.; Liu, T.; Yuan, W.-K.; Zhao, L. Influence of Microphase Morphology and Long-Range Ordering on Foaming Behavior of PE-b-PEO Diblock Copolymers. *Ind. Eng. Chem. Res.* **2015**, *54* (28), 7113–7121. <https://doi.org/10.1021/acs.iecr.5b01014>.
- (71) Zhang, W.; Chen, B.; Zhao, H.; Yu, P.; Fu, D.; Wen, J.; Peng, X. Processing and Characterization of Supercritical CO₂ Batch Foamed Poly(Lactic Acid)/Poly(Ethylene Glycol) Scaffold for Tissue Engineering Application. *J. Appl. Polym. Sci.* **2013**, *130* (5), 3066–3073. <https://doi.org/10.1002/APP.39523>.
- (72) Taki, K.; Nitta, K.; Kihara, S.-I.; Ohshima, M. CO₂ Foaming of Poly(Ethylene Glycol)/Polystyrene Blends: Relationship of the Blend Morphology, CO₂ Mass Transfer, and Cellular Structure. *J. Appl. Polym. Sci.* **2005**, *97* (5), 1899–1906. <https://doi.org/10.1002/APP.21930>.
- (73) Yokoyama, H. Small Angle X-Ray Scattering Studies of Nanocellular and Nanoporous Structures. *Polym. J.* **2013**, *45* (1), 3–9. <https://doi.org/10.1038/pj.2012.205>.
- (74) Bernardo, V.; Martín-de León, J.; Pinto, J.; Catelani, T.; Athanassiou, A.; Rodríguez-Pérez, M. A. Low-Density PMMA/MAM Nanocellular Polymers Using Low MAM Contents: Production and Characterization. *Polymer (Guildf)*. **2019**, *163*, 115–124. <https://doi.org/10.1016/J.POLYMER.2018.12.057>.
- (75) Bernardo, V.; Martín-de León, J.; Rodríguez-Pérez, M. Á. Production of PMMA-Based Nanocellular

- Polymers Using Low Demanding Saturation Conditions. *Mater. Lett.* **2019**, *255*, 126551.
<https://doi.org/10.1016/j.matlet.2019.126551>.
- (76) Pinto, J.; Reglero-Ruiz, J. A.; Dumon, M.; Rodriguez-Perez, M. A. Temperature Influence and CO₂ Transport in Foaming Processes of Poly(Methyl Methacrylate)–Block Copolymer Nanocellular and Microcellular Foams. *J. Supercrit. Fluids* **2014**, *94*, 198–205.
<https://doi.org/10.1016/J.SUPFLU.2014.07.021>.
- (77) Pinto, J.; Dumon, M.; Pedros, M.; Reglero, J.; Rodriguez-Perez, M. A. Nanocellular CO₂ Foaming of PMMA Assisted by Block Copolymer Nanostructuring. *Chem. Eng. J.* **2014**, *243*, 428–435.
<https://doi.org/10.1016/J.CEJ.2014.01.021>.
- (78) Bao, D.; Liao, X.; He, T.; Yang, Q.; Li, G. Preparation of Nanocellular Foams from Polycarbonate/Poly(Lactic Acid) Blend by Using Supercritical Carbon Dioxide. *J. Polym. Res.* **2013**, *20* (11). <https://doi.org/10.1007/S10965-013-0290-6/FIGURES/9>.
- (79) Nemoto, T.; Takagi, J.; Ohshima, M. Nanoscale Cellular Foams from a Poly(Propylene)-Rubber Blend. *Macromol. Mater. Eng.* **2008**, *293* (12), 991–998. <https://doi.org/10.1002/mame.200800184>.
- (80) Nemoto, T.; Takagi, J.; Ohshima, M. Control of Bubble Size and Location in Nano-/Microscale Cellular Poly(Propylene)/Rubber Blend Foams. *Macromol. Mater. Eng.* **2008**, *293* (7), 574–580.
<https://doi.org/10.1002/mame.200800015>.
- (81) Costeux, S.; Foether, D. Continuous Extrusion of Nanocellular Foam. In *Proceedings of the Annual Technical Conference-ANTEC, Orlando, FL, USA; 2014*; pp 23–25.
- (82) Wang, G.; Zhao, G.; Zhang, L.; Mu, Y.; Park, C. B. Lightweight and Tough Nanocellular PP/PTFE Nanocomposite Foams with Defect-Free Surfaces Obtained Using in Situ Nanofibrillation and Nanocellular Injection Molding. *Chem. Eng. J.* **2018**, *350*, 1–11. <https://doi.org/10.1016/j.cej.2018.05.161>.
- (83) Petchwattana, N.; Covavisaruch, S. Influences of Particle Sizes and Contents of Chemical Blowing Agents on Foaming Wood Plastic Composites Prepared from Poly(Vinyl Chloride) and Rice Hull. *Mater. Des.* **2011**, *32* (5), 2844–2850. <https://doi.org/10.1016/j.matdes.2010.12.044>.
- (84) Michaeli, W.; Sitz, S. Analysis of the Expansion Behaviour of Rubber Compounds with Chemical Blowing Agents. *Cell. Polym.* **2010**, *29* (4), 227–236. <https://doi.org/10.1177/026248931002900402>.
- (85) Kojima, J.; Takada, T.; Jinno, F. Thin Microcellular Plastic Sheet Incorporating Designed Foaming Patterns Made by Photochemical Foaming Technology. *J. Cell. Plast.* **2007**, *43* (2), 103–109.
<https://doi.org/10.1177/0021955X06076573>.

Chapter 2 Synthesis of High Molecular Weight Photocleavable Block Copolymer for UV-Induced Chemical Foaming

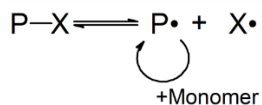
2.1 Introduction

As discussed in Chapter 1, the UV-induced chemical foaming process enables the production of nanocellular foams at ambient pressures, in contrast to physical foaming. The chemical foaming process was initially proposed by Kojima et al.¹. In the process, isobutene gas was created by the UV-irradiation on tert-butyl ester functionalized polymers, such as poly(tert-butyl acrylate) (PtBA) or poly(tert-butyl methacrylate) (PtBMA). While Kojima et al.¹ used a random copolymer of PtBA for creating a nanocellular foam in their UV-induced chemical foaming process, we expected that a similar approach could be used for self-assembled block copolymers and use the copolymer as a template for further controlling the cell structure of the nanocellular foams. For this reason, this chapter is mainly focused on synthesizing photocleavable block copolymers that contain the tert-butyl ester group for the UV-induced chemical foaming process and show the microphase-separation structures.

Reversible deactivation radical polymerization (RDRP), also known as living radical polymerization, has been widely implemented for block copolymer synthesis.^{2,3} The general mechanism of the RDRP process is illustrated in Figure 2.1(a), where the reversible activation and deactivation occurs between a dormant species (P-X) and a propagating radical (P•), i.e., active species. This activation and deactivation process minimizes unwanted termination reactions and allows the polymer chains to grow with nearly equal lengths, making them suitable for synthesizing block copolymers. Several RDRP methods of capping the groups (X) have already been developed, including nitroxide-mediated radical polymerization (NMP),^{4,5} atom transfer radical polymerization (ATRP),⁶ reversible addition-fragmentation chain-transfer radical polymerizations (RAFT)^{2,7} and organotellurium-mediated radical polymerization (TERP).⁸⁻¹⁶

Among the RDRP mentioned above, this study used the TERP process having the organotellurium chain transfer agents (CTA) to synthesize the photocleavable block copolymers. Apart from the reversible activation and deactivation process shown in Figure 2.1(a), the TERP polymerization undergoes a degenerative chain transfer process as illustrated in Figure 2.1(b). In polymerization, the free radicals are also transferred between two different CTAs, which allows more precise control of the molecular weight (M_n) and the dispersity (\mathcal{D}) of the polymer. The TERP process has been implemented to polymerize monomers with various functional groups, including acrylates,¹⁴⁻¹⁶ styrene,^{15,17} and amides.⁸ Furthermore, the TERP could also be implemented in *ab initio* emulsion polymerizations (herein referred to as emulsion polymerizations) to enable the synthesis of the block copolymers with high molecular weights ($M_n > 10^5$).^{14,16} This is due to the gradual diffusion of the monomer into the CTA/polymer micelles, as shown in Figure 2.2. The viscosity of the polymer micelle is kept relatively low in emulsion polymerization when compared to homogeneous polymerizations, which requires solvent addition for high M_n polymerization, resulting in less CTA termination.

(a) Reversible Activation/Deactivation



(b) Degenerative Transfer

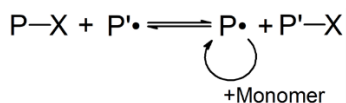


Figure 2.1 a) Reversible activation and b) degenerative chain transfer mechanisms in RDRP polymerization

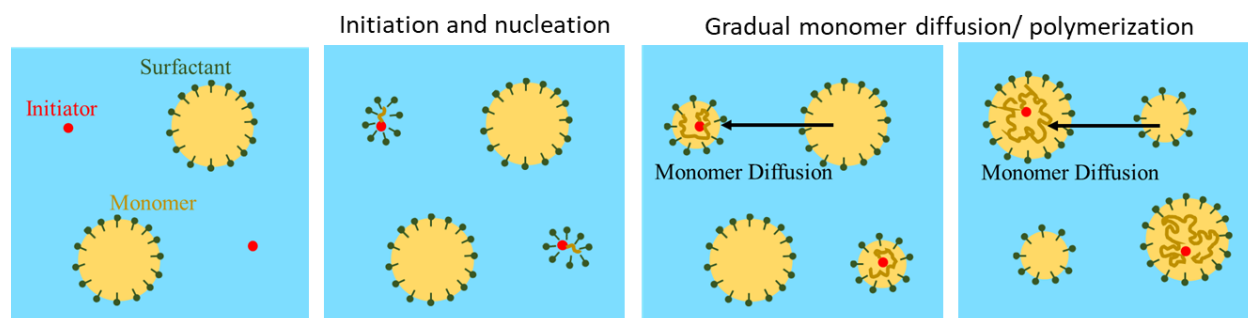


Figure 2.2 Emulsion TERP polymerization

In this chapter, photocleavable block copolymer containing tert-butyl ester functional groups was synthesized by TERP. Poly(styrene-*b*-tert butyl methacrylate) (PS-*b*-PtBMA) was synthesized in the first section by homogeneous TERP polymerization. The monomer conversion was monitored by ^1H NMR, while size exclusion chromatography was used to determine the M_n , D , and inactive macro initiators (herein referred to as dead polymers). In the latter part of this chapter, poly(methyl methacrylate-*b*-tert butyl acrylate) (PMMA-*b*-PtBA) with high M_n was synthesized by an emulsion TERP polymerization. DSC analysis identified the thermal properties of PMMA-*b*-PtBA to confirm that well-controlled block copolymer chains were created.

2.2 Methods

2.2.1 Materials

In this study, poly(styrene-*b*-tert butyl methacrylate) (PS-*b*-PtBMA) and poly(methyl methacrylate-*b*-tert butyl acrylate) (PMMA-*b*-PtBA) were synthesized by the TERP in a homogeneous solution^{9,12,13} and emulsion, respectively.^{8,11,14-16} Styrene, tert-butyl methacrylate, methyl methacrylate, and tert-butyl acrylate monomers were washed with 5% aqueous NaOH solution and distilled over CaH_2 under reduced pressure in a nitrogen (N_2) atmosphere. The purified dimethylformamide (DMF), deuterated chloroform (CDCl_3) (Sigma-Aldrich, USA), thiophenol (PhSH) (Sigma-Aldrich, USA), and DI water were treated with N_2 bubbling prior to transferring to a glovebox in a N_2 atmosphere. Azobis(4-cyanovaleric acid) (ACVA) was recrystallized in methanol. NaOH was dissolved in deaerated

DI water, and its concentration was made to be 0.50 mol L^{-1} by titration of 0.05 mol L^{-1} standard oxalic acid solution with phenolphthalein as an indicator. 4,4'-Azobis(4-cyanopentanoic acid) (ACVA) was neutralized with sodium carboxylate (Wako Co., Ltd., Japan) in an aqueous NaOH solution (2.0 equivalents), and it was diluted by deaerated DI water to a 0.10 mol L^{-1} solution. The preparation of the chain transfer agent (CTA) and the ditelluride compound ((TeR)₂) were previously reported for homogeneous (Figure 2.3)¹⁰ and emulsion polymerization (Figure 2.4)¹⁶. Azobis(cyclohexanecarbonitrile) (ABCN), hexadecyltrimethylammonium bromide (CTAB), and 2-aminoethanethiol were used as received from the supplier. Unless indicated otherwise, the chemicals used in this study were supplied by Wako Co., Ltd. (Japan).

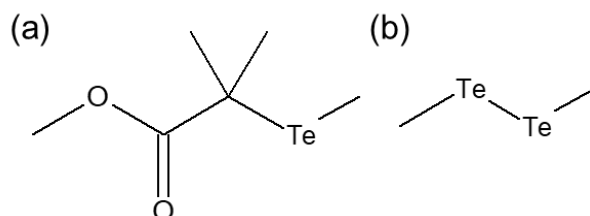


Figure 2.3 Chemical structure of the CTA-1 (a) and the (TeMe)₂ (b) for homogeneous TERP polymerization

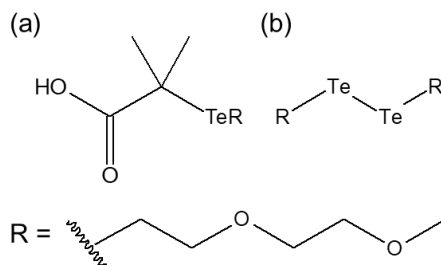


Figure 2.4 Chemical structure of the CTA-2 (a) and the (TeR)₂-2 (b) for emulsion TERP polymerization

2.2.2 Homogeneous polymerization of PS-b-PtBMA by TERP

The TERP polymerization conducted the polymerization of PS-b-PtBMA in a homogeneous solution, summarized in Figure 2.5. For the homogeneous polymerization of PS-b-PtBMA, styrene was polymerized first, followed by the polymerization of tBMA. Due to the oxygen sensitivity of the CTA, the reaction was conducted in a sealed test tube filled with N₂. CTA-1 (10 μL , 0.06 mmol) was added to the styrene (0.85 ml, 8 mmol) for the PS synthesis. The styrene polymerization was conducted under two conditions, the Azo-initiated thermal condition and the thermal condition. For Azo-initiated thermal conditions, ABCN (7.3 mg, 0.03 mmol) was added to the monomer solution, and the polymerization was conducted by keeping the temperature at 90 °C. For the thermal conditions, the monomer solution was heated to 110 °C. During the polymerization, small aliquots (ca. 100 μl) of the emulsion were taken and dissolved into the deuterated chloroform (CDCl₃). The monomer conversion was determined by ¹H NMR (400 MHz). The molecular weight (M_n) and the dispersity (D) were evaluated by size-exclusion chromatography

(SEC) at 40°C. After the conversion of the styrene monomer reaches approximately 90%, tBMA monomer and (TeMe)₂ (13 µL, 0.12 mmol) were added to the solution and the PtBMA block was polymerized. Three reaction conditions were used for the PtBMA polymerization, including the Azo-initiated thermal condition, thermal condition, and photo-irradiated condition. The Azo-initiated and thermal polymerization of PtBMA were conducted similarly to the PS block, however the polymerization temperature was changed to 80 °C. For the photo-irradiated conditions, the polymerization was carried out at 60° C under 6W LED light irradiation. This LED light irradiation intensity was selected to maintain low free radical concentrations, to prevent the termination of the CTA. During the polymerization of both PS and PtBMA, DMF solvents were added to control the viscosity of the polymer solution.

In order to terminate the polymerization reaction, the tellurium group in CTA-1 was removed by adding PhSH (31 µL, 0.30 mmol) and reacting at 30 °C under 6 W LED irradiation for 3 hours. The polymers were then precipitated in 600 ml of a methanol and water mixture (8:2), then vacuum filtered and dried at 80 °C in a vacuum.

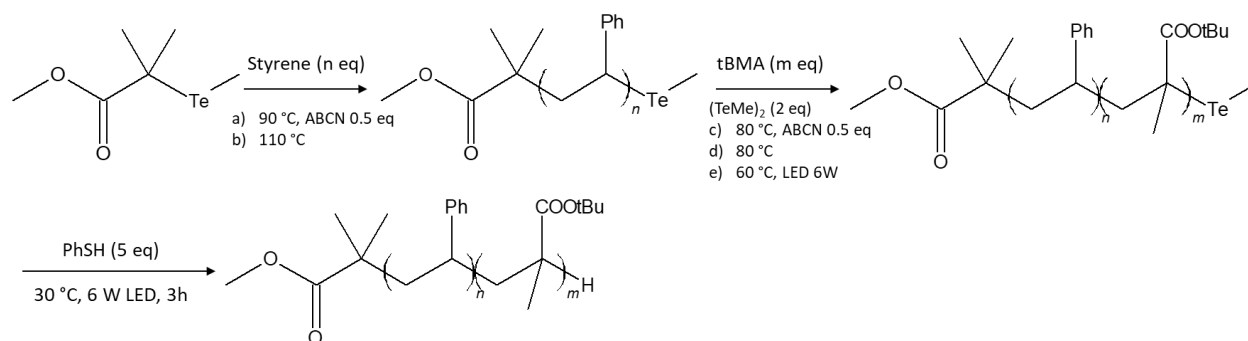


Figure 2.5 Homogeneous TERP polymerization of PS-b-PtBMA. Styrene polymerization under (a) Azo-initiated thermal condition (b) thermal condition. tBMA polymerization under (c) Azo-initiated thermal, (d) thermal, (e) photo-irradiated conditions. Reprinted with permission from Rattanakawin et al., *J. Photopolym. Sci. Technol.*, **2018**, 31 (5), 647-650. DOI: 10.2494/photopolymer.31.647. Copyright ©2018. Society of Photopolymer Science and Technology (SPST).

2.2.3 Emulsion polymerization of PMMA-b-PtBA

The polymerization of PMMA-b-PtBA was conducted by emulsion TERP polymerization. It can be summarized into two primary polymerization conditions: the photo-irradiated and the Azo-initiated thermal conditions (Figure 2.6). For both cases, tBA was polymerized first, followed by MMA polymerization. Those polymerization reactions were conducted in a sealed test tube. N₂ was introduced before sealing the tube to prevent oxidation of CTA-2. Then, the photo-irradiated condition of PtBA was conducted by dissolving CTA-2 (28.8 mg, 90 µmol), aqueous NaOH solution (180 µl, 0.503 mol L⁻¹, 90 µmol), and CTAB (0.85 g, 5.0 wt% to water) into the deaerated DI water (17 ml). After a homogeneous solution was obtained, tBA (1.06 ml, 7.2 mmol) was added to the solution and was polymerized with stirring at 65 °C under a 3 W white light-emitting diode (LED) lamp. Small aliquots (ca. 100 µl) of the emulsion were taken during the polymerization and extracted with deuterated chloroform (CDCl₃). The monomer

conversion was then determined by ^1H NMR (400 MHz). The molecular weight (M_n) and dispersity (D) were then evaluated by size-exclusion chromatography (SEC) at 40°C . After the PtBA polymerization, MMA (0.786 ml, 7.2 mmol) and the ditelluride compound (43.9 mg, 90 μmol) were added to the emulsion directly. It should be noted that the ditelluride compound was added to control the final D .^{18,19} The polymerization of MMA was similarly conducted at 65°C under an LED light. The CTA-2 was terminated by adding 2-aminoethanethiol (25.95 mg, 180 μmol) and reduced at 65°C under 6W LED irradiation.²⁰

For PMMA-b-PtBA with higher molecular weights, the synthesis was conducted under Azo-initiated thermal conditions instead.^{10,17} For these cases, 0.30 equivalents of aqueous ACVA were added to the monomer solution prior to the polymerization. The polymerization of the PtBA and subsequently PMMA block is then conducted at 65°C without the LED irradiation. It should be noted that prior to the PMMA polymerization 1.0 equivalent of $(\text{TeR})_2$ and an additional 0.30 equivalents of ACVA were added to the polymerization solution. After both blocks were polymerized, the polymer-end was terminated similarly to the photo-irradiated conditions.

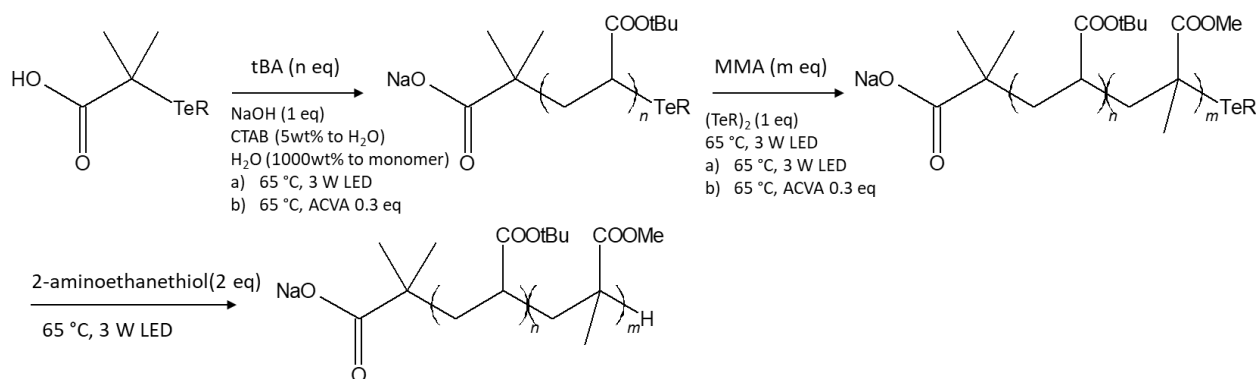


Figure 2.6 Emulsion TERP polymerization of PMMA-b-PtBA under (a) photo-irradiation and (b) Azo-initiated thermal conditions.

After the polymerization, the CTAB surfactant was removed by extraction, where the emulsion solution was mixed with 100 ml of chloroform (CHCl_3) and 150 ml of warm saturated sodium chloride (NaCl) solution. During the extraction, the CTAB micelles are broken and captured within the warm NaCl phase. Meanwhile, the polymer is dissolved in the CHCl_3 phase, as illustrated in Figure 2.7 (a). The extraction was repeated 10 times. The polymer was further purified by preparative gel permeation chromatography (GPC) equipped with JAIGEL-2H and JAIGEL-2.5H columns (Japan Analytical Industry Co., Ltd.) using CHCl_3 as an eluent with a flow rate of 3.8 ml/min (Figure 2.7 (b)). During the purification, larger molecular weight polymers were excluded from the column first and collected, followed by the CTAB and other contaminant molecules, as illustrated in Figure 2.7(c). The complete removal of CTAB was confirmed by ^1H NMR. The polymer solution was then precipitated in hexane. Then, the polymer was removed from the solution by centrifuge prior to drying at room temperature in a vacuum.

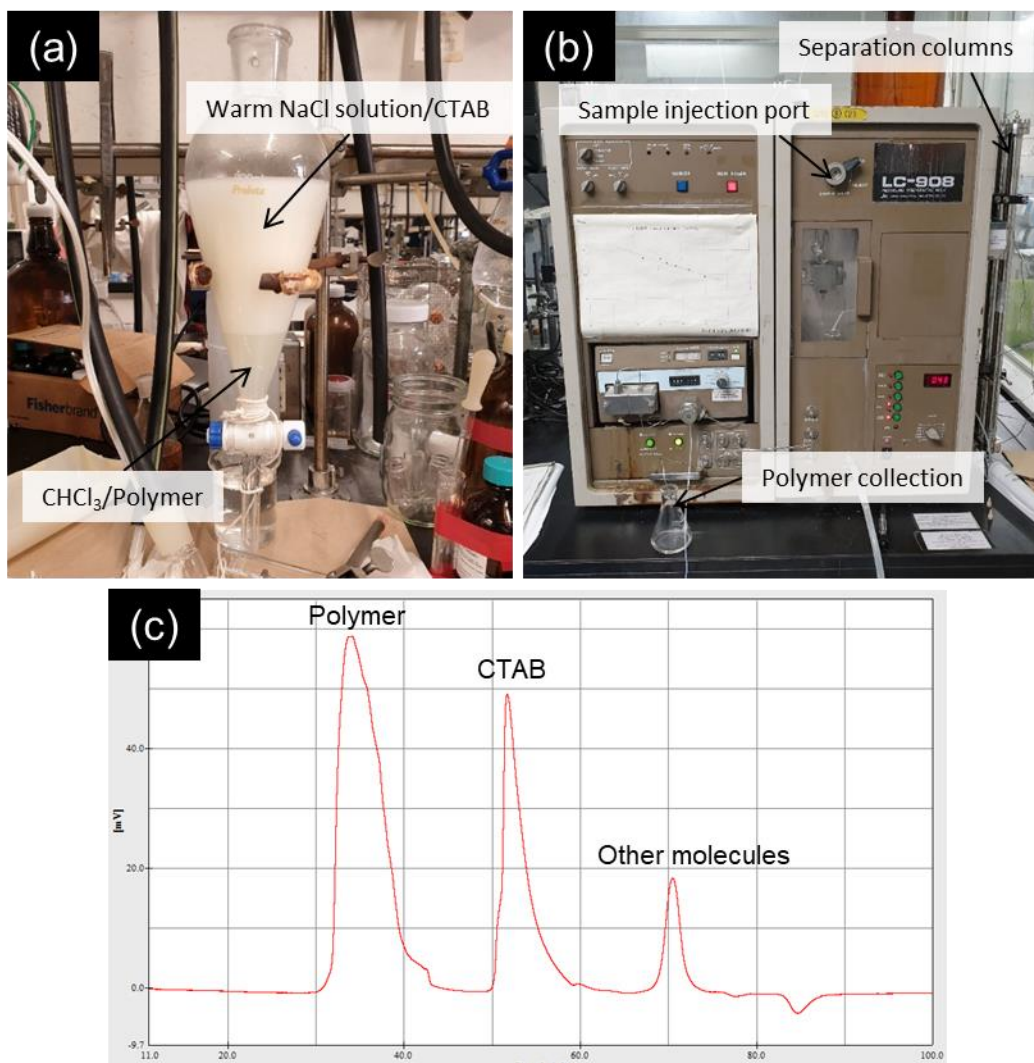


Figure 2.7 Removal of CTAB from PMMA-*b*-PtBA: (a) extraction with warm NaCl aqueous solution and CHCl₃, and (b) preparative GPC. (c) The elution time for the polymer, CTAB and other small molecule contaminants during the preparative GPC purification.

2.2.4 ¹H NMR Analysis

Figure 2.8 shows the result of monomer conversion in the homogeneous TERP polymerization of the PS-*b*-PtBMA process. The conversion of the styrene monomer was determined by comparing the protons at the β -position of styrene ($\delta = 5.225, 5.768$ ppm) to the backbone of PS ($\delta = 1.433, 1.846$ ppm, broad), as shown in Figure 2.8(a). The conversion of the tBMA monomer was determined from the protons at the β -position of tBMA ($\delta = 5.472, 6.001$ ppm). The proton changes before and after the PtBMA polymerization was estimated using the protons for the CH₃ group in ditelluride ($\delta = 2.663$) as a reference, as illustrated in Figure 2.8(b).

Figure 2.9 shows the ^1H NMR analysis of the monomer conversion by the emulsion TERP polymerization of PMMA-b-PtBA. The tBA conversion was calculated from the protons changed from the methyl group of tBA ($\delta = 1.495$ ppm) to PtBA ($\delta = 1.439$ ppm), as shown in Figure 2.9(a). Similarly, the MMA conversion was determined from the protons of the CH_3 group of MMA ($\delta = 3.755$ ppm) changed to PMMA ($\delta = 3.600$ ppm), as shown in Figure 2.9(b). ^1H NMR was also used to confirm the removal of CTAB after the purification, where CH_3 protons of CTAB ($\delta = 3.470$ ppm) should completely disappear (Figure 2.10). The ratio between the PtBA and PMMA blocks was also calculated by comparing the CH_3 protons of PtBA ($\delta = 1.439$ ppm) with those of PMMA ($\delta = 3.600$ ppm), as illustrated in Figure 2.10(b).

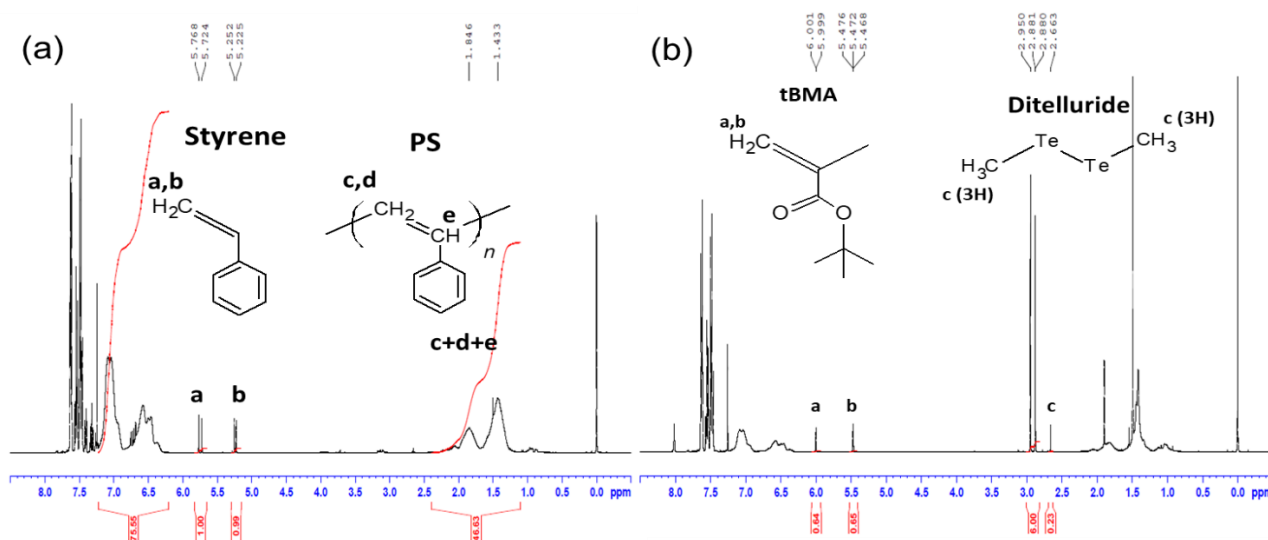


Figure 2.8 Monomer conversion by the homogeneous TERP polymerization of PS-b-PtBMA: (a) ^1H MNR spectra after the PS polymerization, (b) ^1H MNR spectra after the PtBMA polymerization

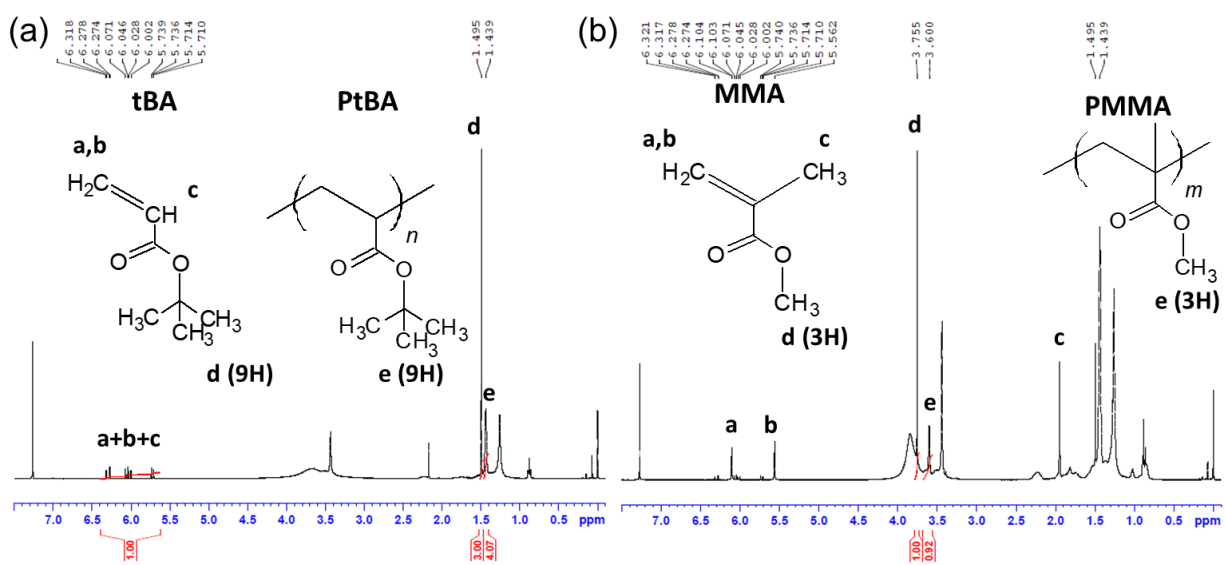


Figure 2.9 Monomer conversion by the emulsion TERP polymerization of PMMA-b-PtBA: (a) ¹H MNR spectra after the PtBA polymerization, (b) ¹H MNR spectra after the PMMAA polymerization

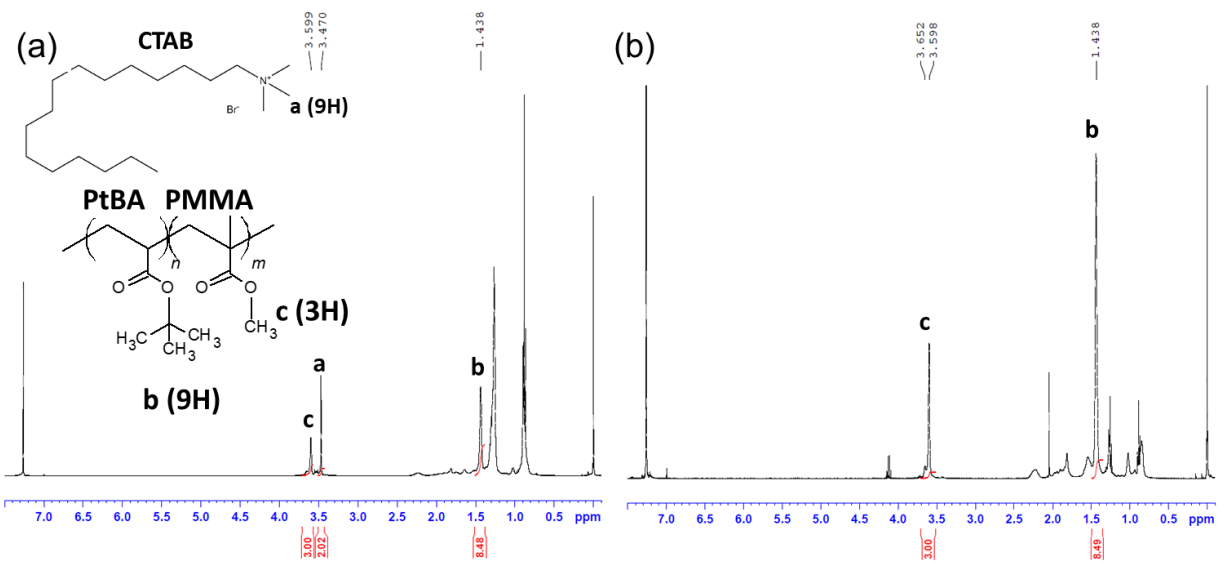


Figure 2.10 ¹H NMR of PMMA-b-PtBA (a) before and (b) after the purification by preparative GPC.

2.2.5 SEC measurement

SEC was performed by a machine equipped with two sequentially connected polystyrene (PSt) mixed gel columns (Shodex LF-604) at 40 °C using ultraviolet (UV) and refractive index (RI) detectors. In the case of the homogeneous TERP polymerization of PS-*b*-PMMA, CHCl₃ was used as an eluent at a flow rate of 1.0 mL/min. The SEC traces were calibrated against the PS and the PMMA standards for the PS and PtBMA polymerizations. For the emulsion TERP polymerization of PMMA-*b*-PtBA, THF was used as an eluent at a flow rate of 1.0 mL/min. The SEC traces were calibrated against the PMMA standard for both the PtBA and PMMA polymerizations.

2.2.6 DSC measurement

The glass transition temperature (T_g) of PMMA-*b*-PtBA was determined by the differential scanning calorimetry (DSC) (DSC7020, Hitachi Ltd., Japan). The measurements were conducted in the temperature range of 0-160 °C at the heating and cooling rates of 10 °C min⁻¹. T_g of PMMA-*b*-PtBA was determined from the second heating curve.

2.3 Results and Discussion

2.3.1 Homogeneous TERP polymerization of PS-*b*-PtBMA

The results of PS-*b*-PtBMA polymerized by the TERP in a homogeneous solution are summarized in Table 2.1. Case 1 represents the homogeneous TERP polymerization of low M_n PS-*b*-PtBMA examined under the Azo-initiated thermal conditions, where 133 and 67 equivalents to CTA-1 of styrene and tBMA monomers were added. Figure 2.11 shows the linear growth of M_n with the increase of monomer conversion for both PS and PtBMA blocks, indicating a living polymerization characteristic of the process.²¹ The SEC trace in Figure 2.12(a) shows narrow molecular weight distributions, $\mathcal{D} = 1.22$ and 1.18, for the PS and the PtBMA blocks, suggesting that a well-controlled block copolymer was synthesized.

Case 2 shows the result of PS-*b*-PtBMA polymerized under the same conditions as Case 1 except the amount of styrene and tBMA. The amounts of styrene and tBMA were increased to 400 and 200 equivalents in Case 2. Figure 2.12(b) shows that after 93 hours of polymerization, the styrene block had a narrow $\mathcal{D} = 1.32$. However, for the PtBMA block, a prominent second peak appeared at the same elution time as the PS block, indicating that many dead polymers were formed during the styrene polymerization. From the SEC trace, approximately 60% of the active species were deactivated before the PtBMA polymerization.

In order to reduce the number of dead polymers, the PS block polymerization was changed to the thermal condition scheme, and the PtBMA block polymerization was investigated under various conditions (Case 3-5). The \mathcal{D} of the PS block was lower than in Case 2, as indicated from the SEC trace shown in Figure 2.12(c-e). However, with approximately 30% inactivated CTA, the dead polymer peaks still appeared in all PtBMA polymerization conditions. For the Azo-initiated thermal and thermal polymerizations, the final \mathcal{D} of PS-*b*-PtBMA was lower than in Case 2, indicating improved controllability. For the photo-irradiated condition, i.e., Case 5, broader molecular weight

distribution was observed, most likely due to the excess free radicals from the photo-irradiation process with 6W LED irradiation.

While well-controlled homogeneous TERP polymerization was achieved for PS-b-PtBMA with low M_n , the formation of the dead polymers made it still unsuitable for high M_n polymerization. It is speculated that the dead polymers are mainly formed due to the addition of the solvents, which are required to maintain a suitable polymerization solution viscosity. This solvent addition increases the polymerization time to achieve high monomer conversion and results in a higher degree of termination reactions.²² Because of this, a different approach is required to achieve a higher degree of polymerization while maintaining precise control over the polymer ratio, M_n and \bar{D} .

Table 2.1 Homogeneous TERP polymerization of PS-b-PtBMA. Reprinted with permission from Rattanakawin et al., *J. Photopolym. Sci. Technol.*, **2018**, 31 (5), 647-650. DOI: 10.2494/photopolymer.31.647. Copyright ©2018. Society of Photopolymer Science and Technology (SPST).

Case	Styrene					PtBMA					Dead Polymer (%)
	n	Cond. ^[a]	Conv. /time	$M_n \times 10^3$	\bar{D}	m	Cond. ^[a]	Conv./time	$M_n \times 10^3$	\bar{D}	
1	133	a	90%/ 5 h	13.5	1.22	67	c	90%/ 16 h	23.8	1.18	13%
2	400	a	92%/ 93 h	20.1	1.32	200	c	83%/ 72 h	61.2	1.48	60%
3	400	b	92%/ 62 h	35.3	1.17	200	c	95%/ 18 h	54.7	1.31	30%
4	400	b	92%/ 62 h	35.3	1.17	200	d	80%/ 45 h	60.2	1.33	30%
5	400	b	92%/ 62 h	35.3	1.17	200	e	71%/ 34 h	55.8	1.55	30%

^[a] Refer to Figure 2.5 for the polymerization conditions

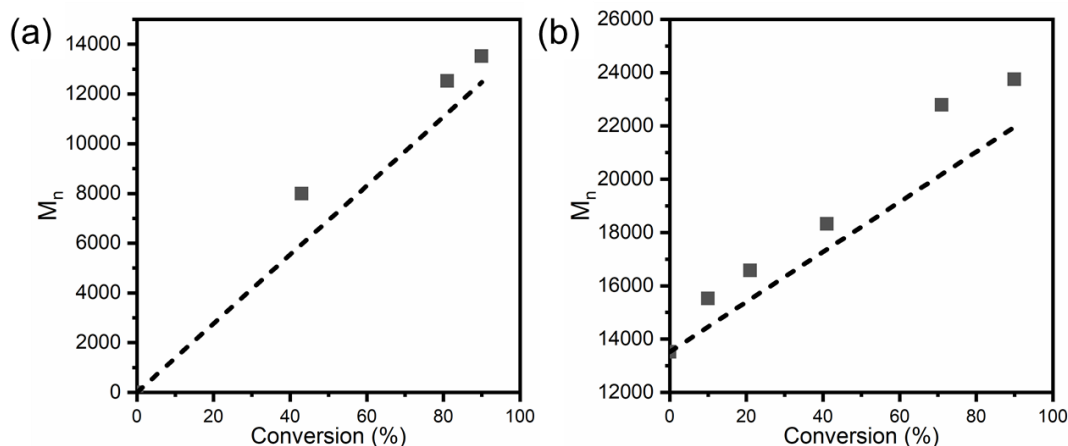


Figure 2.11 Molecular weight change with monomer conversion for (a) PS and (b) PtBMA for Case 1. The dashed line shows the theoretical M_n vs. monomer conversion relationship.

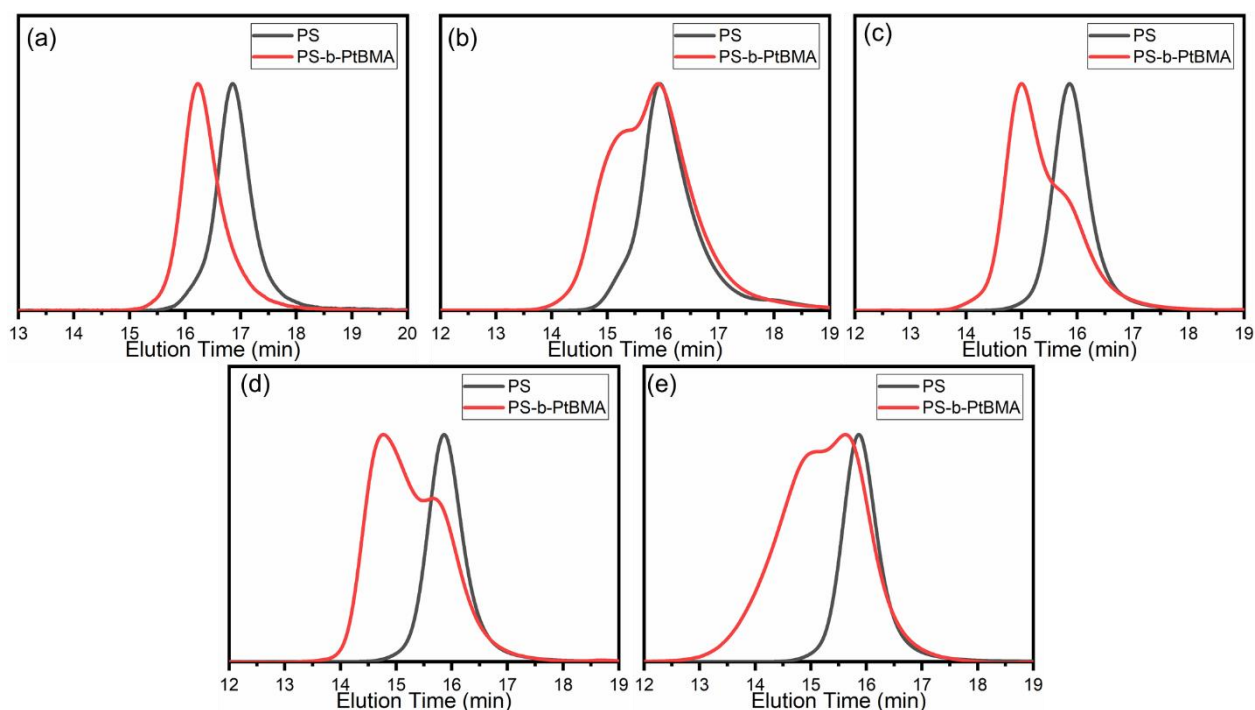


Figure 2.12 SEC traces for PS-b-PtBMA synthesized by homogeneous TERP polymerization: (a) Case 1, (b) Case 2, (c) Case 3, (d) Case 4 and (e) Case 5. Reprinted with permission from Rattanakawin et al., *J. Photopolym. Sci. Technol.*, **2018**, *31* (5), 647-650. DOI: 10.2494/photopolymer.31.647. Copyright ©2018. Society of Photopolymer Science and Technology (SPST).

2.3.2 Emulsion TERP polymerization of PMMA-b-PtBA Under Photo-Irradiated Conditions

Emulsion TERP polymerization was used to reduce the formation of dead polymers. In this study, CTA-2 (Figure 2.4(a)) was used in water with CTAB (5 wt% to water) as a surfactant. CTA-2 was neutralized to the corresponding sodium carboxylates with aqueous NaOH (1 equivalent) to dissolve in water, as shown in Figure 2.6. The tBA polymerization was then conducted and subsequently MMA, by the photo-irradiated conditions at 65 °C under 3 W LED light. The results are summarized in Table 2.2.

In Case 6, low M_n PMMA-b-PtBA synthesis was examined, where 80 equivalents of tBA and MMA monomer to CTA-2 were polymerized. Linear M_n growth was observed with increasing monomer conversion, confirming a living polymerization characteristic for both PtBA and PMMA polymerizations, as shown in Figure 2.13. The discrepancy between the theoretical and the experimental M_n , especially for the PtBA block, could be due to an inaccurate comparison of the PtBA molecular weight to the PMMA calibration standards.⁸ Nevertheless, the weight fraction of the PtBA block (ϕ_{PtBA}) observed from $^1\text{H NMR}$ ($\phi_{\text{PtBA}} = 58.9 \text{ wt\%}$) was close to the theoretical value ($\phi_{\text{PtBA}} = 56.1 \text{ wt\%}$), suggesting that the correct amount of monomer was added. The SEC trace of Case 1 shown in Figure 2.14(a) shows a narrow D for both PtBA and PMMA blocks without the formation of dead polymers.

In Case 7, the M_n of PMMA-b-PtBA increases while maintaining the tBA:MMA monomer ratio similar to Case 6, where 300 equivalents of tBA and MMA were polymerized. From the SEC trace shown in Figure 2.14(b), the polymerization of both PtBA and PMMA blocks showed a narrow $\mathcal{D} = 1.16$ and 1.25. While a slight shoulder peak was observed after the PMMA polymerization, the amount of dead polymer was only 12%, relatively low compared to the homogeneous TERP polymerization in the previous section.

PMMA-b-PtBA with the different PtBA: PMMA ratios were polymerized in Case 8-11. In all cases, the SEC trace shows a narrow \mathcal{D} ($\mathcal{D} < 1.5$) and a relatively small number of dead polymers, as shown in Figure 2.14(c-f), indicating the well-controlled polymerization of PMMA-b-PtBA.

Table 2.2 Emulsion TERP polymerization of PMMA-b-PtBA under photo-irradiated conditions

Case	PtBA				PMMA				$\phi_{\text{PtBA}}^{[a]}$ (wt%)	Dead Polymer
	n	Conv. /time	M_n $\times 10^3$	\mathcal{D}	m	Conv. /time	M_n $\times 10^3$	\mathcal{D}		
6	80	96%/ 14 h	15.3	1.22	80	92%/ 6 h	25.5	1.28	58.9 wt%	-
7	300	89%/ 20 h	32.8	1.16	300	88%/ 10 h	58.4	1.25	54.2 wt%	12%
8	150	87%/ 4 h	12.8	1.32	450	92%/ 3 h	51.6	1.30	31.0 wt%	4%
9	200	90%/ 6h	19.2	1.15	400	95%/ 4 h	54.6	1.38	34.3 wt%	8%
10	400	90%/ 14 h	34.5	1.13	200	91%/ 10 h	49.2	1.18	72.2 wt%	-
11	450	89%/ 12 h	40.4	1.22	150	87%/ 6 h	47.3	1.25	82.8 wt%	-

^[a] The weight fraction of PtBA was estimated by ¹H NMR as shown in Figure 2.10(b).

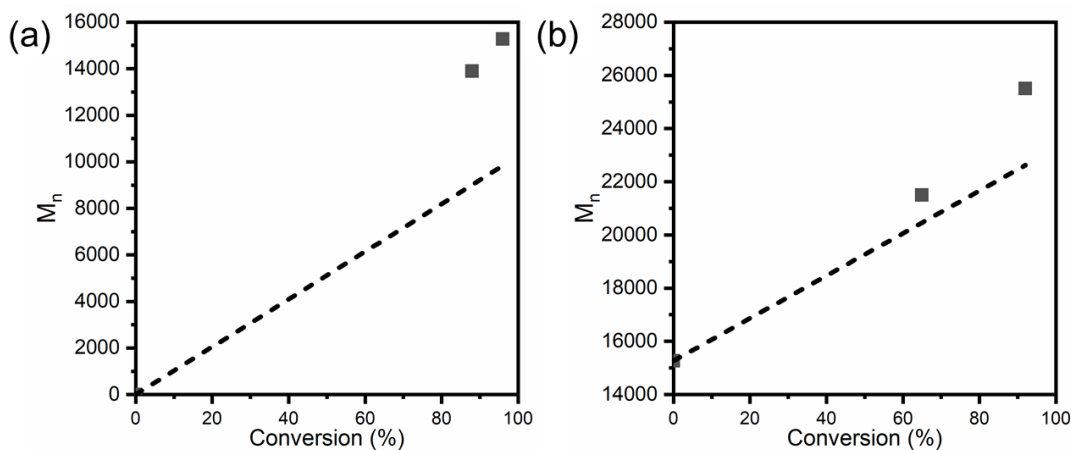


Figure 2.13 Molecular weight change with monomer conversion for (a) PtBA and (b) PMMA for Case 6. The dashed line represents the theoretical M_n vs. monomer conversion relationship.

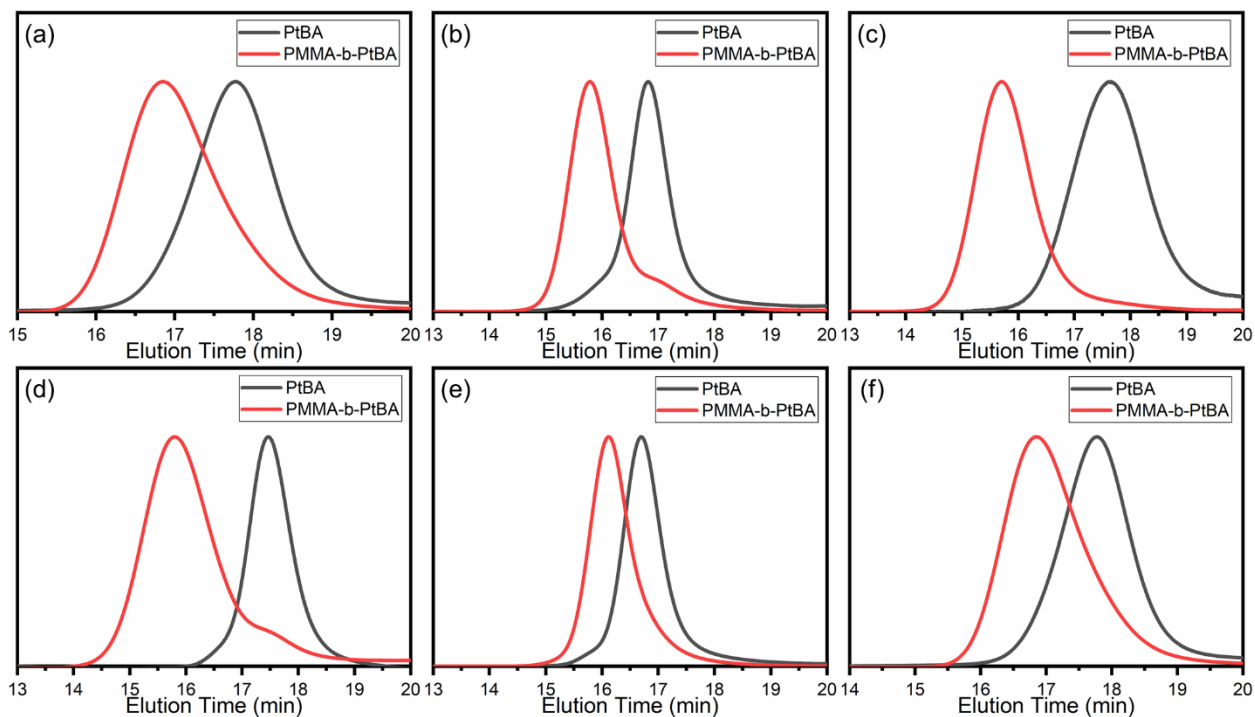


Figure 2.14 SEC traces for PMMA-b-PtBMA synthesized by emulsion TERP polymerization using the photo-initiated conditions: (a) Case 6, (b) Case 7, (c) Case 8, (d) Case 9, (e) Case 10 and (f) Case 11

The thermal properties of PMMA-b-PtBA synthesized in Case 6-11 were investigated by DSC. The glass transition temperatures, T_g , of PtBA and PMMA were obtained from the 2nd heating curves shown in Figure 2.15(a). The results are summarized in Table 2.3. For Cases 6-10, two inflection points corresponding to PtBA and PMMA were observed at 41-47 °C and 92-115 °C, respectively. On the other hand, for Case 11, only one T_g was observed at 34 °C. It is speculated that insufficient PtBA conversion may occur and some of the unreacted tBA monomers could be polymerized after adding MMA, as shown in Figure 2.16. As shown in Figure 2.15(b), T_g of the PMMA block decreases drastically with ϕ_{PtBA} , confirming that the unreacted tBA indeed polymerized with MMA. Besides the thermal properties, the self-assembly of PMMA-b-PtBA may be affected by PtBA. For this reason, a higher tBA monomer conversion was required to mitigate the issue. However, a significantly longer polymerization time was required to achieve a higher tBA conversion, resulting in the formation of dead polymers.

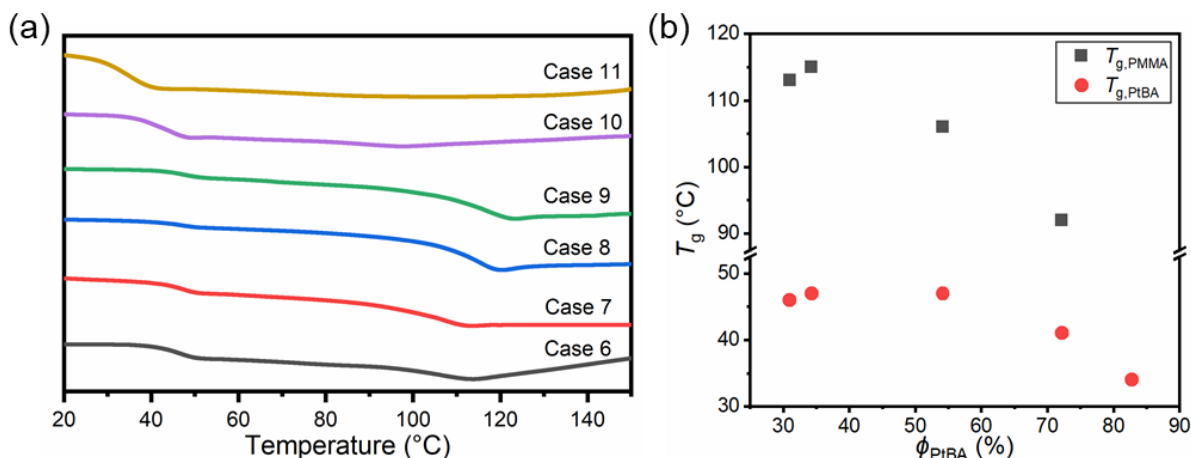


Figure 2.15 (a) DSC 2nd heating curves for PMMA-b-PtBA synthesized using photo-irradiated conditions. (b) Relationship between the PtBA weight fraction and the T_g of PMMA-b-PtBA with similar M_n (Case 7-11).

Table 2.3 Glass transition temperatures for PMMA-b-PtBA synthesized using photo-irradiated conditions

Case	$M_n \times 10^3$	ϕ_{PtBA} (wt%)	$T_{g,\text{PtBA}}$ (°C)	$T_{g,\text{PMMA}}$ (°C)
6	25.5	58.9	45	108
7	58.4	54.2	47	106
8	51.6	31.0	46	113
9	54.6	34.3	47	115
10	49.2	72.2	41	92
11	47.3	82.8	34	-

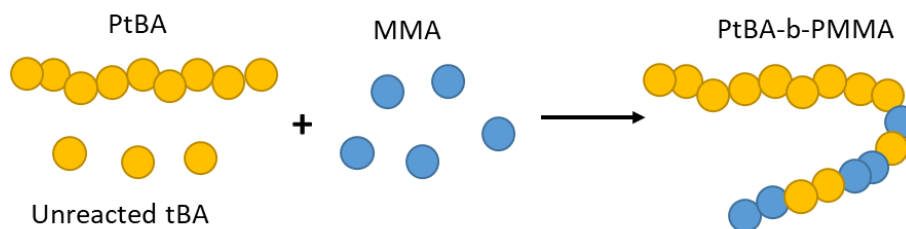


Figure 2.16 Effect of the unreacted tBA monomers during the PMMA polymerization

2.3.3 Emulsion TERP polymerization of PMMA-b-PtBA Under Azo-Initiated Thermal Conditions

As discussed in the previous section, a high tBA monomer conversion is required to reduce the unreacted tBA monomers during the MMA polymerization. The Azo-initiated thermal conditions were employed instead of the photo-irradiated conditions to increase the tBA conversion. An Azo-compound, ACVA, was added to create and transfer the free radicals to the CTA for polymerization. The number of free radicals in the emulsion could be adjusted

depending on the amount of ACVA.¹⁷ The optimal ACVA concentration was determined by polymerizing PtBA with 600 equivalent tBA monomer to the CTA. SEC traces of PtBA, polymerized under the Azo-initiated thermal conditions with 0.3, 0.5, and 1 equivalent of ACVA, are summarized in Figure 2.17 and Table 2.4. For higher ACVA concentrations, shorter foaming times were observed to achieve more than 95% tBA conversions. However, the \mathcal{D} increases drastically due to the number of free radicals generated during the polymerization. For this reason, ACVA with 0.3 equivalents was selected for the PMMA-b-PtBA polymerization under the Azo-initiated thermal conditions. It provides narrow $\mathcal{D} = 1.33$ while maintaining a short polymerization time compared to photo-irradiated conditions.

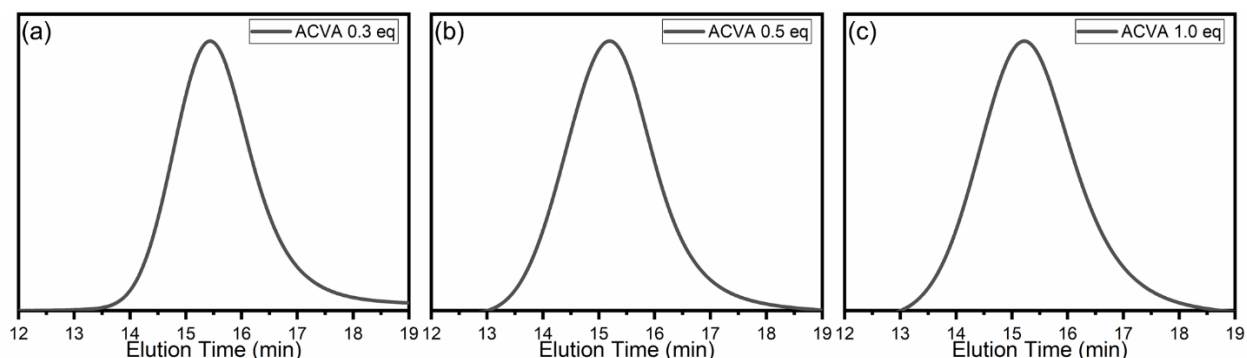


Figure 2.17 SEC traces for PtBA synthesized by emulsion TERP polymerization using Azo-initiated thermal conditions with (a) 0.3, (b) 0.5 and (c) 1.0 equivalent ACVA to the CTA

Table 2.4 Emulsion TERP polymerization of PtBA with different ACVA concentrations

ACVA (eq.)	Conv. /time	$M_n \times 10^3$	\mathcal{D}
0.3	95%/ 8 h	73.0	1.33
0.5	97%/ 3 h	85.3	1.61
1.0	95%/ 1 h	73.0	1.75

PMMA-b-PtBA with 300 equivalents tBA and MMA was polymerized in Case 12 to compare the Azo-initiated thermal and the photo-irradiated conditions. For the PtBA block, 95% tBA conversion was achieved after 4 hours, a notably shorter polymerization time than in Case 7 (Table 2.5). The SEC trace (Figure 2.18(a)) indicated that the final PMMA-b-PtBA had $M_n = 73800$ and $\mathcal{D} = 1.32$, and no dead polymer after the polymerization. This well-controlled synthesis was observed even for high molecular weight PMMA-b-PtBA with $M_n = 117300$ and 233200, as shown in Figures 2.18(b) and (c), respectively.

Table 2.5 Emulsion TERP polymerization of PMMA-b-PtBA under the Azo-initiated thermal conditions

Case	PtBA				PMMA				$\phi_{\text{PtBA}}^{[a]}$ (wt%)	Dead Polymer
	n	Conv. /time	M_n $\times 10^3$	\mathcal{D}	m	Conv. /time	M_n $\times 10^3$	\mathcal{D}		
12	300	95% / 4 h	49.3	1.28	300	94% / 14 h	73.8	1.32	56.6 wt%	-
13	600	95% / 8 h	73.0	1.33	600	89% / 11 h	117.3	1.29	55.1 wt%	-
14	1200	96% / 23 h	152.4	1.41	1200	89% / 28 h	233.2	1.34	56.6 wt%	-

^[a] The weight fraction of PtBA was estimated by ¹H NMR as shown in Figure 2.10(b).

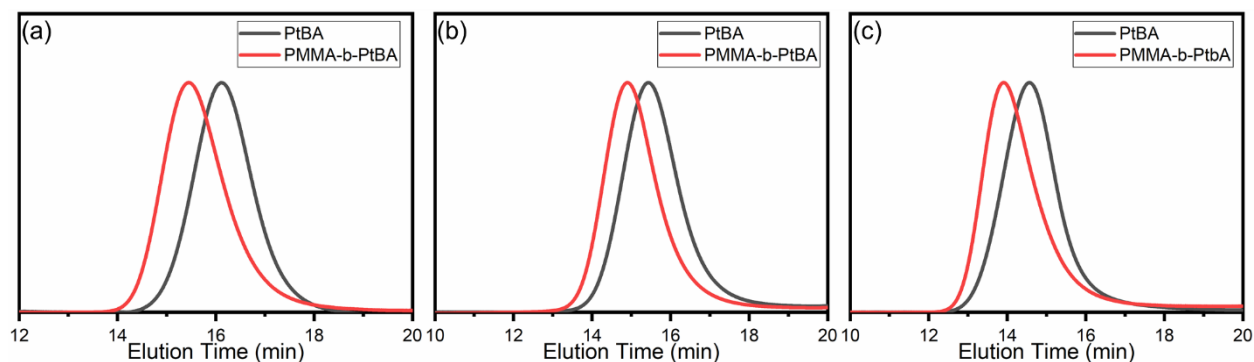


Figure 2.18 SEC traces for PMMA-b-PtBA synthesized by emulsion TERP polymerization using the Azo-initiated thermal conditions: (a) Case 12, (b) Case 13 and (c) Case 14

Figure 2.19 shows the DSC 2nd heating curves for Case 12-14. T_g of PtBA and PMMA blocks were obtained from the curves. As indicated in Table 2.6, T_g of PtBA block was found at 43 °C, similar to in Case 7 ($T_g = 47$ °C). However, T_g of PMMA in Cases 12-14 ($T_g = 116$ -118 °C) were significantly higher than in Case 7 ($T_g = 106$ °C). This confirms that the Azo-initiated thermal conditions with a high tBA monomer conversion were able to prevent the polymerization of the tBA block after the addition of the MMA monomer.

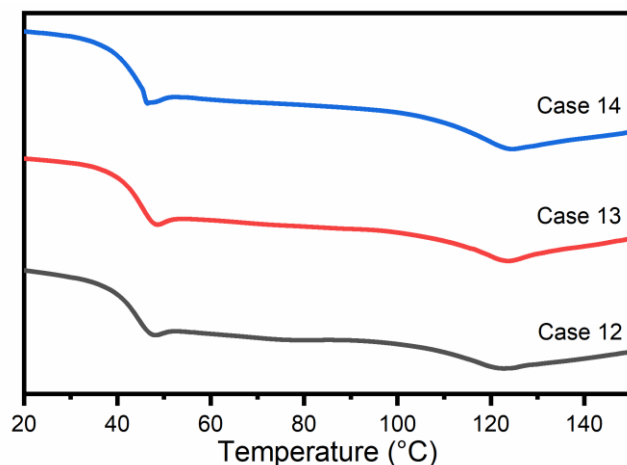


Figure 2.19 DSC 2nd heating curves for PMMA-b-PtBA synthesized by Azo-initiated thermal conditions.

Table 2.6 Glass transition temperatures for PMMA-b-PtBA synthesized using Azo-initiated thermal conditions

Case	$M_n \times 10^3$	ϕ_{PtBA} (wt%)	$T_{g,\text{PtBA}}$ (°C)	$T_{g,\text{PMMA}}$ (°C)
12	73.8	56.6	43	117
13	117.3	55.1	43	118
14	233.2	56.6	43	116

In order to compare the photo-irradiated conditions and the azo-initiated thermal conditions, the copolymerization of the unreacted tBA was calculated using Equation 2.1,²³ where f_{tBA} and f_{MMA} are the mole fraction of tBA and MMA in the feed, and F_{tBA} and F_{MMA} are the mole fractions in the copolymer. For our process, f_{tBA} expresses the unreacted tBA units and be estimated from the conversion during PtBA polymerization. The monomer reactivity ratios r_{tBA} and r_{MMA} express the preferential addition of the same monomer unit to the other monomer species. For tBA and MMA radical copolymerization systems, r_{tBA} and r_{MMA} were reported as 0.60 and 2.14, respectively.²⁴ This suggests that both the tBA and MMA radicals preferentially polymerize MMA monomers, and tBA is added gradually throughout the chain. The ratio of the tBA monomer in the PMMA chain ($F_{\text{tBA}}/F_{\text{MMA}}$) is summarized in table 2.7. The $F_{\text{tBA}}/F_{\text{MMA}}$ ranged from 1.9-16 mol% for photo-irradiated conditions, whereas the azo-initiated thermal conditions were approximately 1.9-2.4 mol%. These estimations are consistent with the $T_{g,\text{PMMA}}$ results summarized in Table 2.3 and Table 2.6, and suggest that the azo-initiated thermal condition is effective in preventing the polymerization of unreacted tBA monomers.

$$\frac{F_{\text{tBA}}}{F_{\text{MMA}}} = \frac{f_{\text{tBA}}(r_{\text{tBA}}f_{\text{tBA}} + f_{\text{MMA}})}{f_{\text{MMA}}(r_{\text{MMA}}f_{\text{MMA}} + f_{\text{tBA}})} \quad (2.1)$$

Table 2.7 Emulsion TERP polymerization of PMMA-b-PtBA under the Azo-initiated thermal conditions

Case	Unreacted tBA (eq.)	MMA (eq.)	f_{tBA} (%)	f_{MMA} (%)	F_{tBA}/F_{MMA} (%)
6	3	80	3.8	96.2	1.8
7	33	300	9.9	90.1	5.2
8	20	450	4.2	95.8	2.0
9	20	400	4.7	95.3	2.3
10	40	200	16.7	83.3	9.5
11	50	150	24.8	75.2	16.0
12	15	300	4.8	95.2	2.4
13	30	600	4.8	95.2	2.4
14	48	1200	3.8	96.1	1.9

2.4 Conclusion

In this chapter, the polymerizations of PS-b-PtBMA and PMMA-b-PtBA by TERP were discussed. PS-b-PtBMA was synthesized using the homogeneous TERP. Low M_n PS-b-PtBMA was synthesized using the Azo-initiated thermal conditions, and the well-controlled polymerization with low D and the low dead polymer was achieved. However, D and the dead polymers increased significantly in the higher M_n PS-b-PtBMA cases. Different polymerization conditions, including the thermal and photo-irradiated conditions, were also tested for the synthesis, however many dead polymers were still formed due to the viscosity of the polymerization solution.

Emulsion TERP polymerization was applied to synthesize PMMA-b-PtBA instead of homogeneous TERP polymerization to reduce the formation of dead polymers. The photo-irradiated conditions were employed to successfully synthesize PMMA-b-PtBA with $M_n = 25500$ to 58400 with different PtBA weight fractions (ϕ_{PtBA}). However, the glass transition temperature of PMMA-b-PtBA, especially the PMMA block, decreases with ϕ_{PtBA} , indicating that the monomer conversion for tBA was insufficient, and the unreacted tBA monomer was polymerized along with MMA.

PMMA-b-PtBA with the higher tBA monomer conversions were achieved under the Azo-initiated thermal conditions. By optimizing the amount of Azo-initiator, ACVA, well-controlled polymerization of PMMA-b-PtBA with high M_n was accomplished. Furthermore, the polymerization of unreacted tBA monomer was suppressed, as indicated by the higher PMMA T_g , when compared to PMMA-b-PtBA synthesized under the photo-irradiated conditions.

2.5 References

- (1) Kojima, J.; Takada, T.; Jinno, F. Thin Microcellular Plastic Sheet Incorporating Designed Foaming Patterns Made by Photochemical Foaming Technology. *J. Cell. Plast.* **2007**, *43* (2), 103–109. <https://doi.org/10.1177/0021955X06076573>.
- (2) Corrigan, N.; Jung, K.; Moad, G.; Hawker, C. J.; Matyjaszewski, K.; Boyer, C. Reversible-Deactivation Radical Polymerization (Controlled/Living Radical Polymerization): From Discovery to Materials Design and Applications. *Prog. Polym. Sci.* **2020**, *111*, 101311. <https://doi.org/10.1016/J.PROGPOLYMSCI.2020.101311>.
- (3) Matyjaszewski, K.; Spanswick, J. Controlled/Living Radical Polymerization. *Mater. Today* **2005**, *8* (3), 26–33. [https://doi.org/10.1016/S1369-7021\(05\)00745-5](https://doi.org/10.1016/S1369-7021(05)00745-5).
- (4) Nicolas, J.; Guillaneuf, Y.; Lefay, C.; Bertin, D.; Gigmès, D.; Charleux, B. Nitroxide-Mediated Polymerization. *Prog. Polym. Sci.* **2013**, *38* (1), 63–235. <https://doi.org/10.1016/J.PROGPOLYMSCI.2012.06.002>.
- (5) Sciannone, V.; Jérôme, R.; Detrembleur, C. In-Situ Nitroxide-Mediated Radical Polymerization (NMP) Processes: Their Understanding and Optimization. *Chem. Rev.* **2008**, *108* (3), 1104–1126. <https://doi.org/10.1021/CR0680540>.
- (6) Matyjaszewski, K. Atom Transfer Radical Polymerization (ATRP): Current Status and Future Perspectives. *Macromolecules* **2012**, *45* (10), 4015–4039. <https://doi.org/10.1021/MA3001719>.
- (7) Faber, M.; Hofman, A. H.; Loos, K.; Brinke, G. ten. Highly Ordered Structure Formation in RAFT-Synthesized PtBOS-b-P4VP Diblock Copolymers. *Macromol. Rapid Commun.* **2016**, *37* (11), 911–919. <https://doi.org/10.1002/MARC.201600052>.
- (8) Fan, W.; Yamago, S. Synthesis of Poly(N-Vinylamide)s and Poly(Vinylamine)s and Their Block Copolymers by Organotellurium-Mediated Radical Polymerization. *Angew. Chemie Int. Ed.* **2019**, *58* (21), 7113–7116. <https://doi.org/10.1002/ANIE.201902940>.
- (9) Yamago, S. Photoactivation of Organotellurium Compounds in Precision Polymer Synthesis: Controlled Radical Polymerization and Radical Coupling Reactions. *Bull. Chem. Soc. Jpn.* **2019**, *93* (2), 287–298. <https://doi.org/10.1246/BCSJ.20190339>.
- (10) Goto, A.; Kwak, Y.; Fukuda, T.; Yamago, S.; Kazunori, I.; Nakajima, M.; Yoshida, J. Mechanism-Based Invention of High-Speed Living Radical Polymerization Using Organotellurium Compounds and Azo-Initiators. *J. Am. Chem. Soc.* **2003**, *125* (29), 8720–8721. <https://doi.org/10.1021/JA035464M>.
- (11) Fan, W.; Nakamura, Y.; Yamago, S. Synthesis of Multivalent Organotellurium Chain-Transfer Agents by Post-Modification and Their Applications in Living Radical Polymerization. *Chem. – A Eur. J.* **2016**, *22* (47), 17006–17010. <https://doi.org/10.1002/CHEM.201603682>.
- (12) Kaya, K.; Seba, M.; Fujita, T.; Yamago, S.; Yagci, Y. Visible Light-Induced Free Radical Promoted Cationic Polymerization Using Organotellurium Compounds. *Polym. Chem.* **2018**, *9* (48), 5639–5643.

- <https://doi.org/10.1039/C8PY01380B>.
- (13) Nakamura, Y.; Ebeling, B.; Wolpers, A.; Monteil, V.; D'Agosto, F.; Yamago, S. Controlled Radical Polymerization of Ethylene Using Organotellurium Compounds. *Angew. Chemie* **2018**, *130* (1), 311–315. <https://doi.org/10.1002/ANGE.201709946>.
- (14) Fan, W.; Tosaka, M.; Yamago, S.; Cunningham, M. F. Living Ab Initio Emulsion Polymerization of Methyl Methacrylate in Water Using a Water-Soluble Organotellurium Chain Transfer Agent under Thermal and Photochemical Conditions. *Angew. Chemie Int. Ed.* **2018**, *57* (4), 962–966. <https://doi.org/10.1002/ANIE.201710754>.
- (15) Yamago, S. Precision Polymer Synthesis by Degenerative Transfer Controlled/Living Radical Polymerization Using Organotellurium, Organostibine, and Organobismuthine Chain-Transfer Agents. *Chem. Rev.* **2009**, *109* (11), 5051–5068. <https://doi.org/10.1021/CR9001269>.
- (16) Jiang, Y.; Fan, W.; Tosaka, M.; Cunningham, M. F.; Yamago, S. Fabrication of Structurally Controlled Poly(n-Butyl Acrylate) Particles by Ab Initio Emulsion Organotellurium-Mediated Radical Polymerization. Synthesis of High Molecular Weight Homo and Block Copolymers. *Macromolecules* under revision.
- (17) Nakamura, Y.; Kitada, Y.; Kobayashi, Y.; Ray, B.; Yamago, S. Quantitative Analysis of the Effect of Azo Initiators on the Structure of α -Polymer Chain Ends in Degenerative Chain-Transfer-Mediated Living Radical Polymerization Reactions. *Macromolecules* **2011**, *44* (21), 8388–8397. <https://doi.org/10.1021/MA201761Q>.
- (18) Yamago, S.; Kazunori Iida, A.; Yoshida, J. Tailored Synthesis of Structurally Defined Polymers by Organotellurium-Mediated Living Radical Polymerization (TERP): Synthesis of Poly(Meth)Acrylate Derivatives and Their Di- and Triblock Copolymers. *J. Am. Chem. Soc.* **2002**, *124* (46), 13666–13667. <https://doi.org/10.1021/JA027599I>.
- (19) Kwak, Y.; Tezuka, M.; Goto, A.; Fukuda, T.; Yamago, S. Kinetic Study on Role of Ditelluride in Organotellurium-Mediated Living Radical Polymerization (TERP). *Macromolecules* **2007**, *40* (6), 1881–1885. <https://doi.org/10.1021/MA0623385>.
- (20) Yamago, S.; Matsumoto, A. Arylthiols as Highly Chemoselective and Environmentally Benign Radical Reducing Agents. *J. Org. Chem.* **2008**, *73* (18), 7300–7304. <https://doi.org/10.1021/JO801200B>.
- (21) Quirk, R. P.; Lee, B. Experimental Criteria for Living Polymerizations. *Polym. Int.* **1992**, *27* (4), 359–367. <https://doi.org/10.1002/PI.4990270412>.
- (22) Goto, A.; Fukuda, T. Kinetics of Living Radical Polymerization. *Prog. Polym. Sci.* **2004**, *29* (4), 329–385. <https://doi.org/10.1016/J.PROGPOLYMSCI.2004.01.002>.
- (23) Odian, G. Chain Copolymerization. *Princ. Polym.* **2004**, 464–543. <https://doi.org/10.1002/047147875X.CH6>.
- (24) Bujak, P.; Matlengiewicz, M.; Pasich, M.; Henzel, N. Microstructure of Methyl Methacrylate/Tert-Butyl Acrylate Copolymer Characterized by ¹³C NMR Spectroscopy. *Polym. Bull.* **2010**, *64* (3), 259–273. <https://doi.org/10.1007/S00289-009-0161-9/FIGURES/8>.

Chapter 3 Preparation of Highly-Ordered Nanocellular Foams by UV-induced Chemical Foaming from Self-Assembled PMMA-b-PtBA

3.1 Introduction

As discussed in the General Introduction in Chapter 1, a great interest in the fabrication of nanocellular foams has been increasing due to their superior mechanical, optical and thermal insulation properties. Through enhancing the ordering of the cell structures, it is expected that the properties of nanocellular foams could be further improved.¹⁻⁴ However, scarce research has been done for either fabricating or evaluating the properties of highly-ordered nanocellular foams because creating such materials by conventional foaming processes is difficult. In this chapter, a unique method to produce highly-ordered nanocellular foams is proposed by incorporating self-assembled block copolymer templates to a UV-induced chemical foaming process.

The concept of using self-assembled block copolymers as a template for creating nanocellular foams has been widely explored for the physical foaming process. The self-assembled block copolymers that has been tested were poly(perfluorooctylethyl methacrylate) (PFMA),⁵⁻⁸ poly(4-(perfluorooctylpropyloxy)styrene) (PFS),⁹ poly(1,1,2,2-tetrahydroperfluorodecyl acrylate) (PFDA)¹⁰ and poly(ethylene glycol) (PEG)¹¹⁻¹³, which contained a CO₂ philic block. One of the reasons is that CO₂ has been preferably used as a physical blowing agent for microcellular foaming. The high solubility of the physical blowing agent in the CO₂-philic block and the interface between the two block domains promote the cell nucleation and result in the production of nanocellular foam with relatively uniform cell size.⁷⁻⁹ The cell structure of the nanocellular foams could be adjusted by the polymer specification or process parameters, such as the gas saturation pressure, pressure drop rate, foaming temperature, or foaming time. Nevertheless, it is challenging to produce nanocellular foams by physical foaming of self-assembled block copolymers due to the reconstruction of the self-assembled structure and plasticization effect of CO₂.^{7-9,11,14} The reconstruction of the self-assembled morphology mainly occurs during the gas saturation process. As the blowing agent selectively dissolves in the CO₂-philic domains, the effective volume fraction of the block copolymer changes. Furthermore, CO₂ may also decrease the effective segregation strength between the CO₂-philic and matrix domains. Depending on the amount of CO₂ dissolved in the domains, the self-assembled morphology might go through either a reconstruction or transition to a disordered state. The plasticization effect of CO₂ on the block copolymer mainly affects the formation of the cell structure during the nanocellular foaming process. When the chain mobility was enhanced in the matrix domain more than the disperse domains and the viscosity of the matrix domain was reduced, the bubble nucleated in the disperse domain can expand, coalesce each other and result in larger cells structures that do not resemble the self-assembled template.

As suggested from the physical foaming process, a stable self-assembled block copolymer template is required to create highly ordered nanocellular foams. To achieve this, we incorporated the UV-induced chemical foaming process with self-assembled poly(methyl methacrylate-*b*-tert-butyl acrylate) (PMMA-*b*-PtBA). As shown in

Figure 3.1(a), the process involves two major steps: (1) formation of a self-assembled block copolymer template consisting of the foamable PtBA domain and the PMMA matrix domain, and (2) control of the gas generation and expansion within the foamable domain (PtBA domain). In the first step, PMMA-*b*-PtBA was mixed with a small amount of photoacid generators and cast on a substrate, where the self-assembly was induced through solvent evaporation. In the second step, acids are created from the PAG upon UV irradiation. Upon heating, these acids will diffuse and catalyze the tert-butyl ester deprotection of PtBA creating isobutene gas (Figure 3.1(b)).^{15,16} By controlling the foaming temperature between the glass transition temperatures (T_g) of the PtBA (39 °C) and PMMA (125 °C), the gas generation and expansion could be controlled within the rubbery PtBA domains, while the glassy PMMA domains suppress cell expansion and cell coalescence. Due to the stability of the self-assembled template during the foaming process, highly-ordered nanocellular structures could be produced.

In this chapter, PMMA-*b*-PtBA with cylindrical self-assembled morphologies were prepared by solvent casting from CHCl₃. The self-assembled morphology was confirmed by small-angle X-ray scattering (SAXS) and transmission electron microscopy (TEM). The foaming condition was determined by analyzing the T_g of PtBA and PMMA, as well as the gas generation behavior observed by thermogravimetric analysis (TGA). The development of the nanocellular structure from the self-assembled PtBA cylindrical domains was then observed by scanning electron microscopy (SEM) at various foaming times at 80 °C. The formation of the cell structures was then confirmed by comparing the cell structure observed by SEM, and changes in density and chemical structure of the samples before and after foaming. In the latter part of this chapter, the effects of process parameters, such as PAG concentration, foaming temperature, and UV-penetration on the cell structure of the resulting foams were investigated for providing insight on how the process could be further optimized or scaled up.

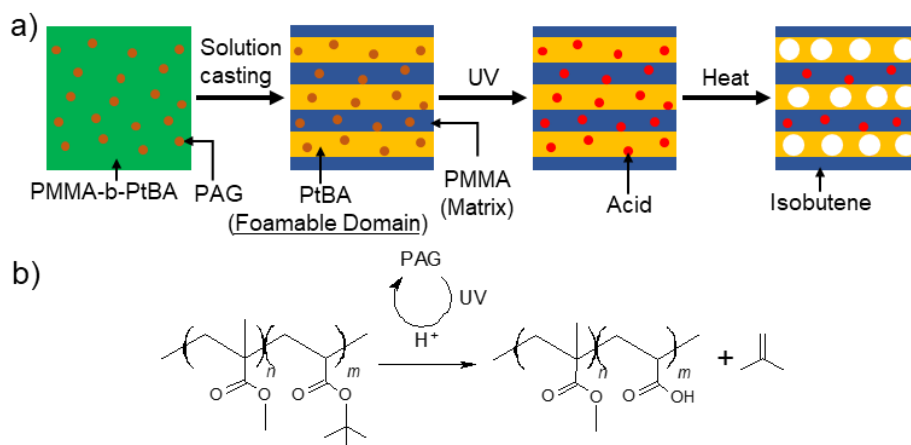


Figure 3.1 (a) Process flow for the UV-induced chemical foaming of self-assembled block copolymer, and (b) acid-catalyzed tert-butyl ester deprotection reaction. Reprinted with permission from Rattanakawin et al., *ACS Macro Lett.*, **2020**, 9 (10), 1433-1438. DOI: 10.1021/acsmacrolett.0c00475. Copyright ©2020. American Chemical Society.

3.2 Methods

3.2.1 Sample preparation

An asymmetric diblock copolymer, PMMA-*b*-PtBA, was purchased from Polymer Source Inc. (Canada). The number-average molecular weight (M_n) of the PMMA and PtBA blocks were 41,000 and 18,000, respectively, and the polydispersity index was 1.2. The volume fraction of the PtBA block was estimated at 31%. The photoacid generator (PAG), BBI-109, was purchased from Midori Kagaku Co., Ltd. (Japan). This photoacid generator was selected since it had a maximum absorption wavelength of 238 nm, close to that of the UV lamp, 254 nm. All purchased reagents were used as received without further purification.

PMMA-*b*-PtBA films were prepared by solution casting. The polymer solution was prepared by dissolving PMMA-*b*-PtBA (1.0 wt%) and PAG (0.05 wt%, 5 wt% polymers) in 20 ml chloroform. The polymer solution was then cast on a 50 ml glass vial and left under ambient conditions to slowly evaporate for several days. During this slow evaporation, microphase separation was induced homogeneously throughout the solution. The resulting sample was a transparent film with a thickness of approximately 150 μm . To ensure complete solvent removal, the film was further dried in a vacuum for 24 hours. The polymer film was removed from the glass vial by submerging the in liquid nitrogen and then dried in a vacuum for 24 hours before the foaming experiments. Polymer films with PAG concentrations of 0.025 and 0.10 wt% were similarly prepared to investigate the effect of the PAG concentration on the cell structure.

3.2.2 Foaming of the self-assembled PMMA-*b*-PtBA film

Prior to foaming, the self-assembled PMMA-*b*-PtBA films were exposed to UV light to generate the acids from PAG. The UV irradiation was conducted with a UV lamp (UVGL-58, UVP, U.K.), with an irradiation intensity of 1 mW/cm^2 and a dosage of 3600 mJ/cm^2 . Immediately after the UV irradiation, the PMMA-*b*-PtBA films were foamed by heating on a hot plate to allow the acids to diffuse and create isobutene gas from the tert-butyl ester deprotection of PtBA.

3.2.3 Characterization of the self-assembled morphology

The self-assembled morphology of the PMMA-*b*-PtBA film was analyzed using small-angle x-ray scattering (SAXS) (NANO-Viewer, Rigaku Corp., Japan). The SAXS profiles of the as-cast PMMA-*b*-PtBA films, where the scattering intensity (I) was plotted against the scattering vector (q), were obtained by irradiation with Cu K- α ($\lambda=0.15418$ nm) for 3 hours. From the SAXS profile, the pitch of the self-assembly (l_0) could be obtained by Equation (3.1), where q^* is the scattering vector of the primary peak of the scattering profile. The long-range ordering of the self-assembly could be determined by a series of the higher-order peak position (q/q^*). The hexagonally packed cylindrical domains show q/q^* of 1, $\sqrt{3}$, 2, $\sqrt{7}$, while the lamellar shows q/q^* of 1, 2, 3, 4.^{17,18}

$$l_0 = \frac{2\pi}{q^*} \quad (3.1)$$

A bright-field TEM (H7650, Hitachi High Tech Corp. Japan) with its acceleration voltage of 100kV was used to observe the self-assembled morphology. Before the TEM measurements, a thin specimen of the PMMA-b-PtBA films was prepared by an ultramicrotome (ULTRACUT E, Reichert Jung, USA) and placed on a TEM grid. To compare the self-assembled morphology observed from the TEM image to the one observed at the SAXS results, a two-dimensional Fast-Fourier transform (2D-FFT) analysis of the TEM image was conducted using ImageJ (National Institutes of Health, U.S.A.) and Matlab (Mathworks, USA). A 1D-FFT profile could be produced by radial averaging of the 2D-FFT image, and the pitch of the self-assembly could be obtained using Equation (3.1).

3.2.4 Thermal property measurement for determining a foaming condition

To determine the appropriate foaming temperature, the glass transition temperature (T_g) of PMMA-b-PtBA was measured by the differential scanning calorimetry (DSC) (DSC7020, Hitachi Ltd., Japan). The measurements were conducted between 0-160 °C with a heating and cooling rate of 10 °C/min as illustrated in Figure 3.2. The first heating was conducted to remove the thermal history from the polymer, and the T_g was determined from the second heating curve.

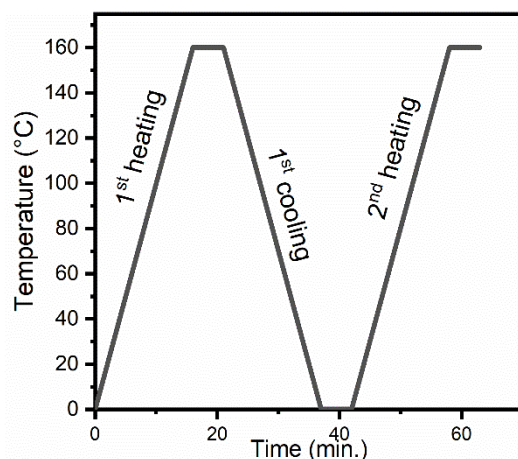


Figure 3.2 Temperature profile for the DSC measurement with heating and cooling rate were 10 °C/min.

The foaming temperature and time were selected based on the tert-butyl ester deprotection determined by thermogravimetric analysis (TGA) (DTG-60H, Shimadzu Corp., Japan). To ensure the generated isobutene gas can easily diffuse out of the polymer films, thin films of the samples were prepared by casting 200µl of a polymer solution, containing PtBA-b-PMMA (5 wt%) and PAG (0.025 wt%) in chloroform, on a 4 cm² silicon wafer. The solvent was allowed to evaporate for 12 hours in ambient conditions, followed by 12 hours of vacuum drying to ensure complete solvent removal. Before the measurement, UV-irradiation at 254 nm with 3600 mJ/cm² dosage was conducted to generate the acids. Dynamic thermogravimetry at the 10 °C/min heating rate was conducted from 40 to 120°C to evaluate the suitable foaming temperature, while isothermal thermogravimetry was conducted to determine the foaming time.

3.2.5 Characterization of the cell structure

The cell structure of the foamed PMMA-b-PtBA samples was observed using SEM (SU8000, Hitachi High Technologies Corp., Japan) with 10 kV. Prior to the observation, the foamed samples were sliced by the microtome and placed on a silicon wafer, and ~1 nm in thickness of platinum was deposited on the surface to avoid the charging effect.

Figure 3.3 shows two SEM images. A region was selected for analysis as shown in Figure 3.3 (b). The cell structure was determined from the SEM images by using ImageJ, where the cell size of an individual cell (d_i) and the number of cells (n) are determined within a specific area (A). The average cell size (d) and cell density (N) were determined and averaged from 3 SEM images using Equations (3.2) and (3.3), respectively.¹⁹

$$d = \frac{\sum d_i}{n} \quad (3.2)$$

$$N = \left(\frac{n}{A}\right)^{\frac{3}{2}} \quad (3.3)$$

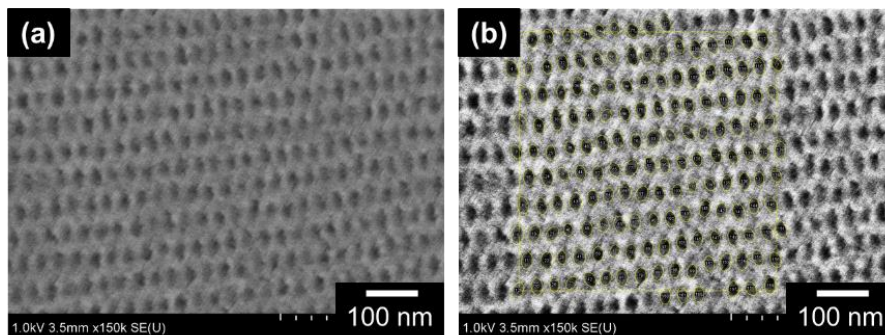


Figure 3.3 Cell structure analysis by ImageJ: (a) original SEM image and (b) overlay of the analyzed SEM image

3.2.6 Change of the chemical structure before and after foaming

The chemical structure change of the PMMA-b-PtBA films after foaming was observed by an attenuated total reflection Fourier-transformed infrared spectroscopy (FTIR) (Spectrum 1000, PerkinElmer Inc., U.S.A.). Each FTIR spectrum was acquired with a co-added scan of 20 times in the range from 100 to 7500 cm^{-1} with 4 cm^{-1} resolutions.

3.2.7 Evaluation of the density of the polymer foam

The density of the non-foamed (ρ_p) and foamed polymer (ρ_f) were measured by a pycnometer (AccuPyc II 1340, Micrometrics Inc., U.S.A.) with a sample cell volume of 1 cm^3 . It should be noted that the density measurement by pycnometer is only suitable for closed-cell foams since the specimen's open-cell volume is excluded from the measurement.

3.2.8 Rheological properties measurement

The rheological properties of PMMA-b-PtBA were measured using a rheometer (ARES, TA Instrument, U.S.A). PMMA-b-PtBA bulk sample with 40 mm × 10 mm × 0.3 mm in dimension was prepared by compression molding at 170 °C under ~20-30 MPa mechanical pressure. The complex viscosity (η^*) was measured in torsion mode at the strain of 0.3 % and the frequency of 0.63 rad/s.

3.2.9 UV penetration depth measurement

For UV penetration measurements, PMMA-b-PtBA films approximately 450 μm in thickness were prepared by casting PMMA-b-PtBA (2.0 wt%) and PAG (0.10 wt%, 5 wt% polymers) in 20 ml chloroform. The sample was irradiated by the UV light with an irradiation intensity of 1 mW/cm² and a dosage of 3600 mJ/cm² and foamed at 80 °C for 5 minutes. The foamed sample was then cryofractured in liquid N₂ and the cross-section was observed by SEM. The UV-penetration depth was then estimated as the minimal distance between the location of the SEM image where a foamed and non-foamed interface was observed and the UV-irradiation surface. The effect of the cell expansion on the UV-penetration depth was then corrected using the expansion ratio obtained from the pycnometer.

3.3 Results and Discussion

3.3.1 Self-assembly of PMMA-b-PtBA by solution casting

The SAXS profile of the self-assembled morphology of PMMA-b-PtBA prepared by solution casting is shown in Figure 3.4. From the scattering vector of the primary peak $q^* = 0.192 \text{ nm}^{-1}$, the minimum pitch of the self-assembly was 33 nm. The ratio of the subsequent peak positions to q^* were 2.0 and 2.7 ($\sim\sqrt{7}$). It indicated the formation of hexagonally packed cylindrical domains, which theoretically have the scattering peaks at $q/q^* = 1: \sqrt{3}: 2: \sqrt{7}$.^{17,18} It should be noted that the missing peak at $q/q^* = \sqrt{3}$ and the weak peak at $q/q^* = 2$ could be the result of the domain factors.^{17,18}

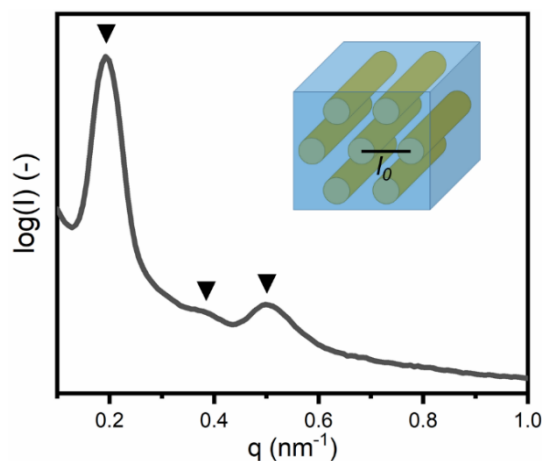


Figure 3.4 SAXS profile of as-cast PMMA-b-PtBA films. The black triangles indicate the scattering peaks at $q/q^* = 1, 2$ and $\sqrt{7}$, where the first peak (q^*) is 0.190 nm^{-1} . The insert shows a schematic of hexagonally packed cylinders. Reprinted with permission from Rattanakawin et al., *ACS Macro Lett.*, **2020**, *9* (10), 1433-1438. DOI: 10.1021/acsmacrolett.0c00475. Copyright ©2020. American Chemical Society.

Figure 3.5(a) shows the TEM image of the self-assembled PMMA-b-PtBA sample, where the brighter and the darker regions respectively correspond to the PtBA-rich and PMMA-rich domains. Long-range ordering of striped and hexagonally packed PtBA domains was observed, confirming the formation of the hexagonally packed cylindrical self-assembled morphology. To determine the pitch of the self-assembly, 2D-FFT and 1D-FFT analyses were conducted using the TEM images and the results were shown in Figure 3.5(b) and Figure 3.5(c). From the 1D-FFT profile, the primary peak location was found at $q^* = 0.196 \text{ nm}^{-1}$, which corresponds to a pitch of 32 nm. This is a good agreement with the value obtained from the SAXS analysis. From both the SAXS and TEM results, the formation of hexagonally packed cylindrical domains was confirmed.

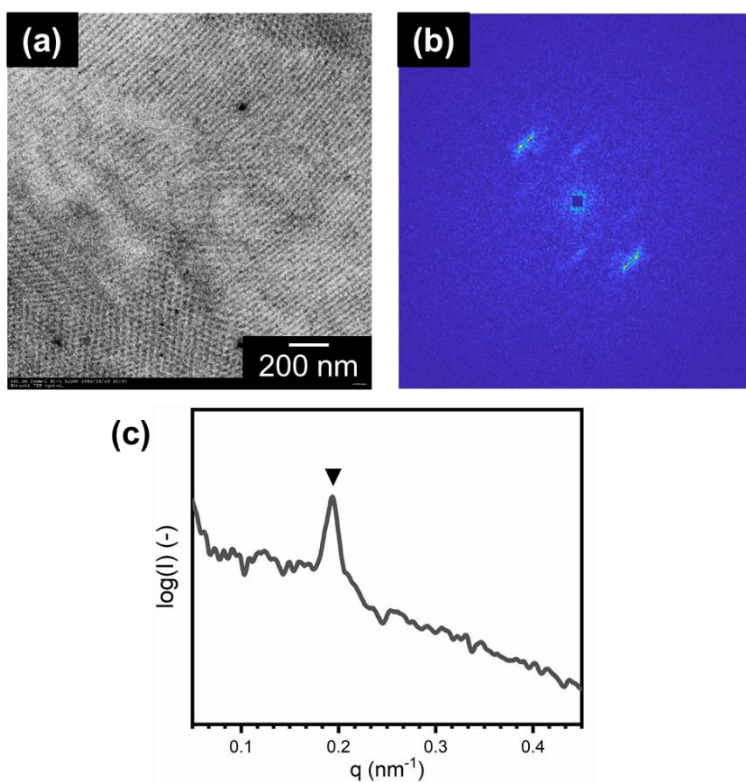


Figure 3.5 Characterization of the self-assembled PMMA-b-PtBA morphology by TEM: (a) TEM image, (b) 2D-FFT image, and (c) 1D-FFT profile. The darker and brighter domains in the TEM corresponds to the PtBA and PMMA rich domains, respectively. The 1D-FFT profile (c) was obtained by radial averaging the 2D-FFT profile (b), and the black triangle in (c) indicates the peak where $q^* = 0.196 \text{ nm}^{-1}$. Reprinted with permission from Rattanakawin et al., *ACS Macro Lett.*, **2020**, 9 (10), 1433-1438. DOI: 10.1021/acsmacrolett.0c00475. Copyright ©2020. American Chemical Society.

3.3.2 Suitable foaming conditions

The foaming condition is crucial to creating highly-ordered nanocellular foams. A suitable foaming temperature and time should be determined to allow sufficient gas generation and cell growth in the PtBA domains while maintaining a stable PMMA matrix to control the cell structure and ordering.

Figure 3.6 shows the 2nd DSC heating curve of PMMA-b-PtBA. The DSC measurement was conducted in the temperature range from 0 to 160 °C at 10 °C/min heating and cooling rates. Two inflection points were observed at 39 and 125 °C, which correspond to the T_g of PtBA and PMMA, respectively. As a reference temperature condition, the foaming temperature was selected to be 80 °C, between the T_g of both polymers, expecting to foam the PtBA selectively. At this foaming temperature, the PtBA domains are in a rubbery state, which is suitable for acid diffusion, gas generation, and cell expansion. On the other hand, the PMMA domains will remain in a glassy state enabling good cell structure control and preventing cell coalescence.

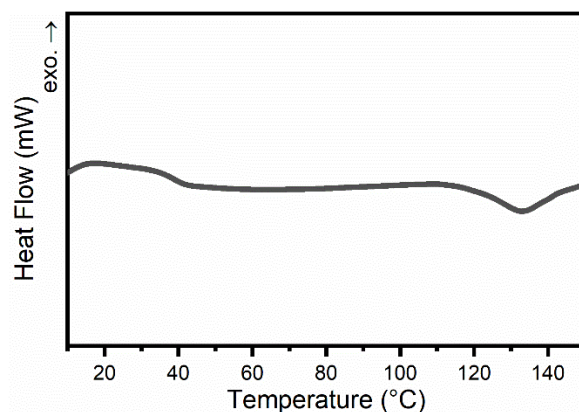


Figure 3.6 DSC 2nd heating curve of PMMA-b-PtBA without PAG. Reprinted with permission from Rattanakawin et al., *ACS Macro Lett.*, **2020**, 9 (10), 1433-1438. DOI: 10.1021/acsmacrolett.0c00475. Copyright ©2020. American Chemical Society.

Figure 3.7 shows the TGA thermographs of PMMA-b-PtBA films with 5wt% PAG. The measurement was conducted after 3600 mJ/cm² UV-irradiation. This UV irradiation dosage was selected to ensure the complete activation of the photoacid generators. Dynamic TGA measurements, where the weight loss was plotted with increasing heating temperature between 40 to 120 °C at a constant heating rate of 10 °C/min (Figure 3.7(a)). Approximately 1.5 % weight loss was observed at 80 °C. This indicates gas generation occurred at this foaming temperature. Isothermal TGA measurements where the weight loss was plotted against the heating time at 80 °C were conducted to determine the appropriate foaming time (Figure 3.7(b)). From the measurement, most of the weight loss was observed within 10 minutes of the heating at 80 °C, resulting in approximately 7 % weight loss. In contrast, only 2 % weight loss was observed between 10 to 60 minutes of the heating. This suggests that the majority of the gas generation occurred within 10 minutes. From the DSC and TGA results, the foaming temperature of 80 °C and foaming time of 0-10 minutes were selected.

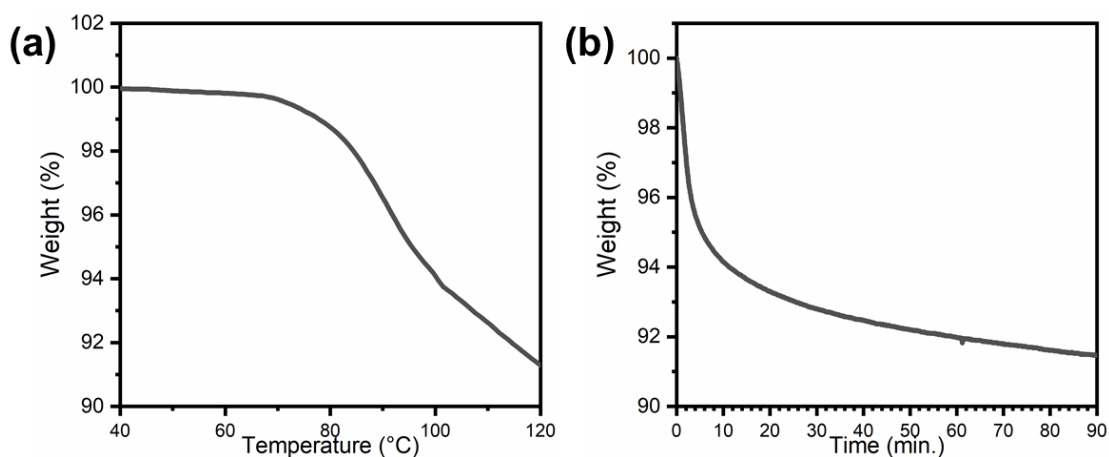


Figure 3.7 TGA thermograph of PMMA-b-PtBA films after 3600 mJ/cm² UV-irradiation: (a) dynamic thermogravimetry from 40 to 120 °C, and (b) isothermal thermogravimetry at 80 °C. Reprinted with permission from Rattanakawin et al., *ACS Macro Lett.*, **2020**, 9 (10), 1433-1438. DOI: 10.1021/acsmacrolett.0c00475. Copyright ©2020. American Chemical Society.

3.3.3 Formation of the PMMA-b-PtBA nanocellular foams

The formation of PMMA-b-PtBA nanocellular foams was studied by irradiating the films with UV light at 254 nm and dosage of 3600 mJ/cm², followed by heating at 80 °C for 0, 1, 5, and 10 minutes. Optical microscope images of PMMA-b-PtBA films after the solvent casting and foaming at 80 °C for 10 minutes are shown in Figures 3.8(a) and (b), respectively. Interestingly, the PMMA-b-PtBA film remained transparent after foaming which indicates that the cell size is much smaller than the wavelength of visible light (400-700 nm).

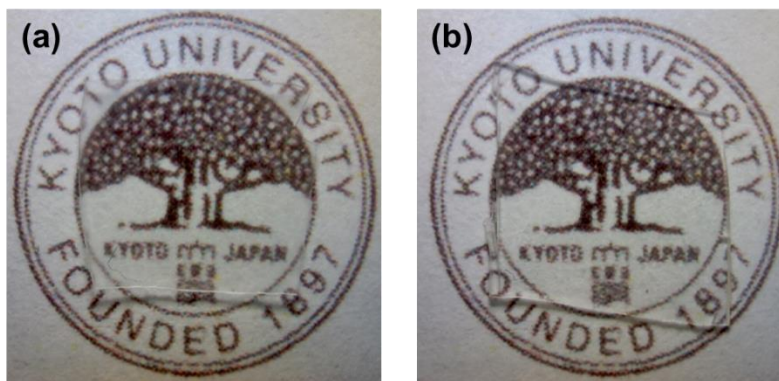


Figure 3.8 Optical microscope images of PMMA-b-PtBA films: (a) as-cast and (b) foamed at 80 °C for 10 minutes. (The size of the films is 7 × 7 × 0.15 mm.) Reprinted with permission from Rattanakawin et al., *ACS Macro Lett.*, **2020**, 9 (10), 1433-1438. DOI: 10.1021/acsmacrolett.0c00475. Copyright ©2020. American Chemical Society.

SEM observations were conducted to investigate the change in cell structure against heating time at a foaming temperature of 80 °C. Figure 3.9 shows the SEM images of non-foamed PMMA-b-PtBA film and those foamed at 80 °C for different foaming times. The cell size and cell densities of those films are summarized in Figure 3.10. Before the foaming, stripe patterns of the self-assembled domains were observed from the SEM image illustrated in Figure 3.9(a). The observed pitch of self-assembly was 35 nm, which was close to those estimated from the SAXS and TEM measurements. After foaming at 80 °C for 1 minute, highly ordered nano-sized pores with cell size and density of 18.1 nm and 7.82×10^{15} cells/cm³ were produced along the self-assembled domains, as shown in Figure 3.9(b). It is speculated that the formation of the spherical cells from the cylindrical self-assembled morphology is due to the limited amount of gas generation in the PtBA domains and the presence of the rigid PMMA matrix domains. Increasing the foaming time to 5 minutes, the cell density significantly increased to 1.42×10^{16} cells/cm³ as shown in Figure 3.9(c). A slight decrease in cell size to 17 nm was observed. However, the cell structure became more homogeneous. This is most likely due to the increase of the isobutene (gas) generation and diffusivity in the PtBA domains. Only a minor change in the cell structure was observed at the samples foamed at 80 °C for 10 minutes, where the cell size and density were 16.1 nm and 1.53×10^{15} cells/cm³. This is the result of the decrease in gas generation with longer foaming times as previously observed from the TGA measurements (Figure 3.7(b)).

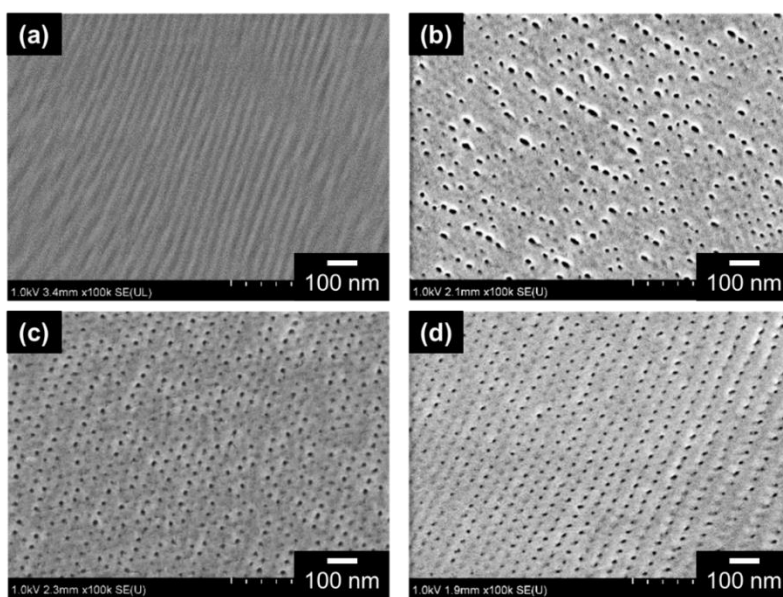


Figure 3.9 SEM images of PMMA-b-PtBA films foamed at 80 °C for (a) 0, (b) 1, (c) 5 and (d) 10 minutes. Reprinted with permission from Rattanakawin et al., *ACS Macro Lett.*, **2020**, 9 (10), 1433-1438. DOI: 10.1021/acsmacrolett.0c00475. Copyright ©2020. American Chemical Society.

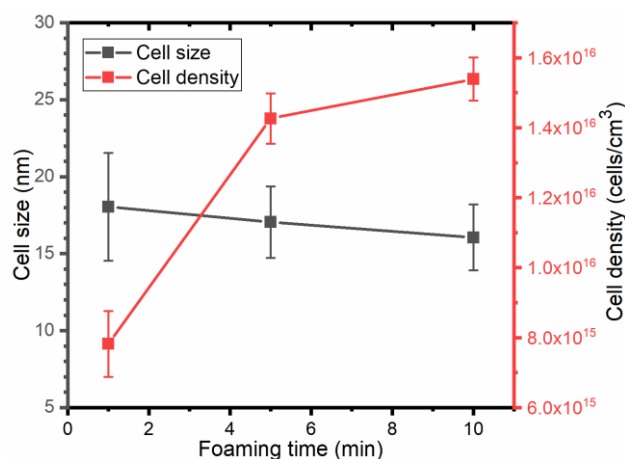


Figure 3.10 Effects of the foaming time at 80 °C on cell size (grey) and cell density (red). Reprinted with permission from Rattanakawin et al., *ACS Macro Lett.*, **2020**, 9 (10), 1433-1438. DOI: 10.1021/acsmacrolett.0c00475. Copyright ©2020. American Chemical Society.

To confirm the formation of the pores, the density of the PMMA-b-PtBA films foamed at 80 °C were measured by a gas pycnometer. The results were illustrated in Figure 3.11. The density of the as-cast PMMA-b-PtBA film was 1.25 g/cm³. The density gradually decreased by foaming, for example, the density of the samples foamed at 80°C for 10 minutes was 1.20 g/cm³ reducing 0.05 g/cm³. This corresponds to an expansion of 1.04 from the bulk PMMA-b-PtBA. This expansion is relatively low when compared to the physical foaming methods, which could achieve an expansion of 2.5 with similar cell size.²⁰ However it should be noted that for our method, only the PtBA domain which consists of 30% of the total domains were expanded. Furthermore, the expansion was constricted by the PMMA domains. A higher expansion could be achieved by changing the ratio of the PtBA block or foaming conditions and will be discussed in Chapter 4.

Using the cell size and the cell density from the SEM observations and the density of the non-foamed polymer (ρ_p), the density of the foam (ρ_f) was evaluated. This was done by determining the specific volume of the gas phase (V_g) and the expansion ratio (Φ) using Equations (3.4) and (3.5).²¹ From Figure 3.11, the density estimated from the SEM shows good agreement with the results of pycnometry, giving the density of 1.21 g/cm³ for the sample foamed at 80 °C for 10 minutes.

$$V_g = N \times \frac{\pi}{6} \times d^3 \quad (3.4)$$

$$\Phi = 1 + V_g = \frac{\rho_p}{\rho_f} \quad (3.5)$$

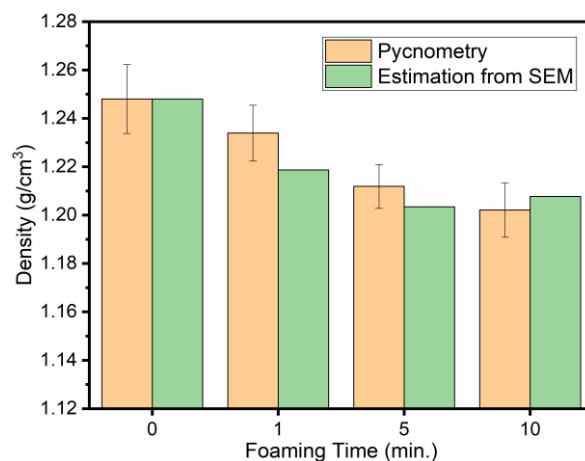


Figure 3.11 Density of PMMA-b-PtBA films foamed at 80 °C for 1-10 minutes. The orange bar and green bars respectively represent the density obtained from pycnometry and one estimated from the SEM observations. Reprinted with permission from Rattanakawin et al., *ACS Macro Lett.*, **2020**, 9 (10), 1433-1438. DOI: 10.1021/acsmacrolett.0c00475. Copyright ©2020. American Chemical Society.

To ensure that the cells were formed from the tert-butyl ester deprotection reaction, the change in a chemical structure during the foaming process was measured by FTIR spectroscopy. Figure 3.12 shows a result of FTIR spectrums of the PMMA-b-PtBA films foamed at 80 °C for different foaming times. In particular, the absorption peaks at approximately 1390 and 1366 cm^{-1} was studied since it corresponds to the CH_3 bond in the tert-butyl group of PtBA.²² From Figure 3.12(b), it can be observed that the peaks decreased with the increase of the foaming time, which indicates that the tert-butyl ester protection reaction progresses and isobutene gas generates. Interestingly, only a small decrease in the absorption peak was observed between 5 to 10 minutes of foaming. This suggests that most of the foaming reaction occurred within 5 minutes of foaming time, which is consistent with the SEM results in Figure 3.10 where the cell density almost reaches the peak value at the 5 minutes of heating time. As the rate of isobutene production decreases, the gas concentration in the PtBA domains decreases, and fewer cells are formed.

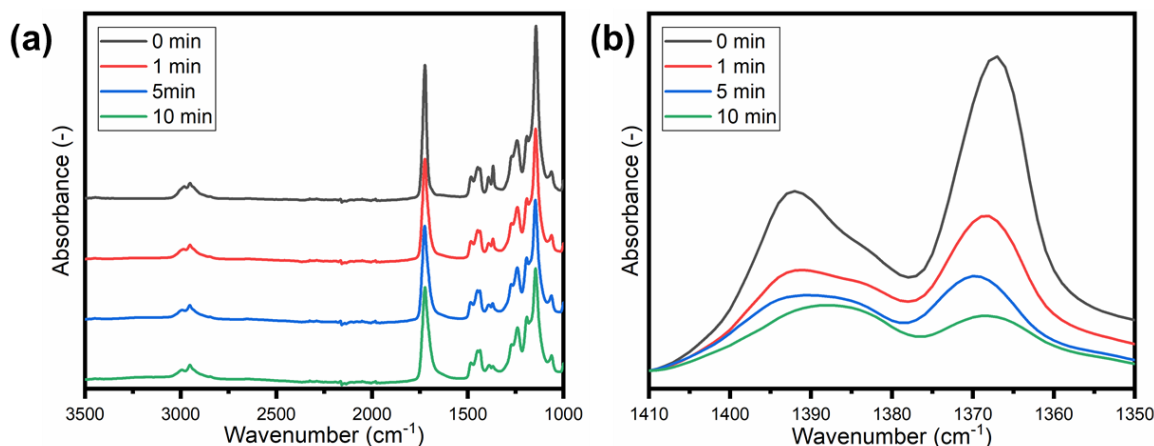


Figure 3.12 FTIR spectrums of the PMMA-b-PtBA films foamed at 80 °C for 0-10 minutes: (a) full FTIR spectra between 1000 – 3500 cm⁻¹ and (b) FTIR spectra of CH₃ bond of the tert-butyl ester group in PtBA. Reprinted with permission from Rattanakawin et al., *ACS Macro Lett.*, **2020**, 9 (10), 1433-1438. DOI: 10.1021/acsmacrolett.0c00475. Copyright ©2020. American Chemical Society.

3.2.4 Effect of PAG concentration on the cell structure

To investigate the effect of the PAG concentration on the cell structure, PMMA-b-PtBA films with three different PAG concentrations, i.e., 2.5, 5, and 10 wt% to polymer were prepared. The UV irradiation and the foaming were performed in the same way as described in the previous section, where the foaming was conducted at 80 °C for 5 minutes. The SEM images of the foamed PMMA-b-PtBA films are shown in Figure 3.13, and the cell size and the cell density of the foamed films are summarized in Figure 3.14. It can be observed that the cell density is highly dependent on the PAG concentration. It increases from 9.05×10^{15} to 1.83×10^{16} cells/cm³ with the increase of PAG from 2.5 to 10 wt%. However, no clear correlation between the cell size and PAG concentration was observed, where the cell size was in a range from 17.0 to 19.9 nm. This is because, with higher PAG concentrations, more acids are created during the UV irradiation process. Because of this, more isobutene is generated and leads to a higher cell density. However, due to the limited amount of generated isobutene in the PtBA domains and the presence of the PMMA domains neighboring the PtBA domains, the cells produced in PtBA domains could not be fully expanded and no significant change in cell size was observed.

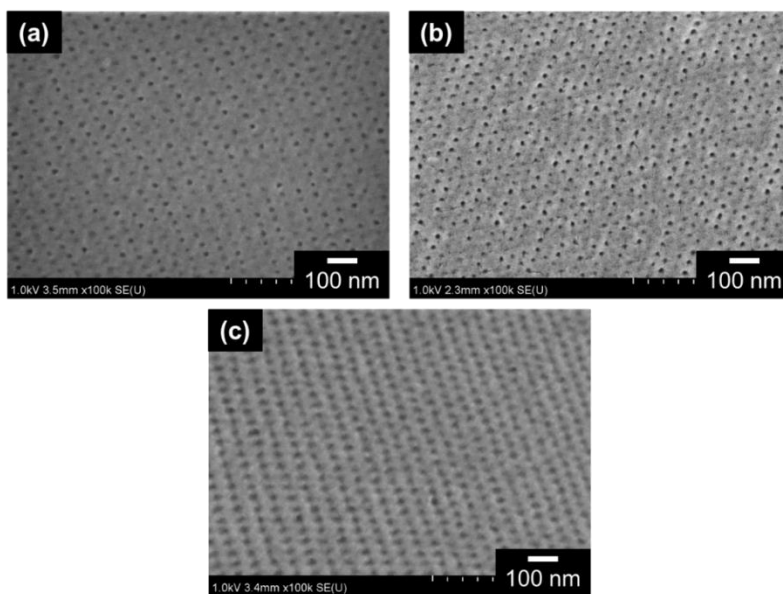


Figure 3.13 SEM images of PMMA-b-PtBA films with PAG concentration of (a) 2.5, (b) 5 and (c) 10 wt% polymer, foamed at 80 °C for 5 minutes. Reprinted with permission from Rattanakawin et al., *ACS Macro Lett.*, **2020**, *9* (10), 1433-1438. DOI: 10.1021/acsmacrolett.0c00475. Copyright ©2020. American Chemical Society.

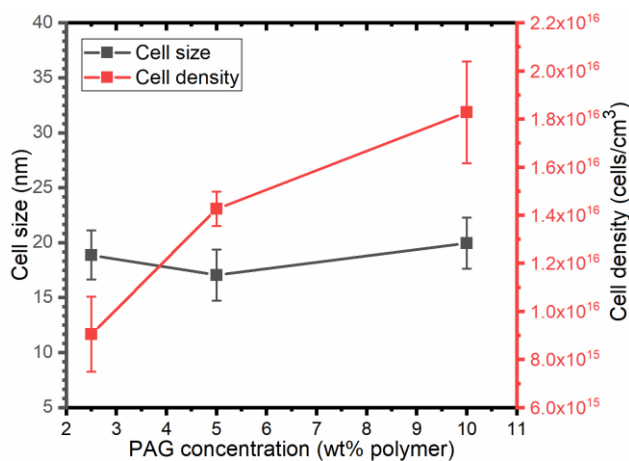


Figure 3.14 Effects of the PAG concentration on the cell size (grey) and cell density (red) of PMMA-b-PtBA foamed at 80 °C for 5 minutes. The cell size and densities were obtained by analyzing the SEM images shown in Figure 3.13.

3.2.5 Effect of foaming temperature on the cell structure

Figure 3.15 illustrates the cell structure obtained by foaming the self-assembled PMMA-b-PtBA films at 70-120 °C for 5 minutes. At 70 °C, stripe-like patterns representing the self-assembled cylindrical domains were observed as shown in Figure 3.15(a), similarly to the as-cast SEM image shown in Figure 3.9(a). This indicates that the foaming at 70 °C for 5 minutes was insufficient to accelerate acid diffusion within the PtBA domains and it could not generate

a sufficient amount of isobutene for creating cells. Indeed, the dynamic TGA measurement showed almost no weight loss at 70 °C (Figure 3.7(a)). From 80-120 °C, highly ordered spherical cells were formed as shown in Figure 3.15(b-f). The cell size and the densities were estimated from the SEM images in Figure 3.15. The results of the cell size and the density of the films foamed at different foaming temperatures are summarized in Figure 3.16. A noticeable change in the cell structure occurred when the foaming temperature was increased from 80 to 90 °C, where the cell size and density increased from 17.0 to 25.0 nm and 1.42×10^{16} to 1.71×10^{16} cells/cm³, respectively. At the higher foaming temperatures, higher than 90°C, no significant change in the cell size was observed, while the cell density showed a gradual trend of increase from 1.71×10^{16} to 1.88×10^{16} cells/cm³. Interestingly, despite the cell expansion, only spherical cells were formed from the cylindrical PtBA domains, suggesting that insufficient isobutene gas was generated to fully expand the cells throughout the PtBA-rich domain.

The relationship between the cell structure and the foaming temperature could be explained by the isobutene gas generation rate and the viscoelasticity of the PMMA matrix. At 80 °C, the gas is gradually generated as shown in the isothermal TGA of Figure 3.16 and the gas nucleated the cells in the PtBA domains. However, due to the high rigidity of the PMMA matrix that exists in the vicinity of the PtBA domains, the nucleated cells could not be expanded to be the size larger than the thickness of PtBA domains. The increase in cell size to 25 nm for PMMA-b-PtBA foamed at 90 °C is most likely due to the reduction of the rigidity of the PMMA domains. Figure 3.17 shows the complex viscosity of bulk PMMA-b-PtBA film measured in a temperature scan mode. It can be found that the complex viscosity was decreased from 6.4×10^8 to 5.2×10^8 Pa·s by increasing temperature from 80 to 90 °C. In the temperature range from 100 to 120 °C, while the complex viscosity of PMMA-b-PtBA continuously decreased, there was no significant change in the cell size as shown in Figure 3.16. It can be speculated that, at high foaming temperatures, the isobutene gas could be instantaneously generated within a short time frame (Figure 3.18), where most of the tert-butyl ester group is deprotected by the time that the temperature inside the polymer film is equilibrated. Because of this, most of the gas generated would diffuse out from the film before the PMMA-rich domains were softened, resulting in the formation of a stable cell structure. This is demonstrated in Figure 3.19, where no change in the cell size was observed for PMMA-b-PtBA samples foamed at 110 and 120 °C for 1, 2, and 5 minutes.

Figure 3.20 shows an optical microscope image of PMMA-b-PtBA foamed at 130 °C for 5 minutes, where microcellular foams were formed. When the foaming was conducted above the glass transition temperature of PMMA, the matrix domain softens and allows the cells to expand in the micrometer range. Indeed, the viscosity of the polymer decreases drastically to 4.5×10^7 Pa·s at 130°C when compared to 1.6×10^8 Pa·s at 120°C. Thus, maintaining a stable PMMA matrix domain is required to limit the cell expansion to the nanometer scale.

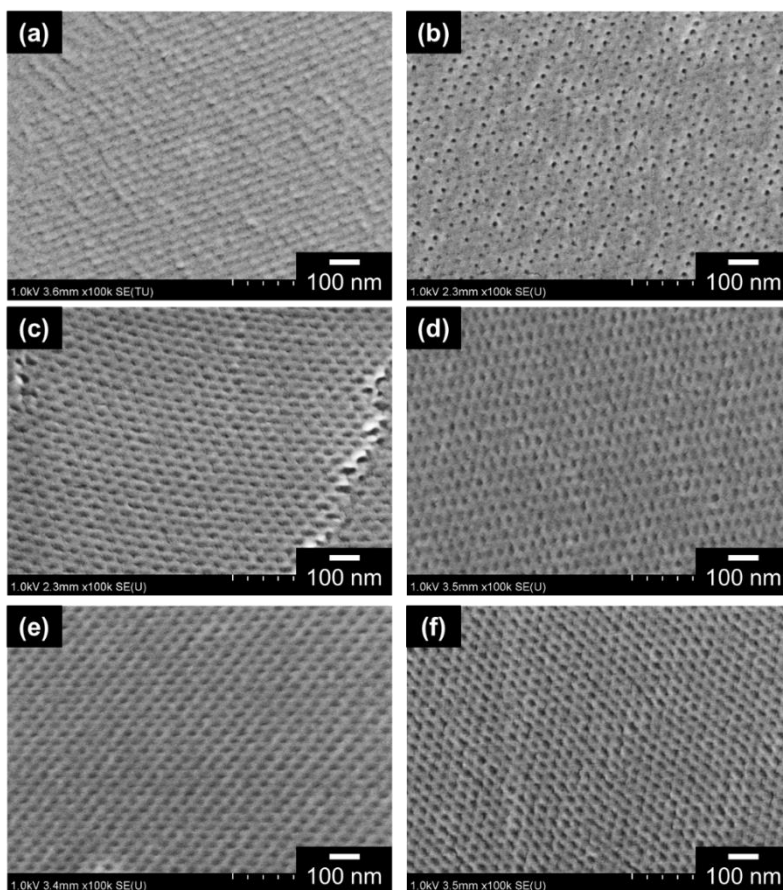


Figure 3.15 SEM images of PMMA-b-PtBA films foamed at (a) 70, (b) 80, (c) 90, (d) 100, (e) 110 and (f) 120 °C for 5 minutes. Reprinted with permission from Rattanakawin et al., *ACS Macro Lett.*, **2020**, 9 (10), 1433-1438. DOI: 10.1021/acsmacrolett.0c00475. Copyright ©2020. American Chemical Society.

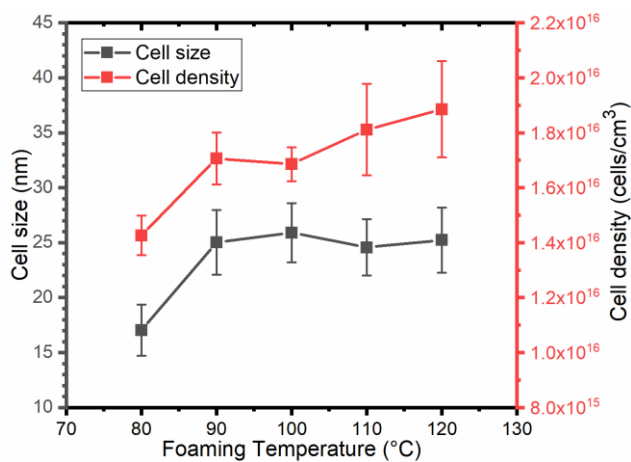


Figure 3.16 Effects of the foaming temperature on the cell size (grey) and cell density (red) of PMMA-b-PtBA foamed at a temperature in the range of 80-120 °C for 5 minutes.

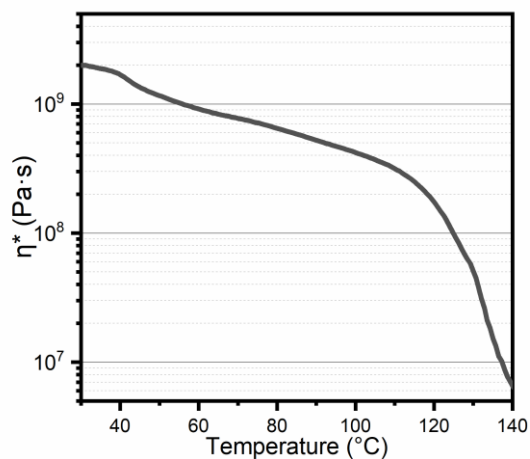


Figure 3.17 Temperature scan of the complex viscosity (η^*) of PMMA-b-PtBA without PAG. (Torsion-mode experiments with strain of 0.3 % at frequency of 0.63 rad/s). Reprinted with permission from Rattanakawin et al., *ACS Macro Lett.*, **2020**, 9 (10), 1433-1438. DOI: 10.1021/acsmacrolett.0c00475. Copyright ©2020. American Chemical Society.

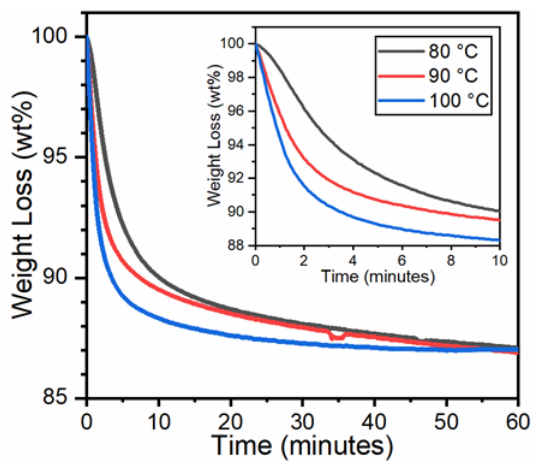


Figure 3.18 Isothermal TGA thermographs of PMMA-b-PtBA at 80-100°C for 60 minutes. (The insert shows the decomposition behavior of PMMA-b-PtBA at shorter heating time.)

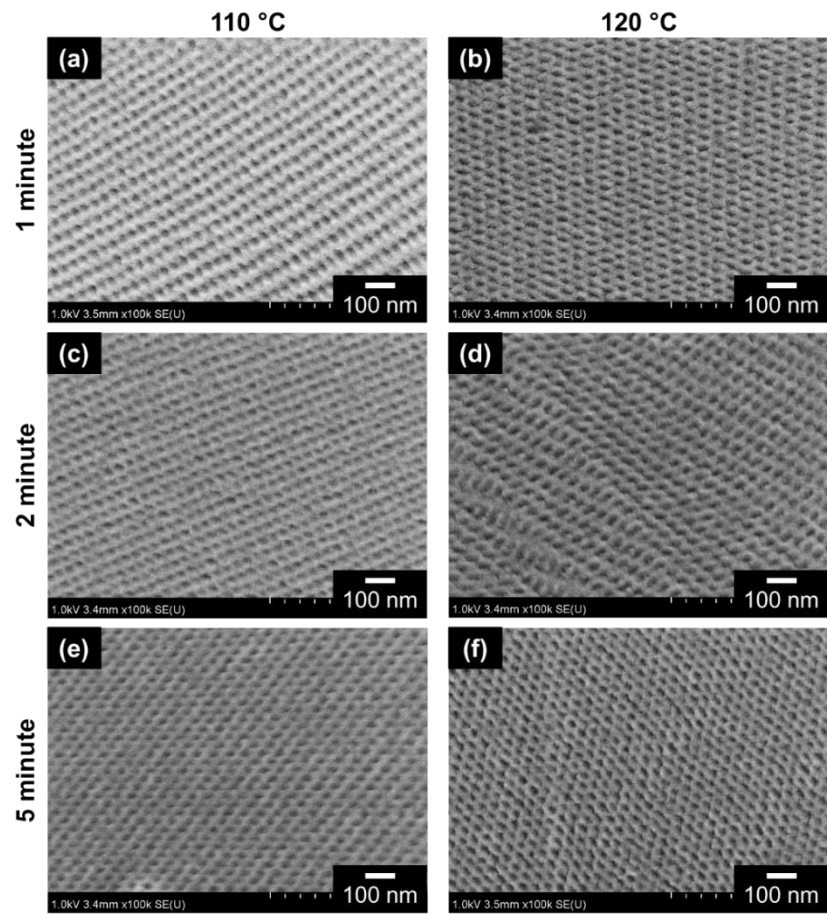


Figure 3.19 SEM images of PMMA-b-PtBA films foamed at (a,c,e) 110, and (b,d,f) 120 °C for (a,b) 1, (c,d) 2 and (e,f) 5 minutes.

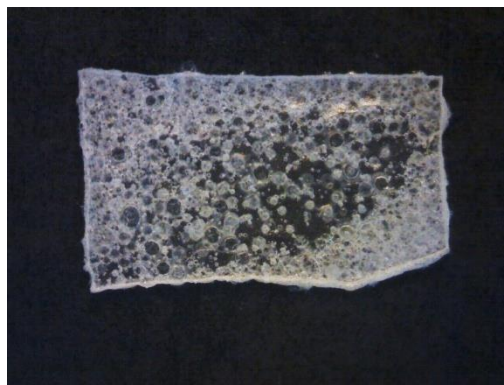


Figure 3.20 Optical microscope images of PMMA-b-PtBA foamed at 130 °C for 5 minutes. (The size of the films is $5 \times 8 \times 0.15$ mm.)

3.2.5 Estimation of the UV penetration depth

The UV penetration depth is an important process parameter for scaling up the UV-induced chemical foaming process since it limits the maximum thickness of the polymer foam. In this study, we evaluated the cross-section SEM of PMMA-b-PtBA films with a thickness of 450 μm foamed at 80 $^{\circ}\text{C}$ for 5 minutes. The UV penetration depth is defined as the distance between the UV irradiation surface to the foam/non-foamed interface as shown in Figure 3.21. The cross-section SEM of the as-cast PMMA-b-PtBA film is shown in Figure 3.22, where no cellular structure is observed throughout the film. Figure 3.23 shows the cell structure at different locations for the PMMA-b-PtBA film after UV-irradiation with an irradiation intensity of 1 mW/cm^2 and a dosage of 3600 mJ/cm^2 and foamed at 80 $^{\circ}\text{C}$ for 5 minutes. The SEM images, which were taken near the UV-irradiation surface, at the middle of the foamed layer, and the interface between the foam/non-foamed layer, are shown in Figure 3.23(b-d), where the ordered nanocellular structure could be observed. At a location near the UV-irradiation surface, relatively smaller cells were created compared to cells observed at the middle of the foamed layer. Most likely this is due to isobutene diffusing out of the film. With sufficient PAG activation and less gas diffusion through the surface, as shown in Figure 3.23(c), the majority of the film shows a cell structure. At the interface of the foamed/non-foamed regions, it is expected that only a small amount of PAG was activated. As a result, smaller cells were produced. Considering the facts that the interface appears around 345 μm in depth from the UV-irradiated surface and the expansion ratio at 80 $^{\circ}\text{C}$ for 5 minutes was 1.03, the UV-penetration depth for this experimental setup is approximately 330 μm . By conducting the UV-irradiation on both sides of the film, the maximum thickness of the PMMA-b-PtBA foam by UV-induced chemical foaming is 660 μm . This thickness may be improved by using longer wavelength UV or visible light irradiation with the suitable PAG or using thermally liable functional groups instead of the UV process, and will be further discussed in Chapter 5.

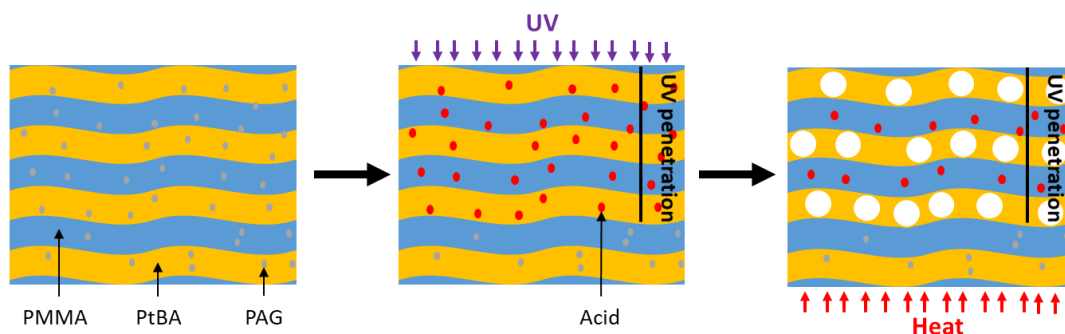


Figure 3.21 Schematic image of the UV penetration depth evaluation based on the foamed/non-foamed interface

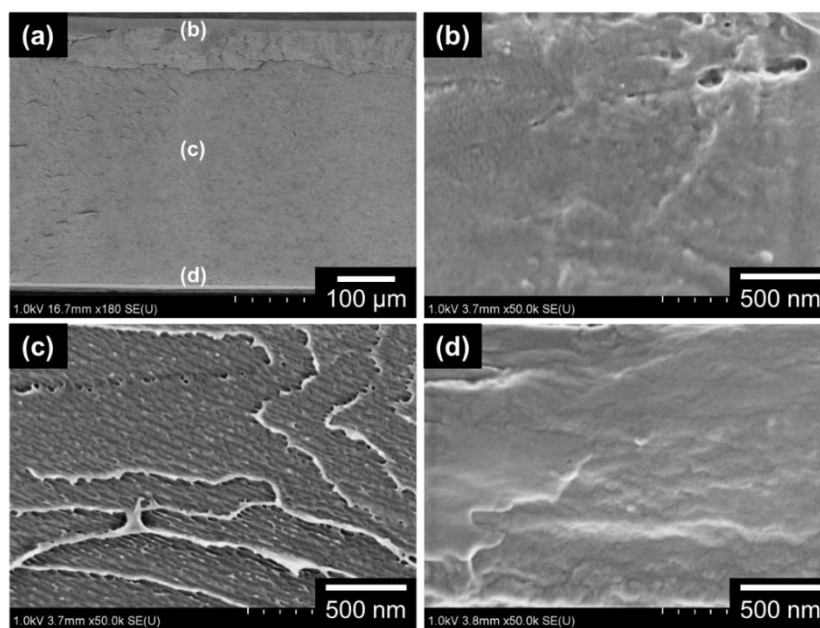


Figure 3.22 Cross-section SEM images of as-cast PMMA-b-PtBA film with thickness of 450 μm : (a) low magnification and (b-d) high magnification. (a): the observation location of the higher magnification SEM images, (b): top, (c): center and (d): bottom of the film.

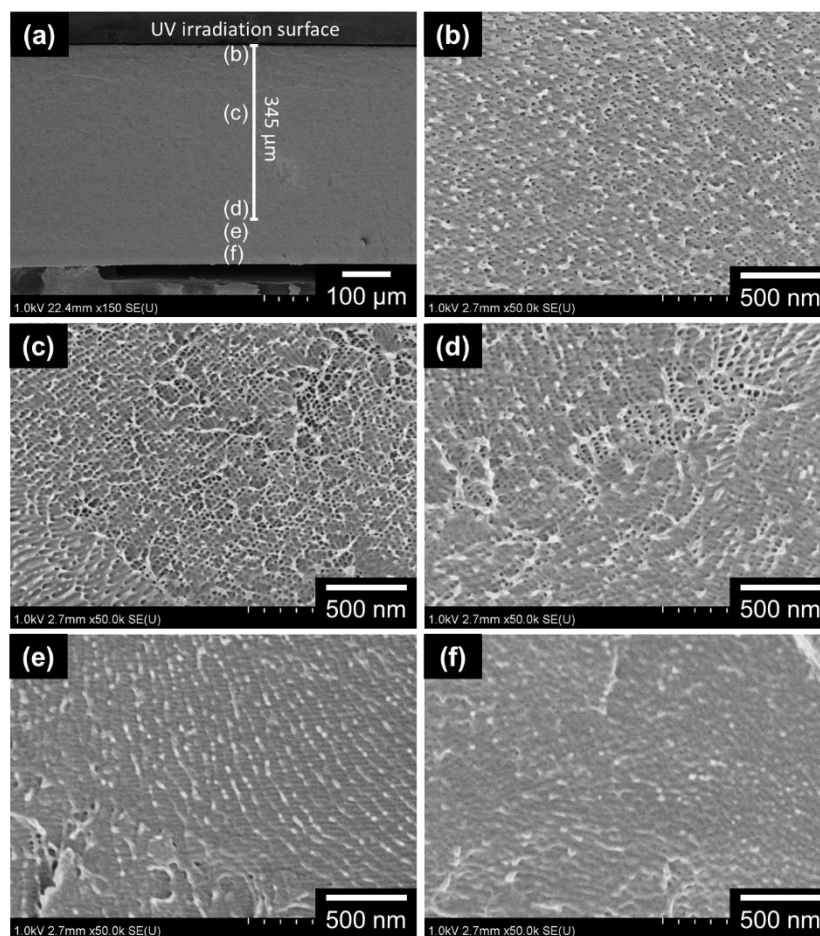


Figure 3.23 Cross-section SEM images of PMMA-*b*-PtBA film with a thickness of 450 μm foamed at 80°C for 5 minutes: (a) low magnification and (b-f) high magnification. (a): the observation location of the higher magnification SEM images, (b): UV-irradiation surface, (c): middle of the foamed layer and (d): foamed/non-foamed interface, (e) non-foamed layer and (e) bottom of the film.

3.4 Conclusion

In this chapter, we have proposed a chemical foaming method to produce highly-ordered nanocellular foams, which uses self-assembled block copolymer templates consisting of foamable PtBA-rich cylindrical domain and a PMMA-rich matrix domain. This approach includes two major steps, 1) prefabricating the self-assembled template including a small amount of the PAG molecules, and 2) exposing the sample with UV light before the heating. By carefully setting the heating temperature between T_g of the foamable PtBA-rich domain and that of the matrix, isobutene is generated and expands the PtBA-rich domains while the glassy PMMA domains control the cell expansion in the nanometer scale. As a result, highly ordered nanocellular foams with cell size and density of $\sim 16\text{--}25$ nm and

$\sim 0.8\text{--}1.9 \times 10^{16}$ cells/cm³ were created. Notably, the nanocellular foams were transparent, since the cell size is significantly smaller than the wavelength of visible light.

The development of the cell structure was observed by changing the foaming time at 80 °C. In the initial stage of the foaming, nanocellular foams were sparsely created along with the self-assembled domain. As the foaming time increases, the cell density increases, while the cell size slightly decreases but becomes more uniform as a result of the isobutene gas diffusing within the PtBA domains. Within 10 minutes of foaming, no further change in the cell structure was observed as a result of the majority of the isobutene gas being generated.

The effect of the process parameters, including the PAG concentration, and foaming temperature on the cell structure of the nanocellular foam was also investigated. It was found that the PAG concentration mainly affects the cell density of the foam. By increasing the PAG concentration, the amount of the generated photo acids are increased, increasing cell nucleation sites and isobutene gas generation. The effect of the foaming temperature on the cell structure is relatively complex. As the foaming temperature increases in the range of 80-90 °C, the generation of isobutene gas increases, and the softening PMMA domain progressed. As a result, the cells are gradually formed and expanded, and both cell size and cell density are increased. However, above 100 °C, the isobutene gas is rapidly generated and diffused out while the PMMA domain is not fully softened. Then, the cell structure is stabilized within a short time frame and the cell expansion is limited. Due to the limited amount of gas generated from cylindrical PtBA domains, the self-assembled morphology with a higher PtBA ratio is necessary to create nanocellular foams with higher degrees of expansion, which is discussed in Chapter 4.

3.5 References

- (1) Feng, X.; Kawabata, K.; Kaufman, G.; Elimelech, M.; Osuji, C. O. Highly Selective Vertically Aligned Nanopores in Sustainably Derived Polymer Membranes by Molecular Templating. *ACS Nano* **2017**, *11* (4), 3911–3921. <https://doi.org/10.1021/acsnano.7b00304>.
- (2) Feng, X.; Tousley, M. E.; Cowan, M. G.; Wiesenauer, B. R.; Nejati, S.; Choo, Y.; Noble, R. D.; Elimelech, M.; Gin, D. L.; Osuji, C. O. Scalable Fabrication of Polymer Membranes with Vertically Aligned 1 Nm Pores by Magnetic Field Directed Self-Assembly. *ACS Nano* **2014**, *8* (12), 11977–11986. <https://doi.org/10.1021/nn505037b>.
- (3) Feng, X.; Nejati, S.; Cowan, M. G.; Tousley, M. E.; Wiesenauer, B. R.; Noble, R. D.; Elimelech, M.; Gin, D. L.; Osuji, C. O. Thin Polymer Films with Continuous Vertically Aligned 1 Nm Pores Fabricated by Soft Confinement. *ACS Nano* **2019**, *10* (1), 150–158. <https://doi.org/10.1021/acsnano.5b06130>.
- (4) Liu, M.; Wu, J.; Gan, Y.; Chen, C. Q. The Pore-Load Modulus of Ordered Nanoporous Materials with Surface Effects. *AIP Adv.* **2016**, *6* (3), 035324. <https://doi.org/10.1063/1.4945441>.
- (5) Yokoyama, H.; Li, L.; Nemoto, T.; Sugiyama, K. Tunable Nanocellular Polymeric Monoliths Using Fluorinated Block Copolymer Templates and Supercritical Carbon Dioxide. *Adv. Mater.* **2004**, *16* (17), 1542–1546. <https://doi.org/10.1002/adma.200400072>.

- (6) Yokoyama, H.; Li, L.; Dutriez, C.; Iwakura, Y.; Sugiyama, K.; Masunaga, H.; Sasaki, S.; Okuda, H. Horizontally and Vertically Aligned Polymeric Nanosheets: CO₂-Induced Morphological Changes of Block Copolymer Thin Films. *Macromolecules* **2008**, *41* (22), 8626–8631. <https://doi.org/10.1021/MA801487A>.
- (7) Shinkai, T.; Sugiyama, K.; Ito, K.; Yokoyama, H. Nanoporous Fabrication of Block Copolymers via Carbon Dioxide Swelling: Difference between CO₂-Swollen and Nanoporous Block Copolymers. *Polymer (Guildf)*. **2016**, *100*, 19–27. <https://doi.org/10.1016/j.polymer.2016.08.011>.
- (8) Li, L.; Nemoto, T.; Sugiyama, K.; Yokoyama, H. CO₂ Foaming in Thin Films of Block Copolymer Containing Fluorinated Blocks. *Macromolecules* **2006**, *39* (14), 4746–4755. <https://doi.org/10.1021/ma060325l>.
- (9) Yokoyama, H.; Sugiyama, K. Nanocellular Structures in Block Copolymers with CO₂-Philic Blocks Using CO₂ as a Blowing Agent: Crossover from Micro-to Nanocellular Structures with Depressurization Temperature. *Macromolecules* **2005**, *38* (25), 10516–10522. <https://doi.org/10.1021/ma051757j>.
- (10) Ruiz, J. A. R.; Cloutet, E.; Dumon, M. Investigation of the Nanocellular Foaming of Polystyrene in Supercritical CO₂ by Adding a CO₂-Philic Perfluorinated Block Copolymer. *J. Appl. Polym. Sci.* **2012**, *126* (1), 38–45. <https://doi.org/10.1002/APP.36455>.
- (11) Xu, Y.; Liu, T.; Yuan, W.-K.; Zhao, L. Influence of Microphase Morphology and Long-Range Ordering on Foaming Behavior of PE-*b*-PEO Diblock Copolymers. *Ind. Eng. Chem. Res.* **2015**, *54* (28), 7113–7121. <https://doi.org/10.1021/acs.iecr.5b01014>.
- (12) Zhang, W.; Chen, B.; Zhao, H.; Yu, P.; Fu, D.; Wen, J.; Peng, X. Processing and Characterization of Supercritical CO₂ Batch Foamed Poly(Lactic Acid)/Poly(Ethylene Glycol) Scaffold for Tissue Engineering Application. *J. Appl. Polym. Sci.* **2013**, *130* (5), 3066–3073. <https://doi.org/10.1002/APP.39523>.
- (13) Taki, K.; Nitta, K.; Kihara, S.-I.; Ohshima, M. CO₂ Foaming of Poly(Ethylene Glycol)/Polystyrene Blends: Relationship of the Blend Morphology, CO₂ Mass Transfer, and Cellular Structure. *J. Appl. Polym. Sci.* **2005**, *97* (5), 1899–1906. <https://doi.org/10.1002/APP.21930>.
- (14) Yokoyama, H. Small Angle X-Ray Scattering Studies of Nanocellular and Nanoporous Structures. *Polym. J.* **2013**, *45* (1), 3–9. <https://doi.org/10.1038/pj.2012.205>.
- (15) Kojima, J.; Takada, T.; Jinno, F. Thin Microcellular Plastic Sheet Incorporating Designed Foaming Patterns Made by Photochemical Foaming Technology. *J. Cell. Plast.* **2007**, *43* (2), 103–109. <https://doi.org/10.1177/0021955X06076573>.
- (16) Rattanakawin, P.; Yamamura, K.; Yoshimoto, K.; Ohshima, M. Development and Optimization of UV-Induced Chemical Foaming Process. *J. Photopolym. Sci. Technol.* **2019**, *32* (5), 693–698. <https://doi.org/10.2494/photopolymer.32.693>.
- (17) Hamley, I.; Castelletto, V. Small-Angle Scattering of Block Copolymers. In *Soft Matter Characterization*; Springer Netherlands, 2008; pp 1021–1081. https://doi.org/10.1007/978-1-4020-4465-6_20.
- (18) Förster, S.; Timmann, A.; Konrad, M.; Schellbach, C.; Meyer, A.; Funari, S. S.; Mulvaney, P.; Knott, R. Scattering Curves of Ordered Mesoscopic Materials. *J. Phys. Chem. B* **2005**, *109* (4), 1347–1360.

<https://doi.org/10.1021/jp0467494>.

- (19) Wang, L.; Hikima, Y.; Ohshima, M.; Yusa, A.; Yamamoto, S.; Goto, H. Development of a Simplified Foam Injection Molding Technique and Its Application to the Production of High Void Fraction Polypropylene Foams. **2017**. <https://doi.org/10.1021/acs.iecr.7b03382>.
- (20) Martín-de León, J.; Van Loock, F.; Bernardo, V.; Fleck, N. A.; Rodríguez-Pérez, M. Á. The Influence of Cell Size on the Mechanical Properties of Nanocellular PMMA. *Polymer (Guildf)*. **2019**, *181*. <https://doi.org/10.1016/j.polymer.2019.121805>.
- (21) Baldwin, D. F.; Park, C. B.; Suh, N. P. Microcellular Sheet Extrusion System Process Design Models for Shaping and Cell Growth Control. *Polym. Eng. Sci.* **1998**, *38* (4), 674–688. <https://doi.org/10.1002/pen.10232>.
- (22) Gratzl, G.; Paulik, C.; Hild, S.; Guggenbichler, J. P.; Lackner, M. Antimicrobial Activity of Poly(Acrylic Acid) Block Copolymers. *Mater. Sci. Eng. C* **2014**, *38* (1), 94–100. <https://doi.org/10.1016/j.msec.2014.01.050>.

Chapter 4 Effects of Self-Assembled Block Copolymer Morphology on Nanocellular Foams Prepared by UV-induced Chemical Foaming

4.1 Introduction

In Chapter 3, a process to produce highly-ordered nanocellular foams using self-assembled PMMA-b-PtBA morphology as a template for UV-induced chemical foaming was proposed. The process mainly involves two steps: (1) creation of a self-assembled morphology to be used as a template, which consists of a gas-producing PtBA-rich domain and PMMA-rich domain, (2) control of the gas generation and expansion within the PtBA domain. Using this process, we have demonstrated the preparation of highly-ordered nanometer-scale size spherical cells from a self-assembled PMMA-b-PtBA morphology with hexagonally packed cylindrical PtBA domains, and the effect of the processing parameters on the cell formation was extensively investigated. In this chapter, we focus on the effect of morphological geometry and elucidate how different cellular structures could be prepared from several types of self-assembled morphologies of PMMA-b-PtBA block copolymer.

Self-assembly of block copolymer has been widely studied in nanomanufacturing applications, such as the photolithography processes for semiconductor manufacturing,¹⁻⁵ a framework for mesoporous material fabrication.⁶⁻¹⁰ To this extent, the self-assembled morphology of block copolymers has been extensively studied from both theoretical and experimental perspectives. In regards to the block copolymer specification, the self-assembled morphology is dependent on the volume fraction (f_A) and segregation strength (χN) between the two blocks, where χ and N denote the Flory-Huggins interactive parameter and the degree of polymerization, respectively.¹¹⁻¹³ By adjusting the f_A of one block, self-assembled spheres, cylinders, gyroids, and lamella morphologies could be produced. Whether or not these self-assembled morphologies are formed is mainly determined by the segregation strength (χN). The segregation strength of the block copolymers could be improved by using highly dissimilar block copolymer to increase χ , or increasing the degree of polymerization (N). Theoretically, microphase separation can occur when χN exceeds a critical value for the order-disorder transition ($\chi N_{ODT} = 10.5$).¹¹⁻¹³ However, annealing conditions such as solvent and thermal fluctuation effects may influence this order-disorder transition. Apart from the self-assembled morphology, the pitch of the self-assembly is also determined by the molecular weight of the block copolymers, and is commonly represented by a power-law relationship, i.e., $l_0 \propto M_n^{2/3}$.¹⁴⁻¹⁶ For self-assembled morphologies prepared by solvent casting, the morphology could be also largely affected by the casting process. This includes the selectivity of the solvent to one block,¹⁷⁻¹⁹ and the solvent evaporation rate,^{20,21} which may affect the effective volume fraction (f_A), Flory-Huggins parameter (χ), morphology, and long-range ordering of the self-assembly.

The objective of this chapter is to elucidate the influence of the PMMA-b-PtBA self-assembled morphology on the formation of nanocellular foams produced by UV-induced chemical foaming. For this study, the self-assembled morphology is mainly controlled by the block copolymer specification, and the solvent casting was conducted with relatively neutral solvent and casting time. The chapter consists of two parts. In the first part, nanocellular foams were prepared from self-assembled cylindrical and lamella morphology, where PtBA domains show either cylindrical or

lamella morphologies and short-ranged ordered PMMA domains. Solvent casting PMMA-b-PtBA was conducted to prepare the self-assembled morphology from the block polymers with different PtBA weight fractions (ϕ_{PtBA}), which directly relates to the volume fraction of the PtBA block (f_{PtBA}). Nanocellular foams were then created from the resulting self-assembled PMMA-b-PtBA morphologies, and the resulting cell structures were analyzed in relation to the amount of gas generated in the PtBA domains and the stability (rigidity or viscoelasticity) of the PMMA domains. In the latter part, the self-assembled lamella morphology was prepared using different PMMA-b-PtBA molecular weights (M_n) of block copolymers. The changes in the cell size and cell expansion through the different M_n were then investigated and explained in relation to the increasing pitch of the self-assembly (l_0) and the viscosity of the PMMA-rich matrix domain (η_0). The effects of the foaming process parameters discussed in this chapter are expected to provide an insight for controllability of the cell size, shape, expansion ratio, and the order of the cell structure of the nanocellular foams prepared from UV-induced chemical foaming of self-assembled block copolymer templates.

4.2 Methods

4.2.1 Materials

The specifications of the PMMA-b-PtBA block copolymer used in this study are summarized in Table 4-1. The samples of PMMA-b-PtBA are prepared and these are categorized into two groups: (Group 1): three kinds of the samples with different PtBA weight fractions (ϕ_{PtBA}) (Samples 1-3), and (Group 2): four kinds of the samples with different molecular weights (M_n) (Samples 4-7). The PMMA-b-PtBA block copolymers of Samples 1-3 were purchased from Polymer Source Inc. (Canada) and used as received, while The PMMA-b-PtBA block copolymer of Samples 4-7 were synthesized in house by TERP polymerization as described in Chapter 2. An iodonium salt photoacid generator (PAG), BBI-109 (Midori Kagaku, Japan), with a maximum absorption wavelength of 238 nm was used as received.

Table 4.1 Specification of PtBA-b-PMMA with different molecular weights and PtBA weight fraction (ϕ_{PtBA}).

Sample ^[a]	M_n	ϕ_{PtBA} (wt%)	D	$T_{g,\text{PtBA}}$ (°C) ^[b]	$T_{g,\text{PMMA}}$ (°C) ^[b]	Casting Conditions
1	59,000	30.5	1.20	39	125	CHCl ₃ , room temp. for 5 days
2	56,500	52.2	1.20	39	123	THF, 40 °C for 10 days
3	57,000	66.7	1.20	40	127	THF, 40 °C for 10 days
4	25,500	58.9	1.28	45	108	CHCl ₃ , 40 °C for 7 days
5	73,800	56.6	1.32	43	116	CHCl ₃ , 40 °C for 7 days
6	117,300	55.1	1.29	43	117	CHCl ₃ , 40 °C for 7 days
7	233,200	56.6	1.34	43	118	CHCl ₃ , 40 °C for 7 days

^[a] Samples 1-3 were purchased from Polymer Source, whereas Samples 4-7 were synthesized by TERP emulsion polymerization (detailed synthesis procedures shown in Chapter 2).

^[b] T_g of PMMA-b-PtBA was measured by DSC thermography (a detailed procedure shown in Chapter 2 and 3)

4.2.2 Foaming of the self-assembled PMMA-b-PtBA film

Self-assembled block copolymer thin films were prepared by solution casting 20 g of a polymer solution of 0.20 g of PMMA-b-PtBA and 0.01 g of PAG onto a 50-ml glass vial. Table 4.1 summarizes the used solvents and the casting conditions to form the polymer film. The solvents were either removed under ambient conditions (Sample 1) or by heating at 40 °C (Sample 2-4). For the samples cast at 40 °C, the solvent evaporation rate was slowed down by loosely covering the glass vial. After the solvent removal, the resulting film was further dried in a vacuum for 24 hours to ensure no solvents remained in the film. The polymer film was removed from the glass vial by submerging the in liquid nitrogen and then dried for 24 hours in a vacuum drier.

The UV-induced chemical foaming was conducted using the prepared films in the same procedure described in Chapter 3: the films were first irradiated with UV light at a wavelength of 254 nm, irradiation intensity of 1 mW/cm², and dosage of 3600 mJ/cm² to completely generate the acids from PAG. After the UV irradiation, the PMMA-b-PtBA films were foamed by heating on a hot plate at 80-100 °C for 5 minutes.

4.2.3 Characterization of the self-assembled morphology

The self-assembled PMMA-b-PtBA morphology was observed using a bright-field TEM (H7650, Hitachi High Tech Corp. Japan) with an acceleration voltage of 200kV. The TEM samples were prepared by an ultramicrotome (Ultracut E, Reichert-Jung Inc., USA), where thin ~80 nm PMMA-b-PtBA films were sliced and placed on a TEM grid. The ratio of the dark PtBA-rich domains and the bright PMMA-rich domains were analyzed from the TEM images using ImageJ software (National Institutes of Health, U.S.A.). An 800 × 800 nm area in the middle of the TEM image was cropped and binarized by the automatic threshold function in ImageJ. Figure 4.1 (a) shows a TEM image and (b) shows a binarized TEM image. The ratio between the black and white pixels was used to estimate the fraction of the PtBA domains.

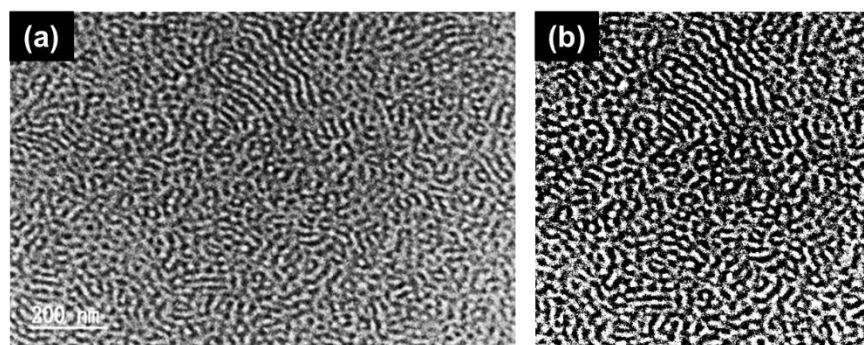


Figure 4.1 Evaluation of the observed PtBA-rich domain fraction: (a) original TEM image and (b) cropped and binarized TEM image used for the analysis.

The self-assembled morphology of the PMMA-b-PtBA film was also analyzed using a small angle x-ray scattering (SAXS) (NanoViewer, Rigaku Corp., Japan). The incident X-ray beams (Cu K- α , $\lambda=0.15418$ nm) were irradiated through the as-cast PMMA-b-PtBA samples for 6 hours and the scattering profiles were obtained by radially averaging the 2D scattering image. The pitch of the self-assembly was estimated from the primary Bragg peak (q^*) and the higher-order peak positions (q/q^*) as described in Chapter 3.

4.2.4 Characterization of the cell structure

The cell structure of the PMMA-b-PtBA nanocellular foams was observed by SEM (SU8000, Hitachi High Technologies Corp., Japan) with 10 kV. The SEM specimen was prepared by a microtome and placed on a silicon wafer. 1 nm thick platinum was deposited on the surface of the specimen before the SEM observation. In this chapter, two types of nanocellular foams were obtained, spherical shape cells and tubes shape cells. For spherical structure, the cell size was calculated using the method described in Chapter 3. In the case of nanocellular tubes, the structure was represented by the average width of the tubes, which was obtained by using ImageJ as shown in Figure 4.2.

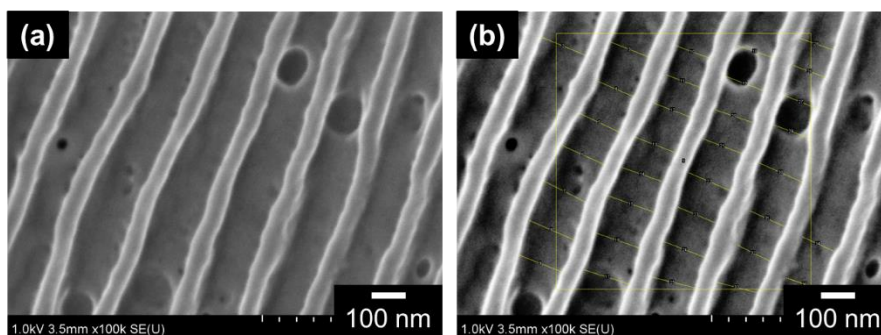


Figure 4.2 Analysis of the cell structure of nanocellular PMMA-b-PtBA tubes: (a) original SEM image and (b) overlay of the analyzed SEM image

4.2.5 Isobutene gas generation

Isothermal TGA measurements at 100 °C were used to estimate the amounts of isobutene gas generated from the different PMMA-b-PtBA self-assembled morphologies. The thin films of PMMA-b-PtBA were prepared by the same procedure described in Chapter 3. Before the TGA measurements, UV irradiation was conducted at a dosage of 3600 mJ/cm² to create the acids from the PAG.

4.2.6 Density and expansion ratio evaluation

The density (ρ) of the as-cast and the foamed PMMA-b-PtBA films were determined by a floatation method.²² The density of the sample was compared to that of a liquid mixture made from ethanol, water, and glycerol, with the density ranging from 0.789 – 1.26 g/cm³. The sample density was estimated by the density of the liquid solution in

which the sample was suspended, as shown in Figure 4.3. The density measurements were only conducted for nanocellular foams because the density of the microcellular foams was too low to be measured by the density of pure ethanol. The expansion ratio of the foamed films was then calculated using Equation 3.5, as a ratio between the density of the non-foamed polymer to the density of the foam.

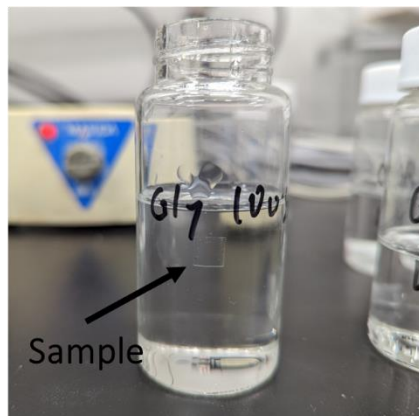


Figure 4.3 Estimation of the sample density by a flotation method.

4.3 Results and Discussion

4.3.1 Effect of the self-assembled morphology on the cell structure

PMMA-*b*-PtBA films with different self-assembled morphologies were prepared by casting the solution of samples 1-3, which have PtBA the weight fractions (ϕ_{PtBA}) of 31, 52, and 67 wt%, respectively. The self-assembled morphologies were observed by TEM and the obtained images were shown in Figure 4.4. The TEM images of PMMA-*b*-PtBA with $\phi_{\text{PtBA}} = 31$ wt% show a stripe pattern with the hexagonally packed darker dots as shown in Figure 4.4(a). Because the darker domains of the binarized image occupy approximately 38% of the total area as shown in Figure 4.4(a), the domains most likely represent the PtBA-rich domains. Figure 4.5 shows a SAXS profile for $\phi_{\text{PtBA}} = 31$ wt% and exhibits the first-order Bragg peaks at the scattering vector (q^*) of 0.19 nm^{-1} , which indicates that the pitch (l_0) of self-assembly is 33 nm. The subsequent peaks were observed at the scattering vectors of 0.38 nm^{-1} ($q/q^* = 2$) and 0.50 nm^{-1} ($q/q^* = 2.63$). These peaks correspond to the hexagonally-packed cylindrical morphologies with theoretical $q/q^* = 1: \sqrt{3}: 2: \sqrt{7}$.^{23,24} The missing peaks at $q/q^* = \sqrt{3}$ and $q/q^* = 2$ are most likely the result of the domain form-factor.^{23,24} For $\phi_{\text{PtBA}} = 52$ wt%, a long-ranged ordered stripe pattern was observed from the TEM image shown in Figure 4.4(b), while the SAXS profile shows the peaks at $q/q^* = 1: 2: 3$ with q^* of 0.219 nm^{-1} as shown in Figure 4.5, which indicates that the lamella self-assembled morphology with $l_0 = 29 \text{ nm}$ was formed. The weak SAXS peak at $q/q^* = 2$, suggests that the thickness of the PtBA and that of the PMMA lamella domains are almost equal.^{15,25} In the case of $\phi_{\text{PtBA}} = 67$ wt%, the short-ranged ordered phase-separated domains are observed from the TEM image shown in Figure 4.4(c). The short segments of the brighter domains cover approximately 39% of the total area of Figure 4.4(c). Thus, it should correspond to the PMMA-rich domains. The SAXS profile shows q^* at 0.170 nm^{-1} and the higher-order

Bragg peaks at $q/q^* = 1: 1.76 (\sqrt{3}): 2.66 (\sqrt{7})$ as illustrated in Figure 4.5. This implies that the cylindrical PMMA domains with $l_0 = 37$ nm were formed. It is speculated that the cylindrical PMMA-rich domains may be kinetically trapped during the solvent evaporation process,^{17,26} resulting in a short-ranged ordered self-assembled morphology.

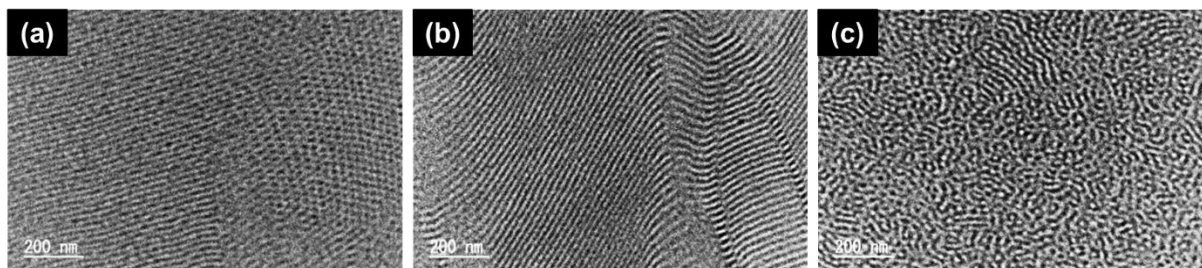


Figure 4.4 TEM images of as-cast PMMA-b-PtBA with $\phi_{\text{PtBA}} =$ (a) 31, (b) 52, and (c) 67 wt%. The bright and dark domains in the TEM image corresponds to the PMMA and PtBA rich domains, respectively.

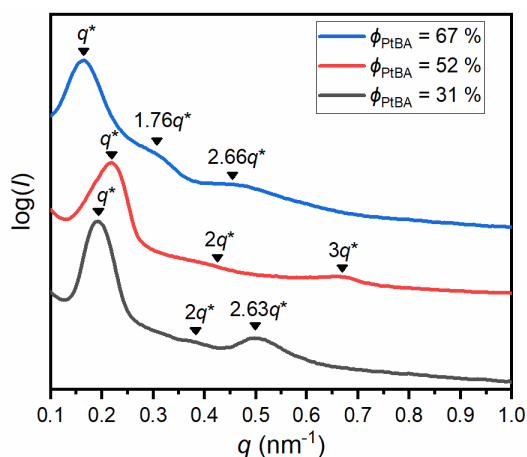


Figure 4.5 SAXS profile of as-cast PMMA-b-PtBA films with $\phi_{\text{PtBA}} = 31, 52,$ and 67 wt%. The positions of scattering peaks are marked by black triangles, where the scattering vectors of the first-order Bragg peak (q^*) are $0.190, 0.219,$ and 0.170 nm^{-1} for $\phi_{\text{PtBA}} = 31, 52,$ and 67 wt%, respectively.

The cell structures of the PMMA-b-PtBA nanocellular foams prepared from the different self-assembled morphologies were observed by SEM. As a reference, the SEM images of the as-cast films of different ϕ_{PtBA} are shown in Figure 4.6. A long-range ordered stripe pattern was observed in Figures 4.5 (a) and (b), which could represent the self-assembled PtBA cylinders ($\phi_{\text{PtBA}} = 31$ wt%) and lamella morphologies ($\phi_{\text{PtBA}} = 52$ wt%), respectively. A short-range pattern was observed in Figure 4.6 (c), which is consistent with the PMMA cylindrical morphology ($\phi_{\text{PtBA}} = 67$ wt%) observed by the TEM image of Figure 4.4(c). In all cases, the SEM images mainly represent the self-assembled morphologies, and no cellular structure was observed.

Figure 4.7 illustrates the cell structure formed by foaming the self-assembled films at 80-100 °C for 5 minutes. From the cylindrical PtBA-rich domains, highly ordered spherical domains are formed as shown in Figure 4.7(a-c), where the cell sizes were 17, 25, and 26 nm in the PMMA-b-PtBA films foamed at 80, 90, and 100 °C. The density and expansion ratio of the as-cast and nanocellular foams are summarized in Table 4.2. The expansion ratios of PMMA-b-PtBA foamed at 80, 90, and 100 °C, were 1.01, 1.08, and 1.10, respectively. As discussed in Chapter 3, at the given temperature range, the gas generated in the PtBA-rich domains is insufficient to fully expand the cells throughout the cylindrical domains and only spherical cells are created.

In the case of the lamella morphology, many small cells were observed in the PtBA-rich domains after being foamed at 80 °C for 5 minutes (Figure 4.7(d)). While some cells coalesced with each other and formed slightly elongated cells at 80 °C, the cells were fully merged and expanded in the PtBA-rich domains at 90 °C (Figure 4.7(e)). The width of the PtBA-rich domain increased from 16 to 43 nm with the increase of foaming temperature from 80 to 90 °C. It should be noted that the width of the PMMA-rich domains remained unchanged at c.a. 35-40 nm, suggesting that no cell was formed in the PMMA-rich domains. At the foaming temperature, 100 °C, the cell size changed abruptly to hundreds of micrometers and a microcellular foam was formed (Figure 4.7(f)). The drastic change in the cell structure at 100 °C could be caused by a sharp increase in the amount of gas generated in the PtBA-rich domains. According to the isothermal TGA measurements at 100 °C (Figure 4.8), the amount of gas (i.e. TGA weight loss) generated by the 5 minutes heating was increased from 10 wt% for the cylindrical PtBA-rich morphology to 15 wt% for the lamella PtBA-rich morphology. Thus, it is speculated that the increase of the amount of generated gas can freely expand along with the interface between the PtBA and PMMA-rich lamella domains whilst pushing off the PMMA-rich matrix domains. The stability (rigidity) of the PMMA matrix domain is another factor that significantly influences cell expansion. As shown in Table 4.1, T_g of PMMA in PMMA-b-PtBA with ϕ_{PtBA} of 31 and 52 wt% are 125 and 123 °C, respectively. The T_g measurements suggest that the PMMA-rich domains were in a glassy state during the foaming. However, some of the past studies have shown that T_g of the PMMA domains could significantly decrease near the vicinity of low- T_g polymers in nanometer-scale morphology, which could move the domains in the order of 10 to 100 nm.²⁷⁻³¹ For this reason, it is expected that the rigidity of the PMMA-rich domains in the lamella morphology would decrease and allow cells to expand larger with the increase of PtBA-rich domain fraction. As listed in Table 2, the maximum expansion was 1.10 for PMMA-b-PtBA with $\phi_{\text{PtBA}} = 31$ wt%. The expansion ratios of PMMA-b-PtBA with $\phi_{\text{PtBA}} = 52$ wt% foamed at 80 and 90 °C were 1.21 and 1.48, respectively. This is a significant increase compared to the expansion ratio of $\phi_{\text{PtBA}} = 31$ wt%.

For short-range ordered cylindrical PMMA morphology, microcellular foams were created at 80 °C (Figure 4.7(g)), and the cell size further increases at higher foaming temperatures (Figure 4.7(h,i)). When compared to previous self-assembled morphologies which have minor PtBA domains, the polymer matrix for PtBA-b-PMMA with ϕ_{PtBA} to 67% consists of the PtBA-rich domains. Due to this, the isobutene gas created in the PtBA-rich domains can freely expand creating microcellular foams. Therefore, in order to control the cell ordering at the nano-scale, a continuous PMMA-rich matrix is required to maintain the framework of the self-assembled morphology during the foaming process.

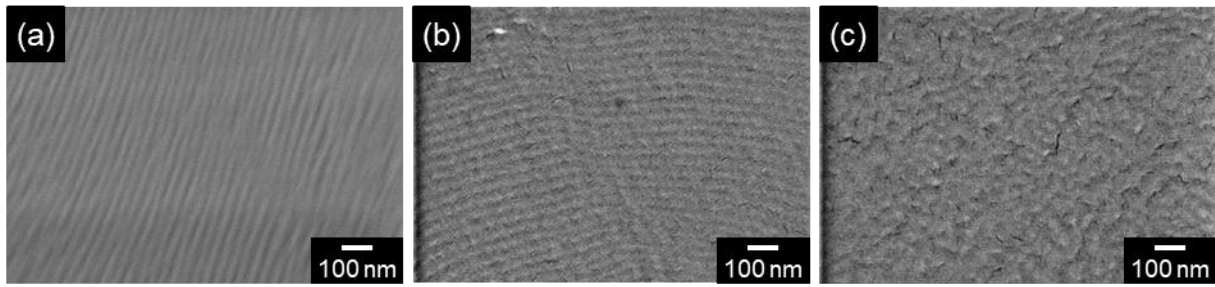


Figure 4.6 SEM images of as-cast PMMA-b-PtBA with ϕ_{PtBA} = (a) 31, (b) 52, and (c) 67 wt%.

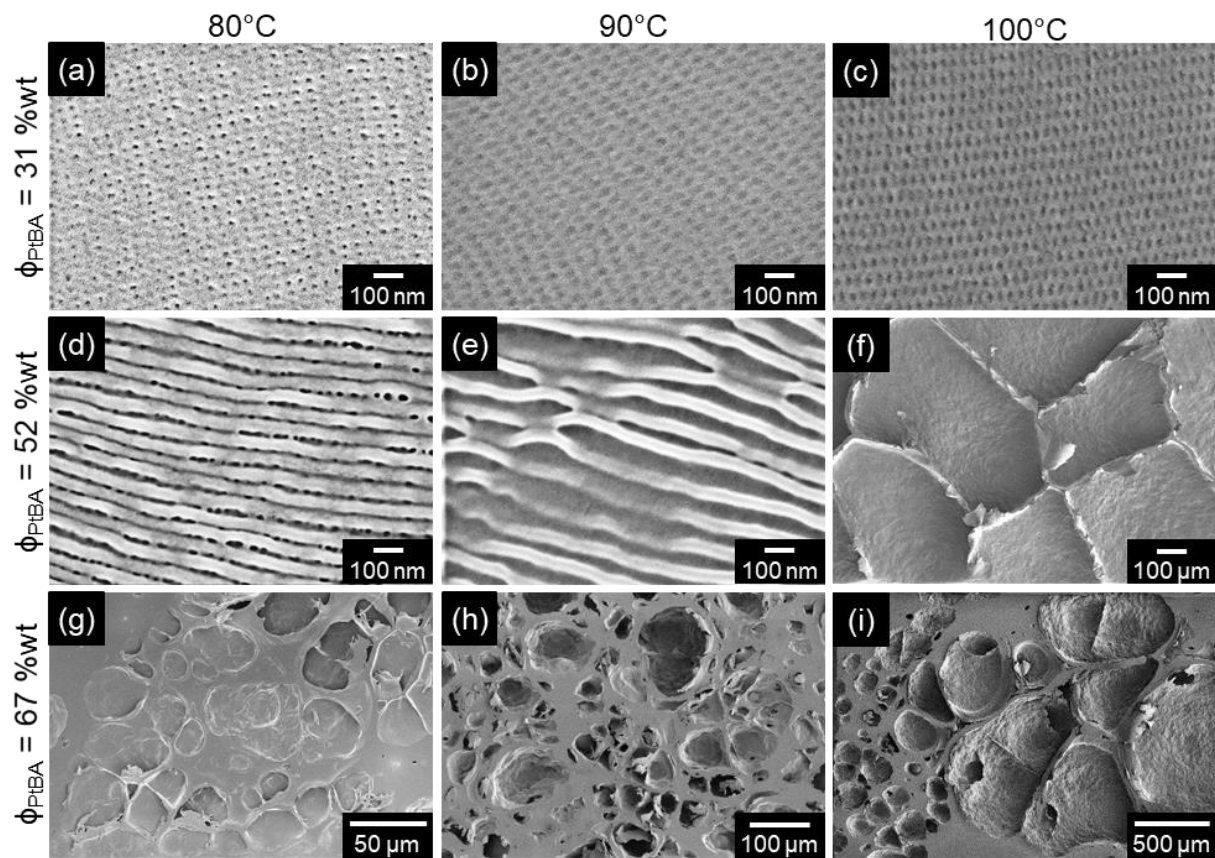


Figure 4.7 SEM images of foamed PtBA-b-PMMA with different PtBA weight fractions (ϕ_{PtBA}): (a-c) 31 wt%, (d-f) 52 wt% and (g-i) 66 wt%. ((a, d, g) foamed at 80, (b, e, h) at 90 and (c, f, i) at 100 °C, foaming time = 5 minutes.)

Table 4.2 Change in density, expansion ratio, and void fraction of PMMA-b-PtBA with $\phi_{\text{PtBA}} = 31$ and 52 wt% foamed at 80-100 °C for 5 minutes. The density measurements were only conducted for as-cast and nanocellular foams.

ϕ_{PtBA} (wt%)	Conditions	Density (g/cm ³)	Expansion Ratio
30.5	As-Cast	1.26	-
	80 °C 5 min	1.25	1.01
	90 °C 5 min	1.17	1.08
	100 °C 5 min	1.14	1.10
52.2	As-Cast	1.26	-
	80 °C 5 min	1.04	1.21
	90 °C 5 min	1.03	1.48

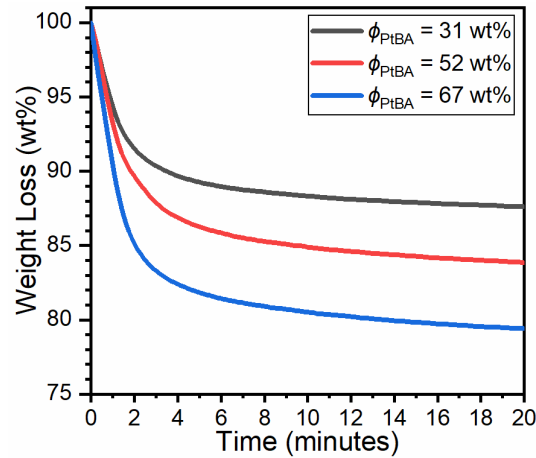


Figure 4.8 Isothermal TGA thermographs of PMMA-b-PtBA after UV-irradiation for PMMA-b-PtBA with $\phi_{\text{PtBA}} = 31$, 51 and 67 wt% at 100°C.

4.3.2 Effect of the molecular weight on the cell structure

Self-assemblies of block copolymer were prepared from symmetric PMMA-b-PtBA with different M_n ranging from 25,500 to 233,200 to study the effect of the molecular weight on the cell structure. The self-assembled morphology was observed by the TEM. The obtained TEM images are shown in Figure 4.9. For PMMA-b-PtBA with $M_n = 25,500$, no self-assembled morphology was observed, whereas a lamella morphology was formed at larger M_n . The transition between the ordered and disorder phase separation for the lamella morphology is expected to occur at $\chi N = 10.5$ ^{11,32}. Using Equation (4.1), the Flory-Huggins interaction parameter between PMMA and PtBA was estimated to be $\chi = 0.08$ at room temperature, where the molar volume (V) is 100 cm³/mol,³³ and the solubility parameter for PMMA and PtBA are 19.88 and 18.46 MPa^{1/2}, respectively.⁷ χN for PMMA-b-PtBA with different M_n are summarized in Table 4.3. For PMMA-b-PtBA block copolymer with $M_n = 25,500$, the segregation strength was

estimated as $\chi N = 18$, which was higher than the order-disorder χN value. It is speculated that the disordered state for $M_n = 25,500$ is mainly due to the overestimation of the Flory-Huggins parameter for the solvent annealing^{20,34} and no consideration of thermal fluctuation effects on the phase separation.^{5,35} As the M_n increases, the χN value could be high enough to compensate for the solvent and thermal fluctuation effects to allow lamella morphologies to be formed.

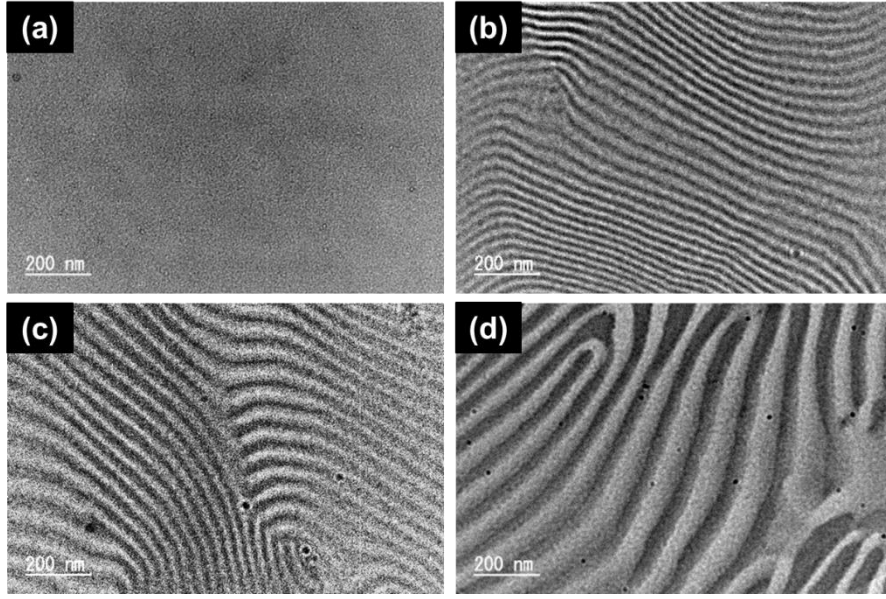


Figure 4.9 TEM images of self-assembled morphology of symmetric PtBA-b-PMMA with different M_n of (a) 25,500, (b) 73,800, (c) 117,300, and (d) 233,200. The bright and dark domains correspond to the PMMA and PtBA rich domains, respectively.

$$\chi = \frac{V}{RT} (\delta_{PtBA} - \delta_{PMMA})^2 \quad (4.1)$$

Table 4.3 χN for PtBA-b-PMMA with $M_n = 25,500, 73,800, 117,300$ and $233,200$ estimated using Equation (4.1).

Sample	M_n	ϕ_{PtBA} (wt%)	χN
4	25,500	58.9	18
5	73,800	56.6	52
6	117,300	55.1	84
7	233,200	56.6	166

For the copolymer whose M_n is larger than 25,500, self-assembly of large lamella morphologies was formed as shown in Figures 4.9(b-d). The minimum pitch of the lamellae (l_0) was estimated from the first-order Bragg peak of the SAXS profile (Figure 4.10(a)) using Equation (2.1). The l_0 for PMMA-b-PtBA of $M_n = 73,800$, 117,300, and 233,200 were 44, 70, and 130 nm, respectively. From the pitch data, a power-law relationship, i.e., $l_0 \propto M_n^\alpha$, with the exponent α of 0.92 was derived as illustrated in Figure 4.10(b). The deviation of α from the theoretical value, i.e., $2/3$,¹⁴⁻¹⁶ indicates that the lamella morphology did not reach an equilibrium state. The insufficient equilibration was observed from the TEM images, where the width of the lamella morphology largely varied as shown in Figure 4.9 (b-d). It is expected that longer solvent casting or additional solvent annealing could improve the equilibration of the self-assembled domains. Nevertheless, the current self-assembled lamella morphologies are already distinct enough to investigate the effect of the M_n on the cell expansion.

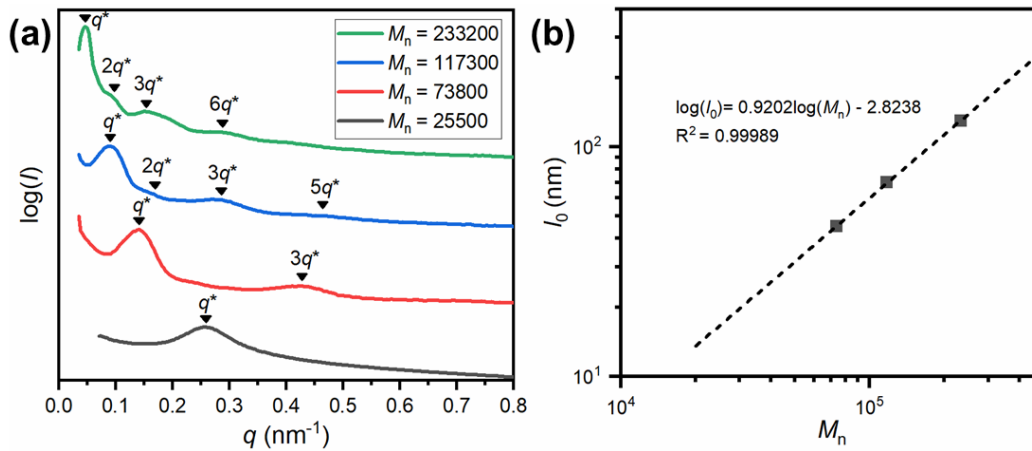


Figure 4.10 (a) SAXS profiles of the symmetric PtBA-b-PMMA with $M_n = 25,500$, 73,800, 117,300, and 233,200. The black triangle: scattering peaks, where the first-order Bragg peak (q^*) was 0.259, 0.142, 0.090, and 0.048 nm^{-1} at $M_n = 25,500$, 73,800, 117,300, and 233,200, respectively. (b) The lamella l_0 estimated from the SAXS profile as a function of M_n .

The formation and cell expansion of PMMA-b-PtBA nanocellular foams with different M_n were observed by SEM. As a reference, the SEM images of the as-cast films was shown in Figure 4.11. For $M_n = 25,500$, no self-assembled morphology was observed by the SEM observation shown in Figure 4.11(a), similarly to the TEM images illustrated in Figure 4.9(a). On the other hand, the stripe-like patterns corresponding to self-assembled lamella morphologies were observed for PMMA-b-PtBA with $M_n = 73,800$, 11,7300, and 233,200.

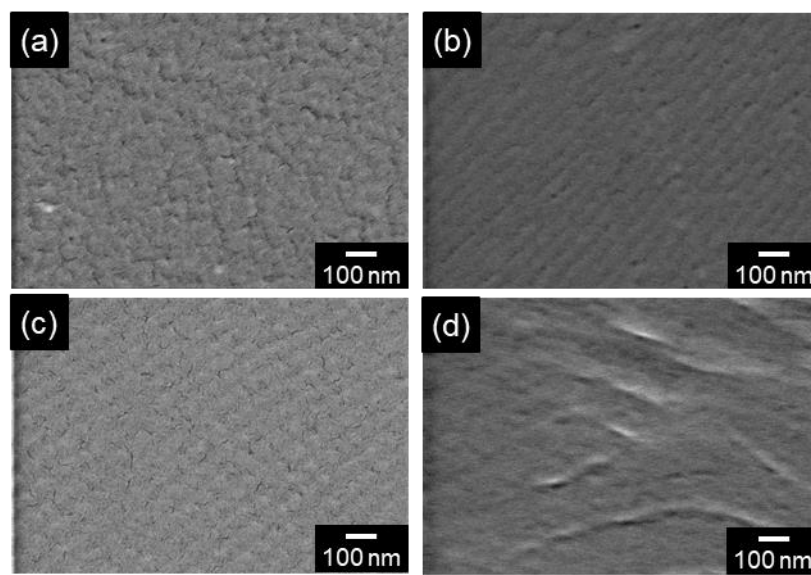


Figure 4.11 SEM images of as-cast PMMA-b-PtBA with M_n = (a) 25,500, (b) 73,800, (c) 117,300 and (d) 233,200.

The PMMA-b-PtBA films were foamed using their self-assembled morphology as the templates of foaming at 80-100 °C for 5 minutes. The obtained cellular structures are summarized in Figure 4.12. From the disordered template ($M_n = 25,500$), cells with a few tens of nanometer sizes were sparsely formed at 80 °C foaming temperature. At higher foaming temperatures, these nanocellular foams completely expanded to the micrometer scale cells. Due to the homogeneous PMMA and PtBA phase for $M_n = 25,500$, the glass transient temperature was estimated by Fox-Equation to be $T_g = 68$ °C.³⁶ Considering the viscosity and the diffusivity of the acids estimated by Vogel–Tamman–Fulcher (VTF) equation,^{37–39} it can be said that the transition from nanocellular to microcellular foams occurs between 80 and 90 °C because the foaming temperature was much higher than the T_g estimated by Fox-Equation. At 90 °C a much higher acid diffusion and lower polymer viscosity are expected, resulting in a microcellular cell expansion.

In the case of PMMA-b-PtBA lamella morphologies ($M_n > 25,500$), the cell size and the cell locations were effectively controlled by the self-assembled morphology at 80 °C, as shown in Figure 4.12(d,g,j). As shown in Figure 4.12(e,h,k), the width of the darker stripes, representing the nanoscale-size groove, becomes larger as the foaming temperature increases to 90 °C. Figure 4.13 shows the cross-section of the foamed film, where nano-sized hollow tubes were formed in the film. It is speculated that at 80 °C nano-sized hollow tubes were formed along with the PtBA-rich lamella domains, which undergoes further gas expansion across the surrounding polymer matrix when the foaming temperature was set at 90 °C or above. The width of the grooves or the diameter of the hollow tube can be estimated from the SEM images shown in Figure 4.12, and the results are summarized in Table 4.4. The densities of the as-cast and the PMMA-b-PtBA foams were also determined by a flotation method. The expansion ratios were calculated from these densities using Equation 3.5. and are shown in Table 4.4. Nanocellular foams with wider hollow tubes were prepared from PMMA-b-PtBA films with higher M_n , due to the larger self-assembled PtBA-rich domains in higher M_n PMMA-b-PtBA.

Interestingly, the opposite trend was observed at the expansion ratios, where the foams with higher expansion were created from PMMA-b-PtBA with higher M_n . For nanocellular foams produced at 90 °C, the expansion ratio decreased from 1.41, 1.38, and 1.22 for PMMA-b-PtBA with $M_n = 73800$, 117300, and 233200. This trend was similarly observed at 100°C, where the lamella morphology was only maintained at the film of $M_n = 233,200$ with the expansion ratio of 1.36. In contrast, the tubes of the other M_n films freely expanded and formed a microcellular foam. The decrease in expansion ratio may be due to the sharp increase in viscosity (η_0) of the PMMA-rich domains with higher M_n , commonly expressed by the Flory-Fox equation as $\eta_0 \propto M_n^{3.4}$.⁴⁰ The η_0 for PtBA-b-PMMA with $M_n = 117,300$ and 233,200 are expected to be approximately 5 and 50 times that of $M_n = 73,800$. This suggests that the matrix domain viscosity is a major factor for controlling the cell expansion, especially at high foaming temperatures.

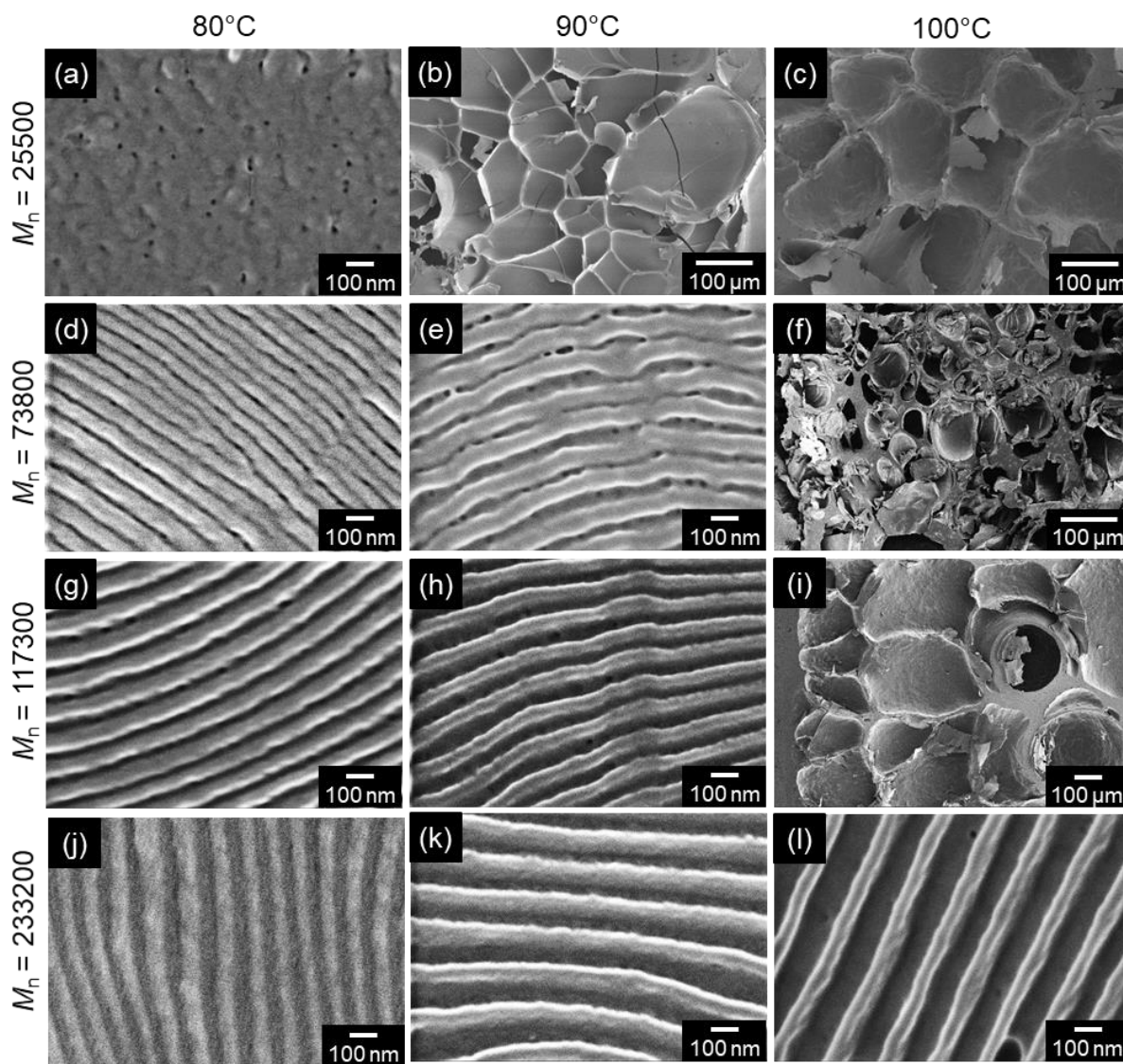


Figure 4.12 SEM images of foamed PtBA-b-PMMA with different M_n : (a-c) 25,500, (d-f) 73,800, (g-i) 117,300 and (j-l) 233,200. ((a, d, g, j) foamed at 80, (b, e, h, k) at 90 and (c, f, i, l) at 100 °C, foaming time = 5 minutes.)

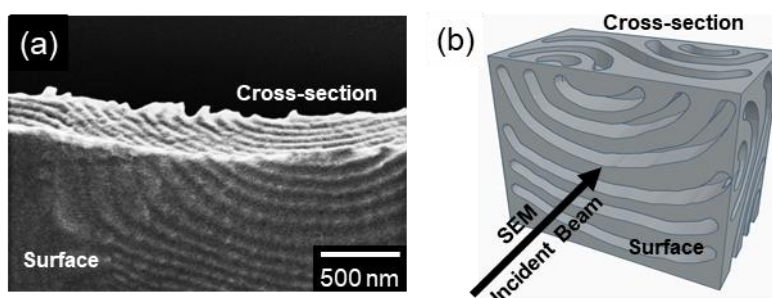


Figure 4.13 Cell structure at the edge of a microtome sample of PMMA-b-PtBA with $M_n = 117,300$: (a) SEM image and (b) a schematic image of the SEM observation

Table 4.4 Change in cell width, density, and expansion ratio of PMMA-b-PtBA with different M_n foamed at 80-100 °C for 5 minutes.

M_n (g/mol)	Conditions	Cell width (nm)	Density (g/cm ³)	Expansion Ratio
73800	As-cast	-	1.25	-
	80 °C 5 min	17 ± 3	1.06	1.17
	90 °C 5 min	43 ± 13	0.88	1.41
	100 °C 5 min	Microcellular	-	-
117300	As-cast	-	1.26	-
	80 °C 5 min	29 ± 4	1.10	1.14
	90 °C 5 min	61 ± 20	0.91	1.38
	100 °C 5 min	Microcellular	-	-
233200	As-cast	-	1.26	-
	80 °C 5 min	42 ± 7	1.12	1.13
	90 °C 5 min	76 ± 21	1.04	1.22
	100 °C 5 min	109 ± 15	0.92	1.36

4.4 Conclusion

In this chapter, the effect of the PMMA-b-PtBA self-assembled morphology on the cell structure generated from UV-induced chemical foaming was studied. Self-assembled cylindrical and lamella PtBA-rich morphologies, as well as short-ranged ordered cylindrical PMMA morphologies, were created by changing the weight fraction of the PtBA block. These different self-assembled morphologies were shown to largely influence the cellular structure and the expansion ratio of the nanocellular foams. By increasing the amount of the foamable domain (PtBA-rich domain),

more isobutene gas can be generated from the PtBA-rich domains, while a less stable PMMA-rich matrix is formed, resulting in a highly expanded cellular structure. This is demonstrated by the highly-ordered spherical cells created from PtBA-rich cylindrical domains compared to the nano-sized hollow tubes created from the lamella morphology. Furthermore, the microcellular foams created from cylindrical PMMA morphologies also emphasize the importance of maintaining a stable PMMA-matrix domain to control the cell expansion within the nanometer scale.

The molecular weight of PMMA-b-PtBA was shown to largely influence the cell size and expansion ratio of the nanocellular foams produced from lamella self-assembled morphology, affecting the pitch of the lamella self-assembly and the viscosity of the PMMA-rich matrix domain. We have demonstrated that the cell size of the nanocellular foam increased from 16 to 43 nm for $M_n = 73,800$ and 233,200 foamed at 80 °C, due to the larger self-assembled lamellar morphology. On the other hand, the higher PMMA-rich domain viscosity suppresses the cell expansion, while allowing the nanocellular foams to be created at higher foaming temperatures.

4.5 References

- (1) Cheng, J. Y.; Ross, C. A.; Smith, H. I.; Thomas, E. L. Templated Self-Assembly of Block Copolymers: Top-Down Helps Bottom-Up. *Adv. Mater.* **2006**, *18* (19), 2505–2521. <https://doi.org/10.1002/ADMA.200502651>.
- (2) Albert, J. N. L.; Epps, T. H. Self-Assembly of Block Copolymer Thin Films. *Mater. Today* **2010**, *13* (6), 24–33. [https://doi.org/10.1016/S1369-7021\(10\)70106-1](https://doi.org/10.1016/S1369-7021(10)70106-1).
- (3) Darling, S. B. Directing the Self-Assembly of Block Copolymers. *Prog. Polym. Sci.* **2007**, *32* (10), 1152–1204. <https://doi.org/10.1016/J.PROGPOLYMSCI.2007.05.004>.
- (4) La, Y. H.; Edwards, E. W.; Park, S. M.; Nealey, P. F. Directed Assembly of Cylinder-Forming Block Copolymer Films and Thermochemically Induced Cylinder to Sphere Transition: A Hierarchical Route to Linear Arrays of Nanodots. *Nano Lett.* **2005**, *5* (7), 1379–1384. <https://doi.org/10.1021/nl0506913>.
- (5) Gronheid, R.; Nealey, P. F. *Directed Self-Assembly of Block Co-Polymers for Nano-Manufacturing*, 1st ed.; Elsevier: Amsterdam, Netherlands, 2015. <https://doi.org/10.1016/c2014-0-03748-3>.
- (6) Ahn, H.; Park, S.; Kim, S.-W.; Yoo, P. J.; Yeol Ryu, D.; Russell, T. P. Nanoporous Block Copolymer Membranes for Ultrafiltration: A Simple Approach to Size Tunability. *ACS Nano* **2014**, *8* (11), 11745–11752. <https://doi.org/10.1021/nn505234v>.
- (7) Park, S.; Jun, T.; Yoon, H. R.; Jo, S.; Kim, J. H.; Ryu, C. Y.; Ryu, D. Y. Nanoporous Structures from PS-b-PMMA-b-PtBA Triblock Copolymer and Selective Modification for Ultrafiltration Membranes. *ACS Appl. Polym. Mater.* **2019**, *1* (3), 584–592. <https://doi.org/10.1021/acsapm.9b00050>.
- (8) Thurn-Albrecht, T.; Steiner, R.; DeRouchey, J.; Stafford, C. M.; Huang, E.; Bal, M.; Tuominen, M.; Hawker, C. J.; Russell, T. P. Nanoscopic Templates from Oriented Block Copolymer Films. *Adv. Mater.* **2000**, *12* (11), 787–791. [https://doi.org/10.1002/\(SICI\)1521-4095\(200006\)12:11<787::AID-ADMA787>3.0.CO;2-1](https://doi.org/10.1002/(SICI)1521-4095(200006)12:11<787::AID-ADMA787>3.0.CO;2-1).

- (9) Chan, V. Z. H.; Hoffman, J.; Lee, V. Y.; Iatrou, H.; Avgeropoulos, A.; Hadjichristidis, N.; Miller, R. D.; Thomas, E. L. Ordered Bicontinuous Nanoporous and Nanorelief Ceramic Films from Serf Assembling Polymer Precursors. *Science (80-.)*. **1999**, *286* (5445), 1716–1719.
<https://doi.org/10.1126/science.286.5445.1716>.
- (10) Hsueh, H. Y.; Yao, C. T.; Ho, R. M. Well-Ordered Nanohybrids and Nanoporous Materials from Gyroid Block Copolymer Templates. *Chem. Soc. Rev.* **2015**, *44* (7), 1974–2018.
<https://doi.org/10.1039/c4cs00424h>.
- (11) Feng, H.; Lu, X.; Wang, W.; Kang, N.-G.; Mays, J. W. Block Copolymers: Synthesis, Self-Assembly, and Applications. *Polymers (Basel)*. **2017**, *9* (10), 494. <https://doi.org/10.3390/POLYM9100494>.
- (12) Kim, H.-C.; Park, S.-M.; Hinsberg, W. D. Block Copolymer Based Nanostructures: Materials, Processes, and Applications to Electronics. *Chem. Rev.* **2009**, *110* (1), 146–177. <https://doi.org/10.1021/CR900159V>.
- (13) Hu, H.; Gopinadhan, M.; Osuji, C. O. Directed Self-Assembly of Block Copolymers: A Tutorial Review of Strategies for Enabling Nanotechnology with Soft Matter. *Soft Matter* **2014**, *10* (22), 3867–3889.
<https://doi.org/10.1039/C3SM52607K>.
- (14) Goodson, A. D.; Troxler, J. E.; Rick, M. S.; Ashbaugh, H. S.; Albert, J. N. L. Impact of Cyclic Block Copolymer Chain Architecture and Degree of Polymerization on Nanoscale Domain Spacing: A Simulation and Scaling Theory Analysis. *Macromolecules* **2019**, *52* (23), 9389–9397.
<https://doi.org/10.1021/ACS.MACROMOL.9B02015>.
- (15) Matsushita, Y.; Mori, K.; Saguchi, R.; Nakao, Y.; Noda, I.; Nagasawa, M. Molecular Weight Dependence of Lamellar Domain Spacing of Diblock Copolymers in Bulk. *Macromolecules* **2002**, *23* (19), 4313–4316.
<https://doi.org/10.1021/MA00221A019>.
- (16) Semenov, A. N. Theory of Block Copolymer Interfaces in the Strong Segregation Limit. *Macromolecules* **2002**, *26* (24), 6617–6621. <https://doi.org/10.1021/MA00076A047>.
- (17) Leolukman, M.; La, Y.-H.; Li, X.; Gopalan, P. Morphology Development in Asymmetric Poly(Styrene-*b*-Tert-Butylacrylate) Thin Films by Solvent Annealing. *Polym. J.* **2008**, *40* (9), 825–831.
<https://doi.org/10.1295/polymj.PJ2008014>.
- (18) Cetintas, M.; Kamperman, M. Self-Assembly of PS-*b*-PNIPAM-*b*-PS Block Copolymer Thin Films via Selective Solvent Annealing. *Polymer (Guildf)*. **2016**, *107*, 387–397.
<https://doi.org/10.1016/J.POLYMER.2016.08.033>.
- (19) Kelly, J. Y.; Albert, J. N. L.; Howarter, J. A.; Stafford, C. M.; Epps Iii, T. H.; Fasolka, M. J. Manipulating Morphology and Orientation in Thermally Responsive Block Copolymer Thin Films. *J Polym Sci Part B Polym Phys* **2011**, *50*, 263–271. <https://doi.org/10.1002/polb.23004>.
- (20) F. Hannon, A.; W. Bai; A. Alexander-Katz; A. Ross, C. Simulation Methods for Solvent Vapor Annealing of Block Copolymer Thin Films. *Soft Matter* **2015**, *11* (19), 3794–3805.
<https://doi.org/10.1039/C5SM00324E>.
- (21) Wei-Cheng Chu; Chen-Xin Lin; Shiao-Wei Kuo. Solvent-Tuning of Ordered Mesoporous Silicas Prepared

- through Evaporation-Induced Self-Assembly Templated by Poly(Ethylene Oxide- b - ϵ -Caprolactone). *RSC Adv.* **2014**, *4* (105), 61012–61021. <https://doi.org/10.1039/C4RA11569D>.
- (22) Andreev, G. A.; Hartmanoá, M. Flotation Method of Precise Density Measurements. *Phys. status solidi* **1989**, *116* (2), 457–468. <https://doi.org/10.1002/PSSA.2211160203>.
- (23) Hamley, I.; Castelletto, V. Small-Angle Scattering of Block Copolymers. In *Soft Matter Characterization*; Springer Netherlands, 2008; pp 1021–1081. https://doi.org/10.1007/978-1-4020-4465-6_20.
- (24) Förster, S.; Timmann, A.; Konrad, M.; Schellbach, C.; Meyer, A.; Funari, S. S.; Mulvaney, P.; Knott, R. Scattering Curves of Ordered Mesoscopic Materials. *J. Phys. Chem. B* **2005**, *109* (4), 1347–1360. <https://doi.org/10.1021/jp0467494>.
- (25) Hasegawa, H.; Hashimoto, T.; Kawai, H.; Lodge, T. P.; Amis, E. J.; Glinka, C. J.; Han, C. C. SANS and SAXS Studies on Molecular Conformation of a Block Polymer in Microdomain Space. *Macromolecules* **1985**, *18* (1), 67–78. <https://doi.org/10.1021/MA00143A011>.
- (26) Tong, J. D.; Leclère, P.; Doneux, C.; Brédas, J. L.; Lazzaroni, R.; Jérôme, R. Morphology and Mechanical Properties of Poly(Methylmethacrylate)-b-Poly(Alkylacrylate)-b-Poly(Methylmethacrylate). *Polymer (Guildf)*. **2001**, *42* (8), 3503–3514. [https://doi.org/10.1016/S0032-3861\(00\)00759-X](https://doi.org/10.1016/S0032-3861(00)00759-X).
- (27) Christie, D.; Register, R. A.; Priestley, R. D. Direct Measurement of the Local Glass Transition in Self-Assembled Copolymers with Nanometer Resolution. *ACS Cent. Sci.* **2018**, *4* (4), 504–511. <https://doi.org/10.1021/ACSCENTSCI.8B00043>.
- (28) Christie, D.; Register, R. A.; Priestley, R. D. Role of Chain Connectivity across an Interface on the Dynamics of a Nanostructured Block Copolymer. *Phys. Rev. Lett.* **2018**, *121* (24), 247801. <https://doi.org/10.1103/PhysRevLett.121.247801>.
- (29) Kang, E.; Graczykowski, B.; Jonas, U.; Christie, D.; Gray, L. A. G.; Cangialosi, D.; Priestley, R. D.; Fytas, G. Shell Architecture Strongly Influences the Glass Transition, Surface Mobility, and Elasticity of Polymer Core-Shell Nanoparticles. *Macromolecules* **2019**, *52* (14), 5399–5406. <https://doi.org/10.1021/ACS.MACROMOL.9B00766>.
- (30) Roth, C. B. Polymers under Nanoconfinement: Where Are We Now in Understanding Local Property Changes? *Chem. Soc. Rev.* **2021**, *50* (14), 8050–8066. <https://doi.org/10.1039/D1CS00054C>.
- (31) Wang, Z.; Sun, D.; Wang, X.; Yang, Y.; Li, Y.; Zuo, B.; Huang, J.; Wang, X. Enhanced Dynamics of PMMA Brushes Induced by the Chain Ends of a Flexible Polymer Chain. *Macromolecules* **2021**, *54* (2), 647–654. <https://doi.org/10.1021/ACS.MACROMOL.0C02481>.
- (32) Yoshimura, Y.; Chandra, A.; Nabae, Y.; Hayakawa, T. Chemically Tailored High- χ Block Copolymers for Perpendicular Lamellae via Thermal Annealing. *Soft Matter* **2019**, *15*, 3497–3506. <https://doi.org/10.1039/c9sm00128j>.
- (33) Miquelard-Garnier, G.; Roland, S. Beware of the Flory Parameter to Characterize Polymer-Polymer Interactions: A Critical Reexamination of the Experimental Literature. *Eur. Polym. J.* **2016**, *84*, 111–124. <https://doi.org/10.1016/J.EURPOLYMJ.2016.09.009>.

- (34) Hagita, K.; Aoyagi, T.; Abe, Y.; Genda, S.; Honda, T. Deep Learning-Based Estimation of Flory–Huggins Parameter of A–B Block Copolymers from Cross-Sectional Images of Phase-Separated Structures. *Sci. Reports* 2021 *111* **2021**, *11* (1), 1–16. <https://doi.org/10.1038/s41598-021-91761-8>.
- (35) Kim, S.; Li, W.; Fredrickson, G. H.; Hawker, C. J.; Kramer, E. J. Order–Disorder Transition in Thin Films of Horizontally-Oriented Cylinder-Forming Block Copolymers: Thermal Fluctuations vs. Preferential Wetting. *Soft Matter* **2016**, *12* (27), 5915–5925. <https://doi.org/10.1039/C6SM00739B>.
- (36) Schneider, H. A.; Di Marzio, E. A. The Glass Temperature of Polymer Blends: Comparison of Both the Free Volume and the Entropy Predictions with Data. *Polymer (Guildf)*. **1992**, *33* (16), 3453–3461. [https://doi.org/10.1016/0032-3861\(92\)91103-9](https://doi.org/10.1016/0032-3861(92)91103-9).
- (37) Richter, E.; Hien, S.; Sebald, M. Novel Diffusion Analysis in Advanced Chemically Amplified DUV Resists Using Photometric Methods. *J. Photopolym. Sci. Technol.* **1999**, *12* (5), 695–709. <https://doi.org/10.2494/PHOTOPOLYMER.12.695>.
- (38) Kang, S.; Wu, W.; Choi, K.-W.; Silva, A. De; Ober, C. K.; Prabhu, V. M. Characterization of the Photoacid Diffusion Length and Reaction Kinetics in EUV Photoresists with IR Spectroscopy. *Macromolecules* **2010**, *43* (9), 4275–4286. <https://doi.org/10.1021/MA902548A>.
- (39) Postnikov, S. V.; Stewart, M. D.; Tran, H. V.; Nierode, M. A.; Medeiros, D. R.; Cao, T.; Byers, J.; Webber, S. E.; Wilson, C. G. Study of Resolution Limits Due to Intrinsic Bias in Chemically Amplified Photoresists. *J. Vac. Sci. Technol. B Microelectron. Nanom. Struct. Process. Meas. Phenom.* **1999**, *17* (6), 3335. <https://doi.org/10.1116/1.591007>.
- (40) Fuchs, K.; Friedrich, C.; Weese, J. Viscoelastic Properties of Narrow-Distribution Poly(Methyl Methacrylates). *Macromolecules* **1996**, *29* (18), 5893–5901. <https://doi.org/10.1021/MA951385M>.

Chapter 5 General Conclusion

5.1 Summary of Chapters

The thesis proposes a novel foaming process that addresses two major issues in the production of nanocellular foams as discussed in Chapter 1: (1) the harsh processing conditions and (2) the difficulty in controlling the cell size and cell ordering of nanocellular foams. Due to the harsh processing requirements of conventional foaming processes, the production of nanocellular foams is currently limited to the lab scale. To solve this issue, I proposed a foaming process that utilizes a UV-induced chemical foaming of tert-butyl ester functionalized polymers, such as PtBA and PtBMA. By creating the gas through an acid-catalyzed deprotection of the polymer's functional group, the process allows nanocellular foams to be produced at ambient pressures, relatively low temperatures, and a short foaming time. The cell size and cell order of the nanocellular foams are controlled by utilizing self-assembled block copolymers, consisting of a foamable block and a matrix block, as a template for the foaming. By optimizing the block copolymer specifications and foaming conditions, the gas can be generated and expanded within the foamable domains, resulting in highly-ordered nanocellular foams with controllable cell size and density.

In Chapter 2, block copolymers containing tert-butyl ester functionalized blocks, PS-b-PtBMA and PMMA-b-PtBA, were synthesized by organotellurium-mediated living radical polymerization (TERP). For PS-b-PtBMA, the TERP polymerization was conducted in a homogeneous solution under Azo-initiated thermal, thermal, and photo irradiated conditions. The monomer conversion, M_n , dispersity (\mathcal{D}), polymer weight fraction (ϕ_A), and the number of dead polymers were carefully monitored during the polymerization to evaluate the controllability of the process. For low molecular weight PS-b-PtBMA, with $M_n = 23,300$, well-controlled polymerization was achieved. However, in the case of PS-b-PtBMA with higher molecular weights, the CTA deactivation occurred due to the high viscosity of the polymerization solution, resulting in a relatively large amount of dead polymers (30-60%). To mitigate the effect of the viscosity of the polymerization solution on the formation of dead polymers, PMMA-b-PtBA was synthesized by TERP in an emulsion system. PMMA-b-PtBA with $M_n = 25,500$ to 58,400 with different PtBA weight fractions (ϕ_{PtBA}) were polymerized under the photo-irradiated conditions, with relatively low \mathcal{D} and the less amount of dead polymer when compared to TERP in homogeneous solutions. However, a significant shift in the glass transition temperature of PMMA-b-PtBA was observed where the T_g decreased from 115 to 92 °C for $\phi_{\text{PtBA}} = 34.3$ and 72.2 wt%. The shift of glass transition temperature indicated that some unreacted tBA monomers were polymerized along with MMA, and higher tBA monomer conversion was required. Under the Azo-initiated thermal conditions, the tBA monomer could be increased from 90% to 95% without increasing the number of dead polymers. At this condition, high molecular weight PMMA-b-PtBA with $M_n = 73,800$ -233,200 and a well-controlled structure was created and used in Chapter 4.

In Chapter 3, highly-ordered nanocellular foams were successfully produced from PMMA-b-PtBA with PtBA-rich cylindrical self-assembled morphology by UV-induced chemical foaming. The foaming was conducted by heating at 80-120 °C for 0-10 minutes, based on the glass transition temperature of PtBA ($T_g = 39$ °C) and PMMA ($T_g = 125$ °C), as well as the decomposition of the tert-butyl ester group. As a result, highly-ordered nano-sized spherical

cells with the size and density of $\sim 16\text{--}25$ nm and $\sim 0.8\text{--}1.9 \times 10^{16}$ cells/cm³ were created. Interestingly, the nanocellular foams produced from ~ 150 μm PMMA-*b*-PtBA films remained transparent because the cell size was significantly smaller than the wavelength of light. The effects of the process parameters, such as PAG concentration and foaming temperature, on the cell structure were also investigated. The PAG concentration was shown to mainly affect the cell density of the foam as a result of the increased isobutene gas generation and nucleation sites. The foaming temperature affected the cell size and cell density of the nanocellular foam by increasing the isobutene gas generation and decreasing polymer viscosity. However, the cell expansion at higher foaming temperatures was limited by the amount of gas generated from self-assembled cylindrical morphology with $\phi_{\text{PtBA}} = 30.5$ wt%. Because of this, only spherical cells are produced instead of fully expanding throughout the PtBA-rich domains. UV-penetration experiments were conducted to examine the scalability of the UV-induced chemical foaming process for thicker nanocellular foam samples. Under the current experimental conditions, the maximum thickness of the nanocellular foam sample created by this process is 660 μm .

In Chapter 4, the effect of the self-assembled morphology and M_n on the cell structure was investigated. The self-assembled morphology was shown to largely influence the structure and the expansion ratio of the nanocellular foams. The change in cell structure and expansion was mainly due to the amount of gas generated from the PtBA-rich domains and the stability of the PMMA-rich matrix. This expansion is observed in the transition from spherical cells from cylindrical PtBA morphology to nanocellular channels from lamella PtBA morphology which has higher ϕ_{PtBA} . Nevertheless, a structurally stable PMMA-matrix domain is required to restrict the cell coalescence and expansion to the micrometer scale, as clearly observed for short-ranged ordered PMMA cylindrical morphologies. On the other hand, the M_n influenced the cell size and expansion of the nanocellular foam. By increasing the M_n , the pitch of the self-assembled domains increases, nanocellular foams with larger cell sizes are created. However, the increase in polymer viscosity with M_n results in nanocellular foams with less expansion at high foaming temperatures. At sufficiently high M_n , the increase in polymer viscosity allows a wider foaming temperature window for nanocellular foam preparation, as demonstrated in lamella PtBA morphology with $M_n = 233,200$ compared to $M_n = 73,800$ and 117,300.

5.2 Future Prospects

The production of nanocellular foams by UV-induced chemical foaming from self-assembled block copolymers has been discussed in this thesis, covering the block copolymer synthesis (Chapter 2) by TERP. It also elucidates the fundamental relationships between the process parameters (Chapter 3) and the self-assembled morphology (Chapter 4) on the cell size, shape, ordering, and expansion of the nanocellular foam.

The proposed UV-induced chemical foaming process has some advantages when compared to conventional physical foaming processes. As previously discussed, generating the gas through a chemical reaction allows the foaming process to be conducted at relatively low pressures, mild temperature conditions, and short foaming times.

Apart from the mild foaming conditions, the stable self-assembled template allows control over the cell structure and ordering. To the author's knowledge, this is the first demonstration of the production of highly-ordered

nanocellular foams with controllable cell structures. This could potentially enable the adjustment of the polymer properties for different applications. For instance, by creating highly ordered spherical cells with approximately 17 nm cell size (Chapter 3), highly transparent nanocellular foams could be created with transmittance comparable to the neat material as shown in Figure 5.1. Further optimizing the thermal insulation with respect to the optical properties could allow the material to be used as transparent thermal insulating films for energy-efficient buildings. By improving the long-range ordering and connectivity of the nano-size hollow tubes created from lamella PtBA morphologies in Chapter 4, the nanocellular foams could be utilized in membrane filter applications.

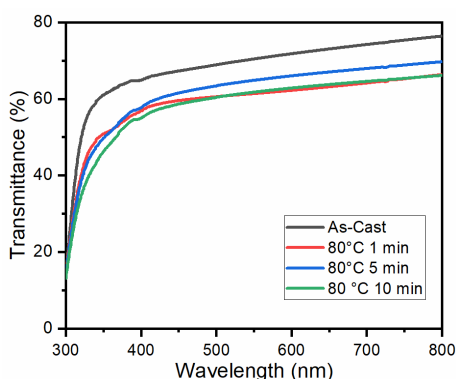


Figure 5.1 Transmittance of nanocellular foams created from cylindrical PMMA-b-PtBA self-assembled template with $M_n = 59000$ and $\phi_{PtBA} = 31$ wt%. The foaming was conducted at 80 °C for 1-10 minutes.

While the UV-induced chemical foaming process of self-assembled block copolymers is a promising method to produce highly-ordered nanocellular foams, the process could be further improved in terms of the block copolymer, self-assembly, and scaling-up the foaming process.

As discussed in Chapter 4, the cell structure of the nanocellular foam produced from the chemical foaming process is highly dependent on the block copolymer specification. By selecting block copolymers with higher glass transition temperatures than PMMA, the stability of the matrix block could be significantly improved. This could allow nanocellular foams to be produced at a larger processing temperature window while maintaining smaller cell sizes. Furthermore, matrix blocks with enhanced properties could be selected, such as using polyimides ($T_g > 300$ °C) for their thermal stability and high mechanical strength.^{1,2} Another area that could be improved is the gas generation from the foamable block. In this thesis, PtBA which produced 1 molecule of isobutene gas per PtBA repeating unit was used to demonstrate the foaming process. However, the gas generation could be by selecting foamable blocks with different functional groups. For instance, tert-butoxycarbonyloxy (TBOC) groups could generate isobutene and CO₂ from acid-catalyzed decomposition, and could potentially allow the production of polymer foams with higher expansion.³⁻⁵

The self-assembly of the block copolymer template could be improved by utilizing directed self-assembly techniques, such as graphoepitaxy⁶⁻⁸ and chemoepitaxy,⁶⁻⁸ or controlled solvent vapor annealing methods,⁹ to create well-aligned self-assembled templates towards a particular direction. Due to the structural stability of the self-assembled template during the chemical foaming process, the well-aligned structure would also be transferred to the nanocellular foam. Such structural anisotropy could potentially improve the thermal, optical, and mechanical properties of the nanocellular foam.

While the UV-induced chemical foaming process of block copolymers was successful on the laboratory scale, there are two major challenges in scaling up the process. The first challenge is that the thickness of the nanocellular foams produced is limited by the UV irradiation step. As discussed in Chapter 3, the UV-penetration for this experimental setup, at a UV wavelength of 254 nm and intensity of 1 mW/cm², was approximately 330 μm. By irradiating both sides of the film, the maximum sample thickness is approximately 660 μm. Thicker films could potentially be created by using longer wavelength irradiation or higher irradiation intensity. For instance, LED light could be paired with visible light PAG,^{10,11} to allow acids to be created in thicker films. To prevent the heating up of the film, which may cause isobutene to be generated prematurely, highly intense light could be repeatedly flashed instead of using a longer exposure time. Another method to allow thicker nanocellular foams to be created is to modify the gas generation method, as shown in Figure 5.2. Thermally liable functional groups, such as p-toluenesulfonylhydrazides (TSH)^{12,13} or 2-hydroxyethyl acrylate groups,¹⁴ can generate gas directly through thermal decomposition. In some cases, an additional catalyst functional group can be embedded in the polymer backbone to facilitate the gas generation, such as the case of amides groups catalyzing the TBOC decomposition. Since no UV-irradiation is required, the process is not limited by the UV penetration depth, and thick polymer foams can be created.

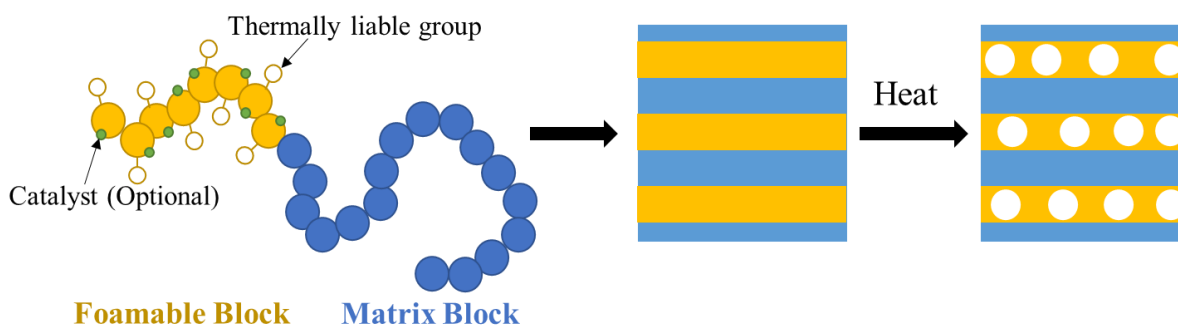


Figure 5.2 Schematic for chemical foaming of self-assembled block copolymers with thermally liable functional groups

The second challenge in scaling up the process is the material cost. In order to create the self-assembled template for the foaming process, the block copolymer should have well-controlled M_n and PDI, as discussed in Chapter 2. Apart from that, large-scale polymer purification processes could be required to remove the contaminants from the polymer. For example, instead of using the preparative GPC, as discussed in Chapter 2, liquid-liquid extraction or adsorption processes¹⁵ may be used to remove the surfactant in large-scale production. For these reasons, the material cost for the proposed UV-induced chemical foaming process is considerably higher than the physical foaming process. Due to this reason, improvement in large-scale block copolymer synthesis and purification is required for the proposed process to be utilized. While unsuitable for general-purpose materials, the UV-induced chemical foaming of block copolymers could be used to create materials that require the production of thin-film polymer foam with high thermal insulation or transparency for specific applications.

5.3 References

- (1) Weiser, E. S.; Johnson, T. F.; St Clair, T. L.; Echigo, Y.; Kaneshiro, H.; Grimsley, B. W. Polyimide Foams for Aerospace Vehicles. *High Perform. Polym.* **2000**, *12* (1), 1–12. <https://doi.org/10.1088/0954-0083/12/1/301>.
- (2) Wang, Y.; Zhou, J.; Hou, J.; Chen, X.; Sun, J.; Fang, Q. High-Performance Polyimides with High Tg and Excellent Dimensional Stability at High Temperature Prepared via a Cooperative Action of Hydrogen-Bond Interaction and Cross-Linking Reaction. *ACS Appl. Polym. Mater.* **2019**, *1* (8), 2099–2107. https://doi.org/10.1021/ACSAPM.9B00400/SUPPL_FILE/AP9B00400_SI_001.PDF.
- (3) Ito, H. Solid-State Thermolysis of Poly(p-t-Butoxycarbonyloxystyrene) Catalyzed by Polymeric Phenol: Effect of Phase Separation. *J. Polym. Sci. Part A Polym. Chem.* **1986**, *24* (11), 2971–2980. <https://doi.org/10.1002/pola.1986.080241124>.
- (4) Jing, C.; Suzuki, Y.; Matsumoto, A. Thermal Decomposition of Methacrylate Polymers Containing Tert-Butoxycarbonyl Moiety. *Polym. Degrad. Stab.* **2019**, *166*, 145–154. <https://doi.org/10.1016/j.polymdegradstab.2019.05.027>.
- (5) Kim, T.-K.; Choi, K.-Y.; Lee, K.-S.; Park, D.-W.; Jin, M. Y. Thermal Conversion of T-Butyloxycarbonyloxy Attached Polyamides to Polybenzoxazoles. *Polym. Bull.* **2000**, *44*, 55–62.
- (6) Darling, S. B. Directing the Self-Assembly of Block Copolymers. *Prog. Polym. Sci.* **2007**, *32* (10), 1152–1204. <https://doi.org/10.1016/J.PROGPOLYMSCI.2007.05.004>.
- (7) Tseng, Y.-C.; Darling, S. B. Block Copolymer Nanostructures for Technology. *Polym. 2010, Vol. 2, Pages 470-489* **2010**, *2* (4), 470–489. <https://doi.org/10.3390/POLYM2040470>.
- (8) Hu, H.; Gopinadhan, M.; Osuji, C. O. Directed Self-Assembly of Block Copolymers: A Tutorial Review of Strategies for Enabling Nanotechnology with Soft Matter. *Soft Matter* **2014**, *10* (22), 3867–3889. <https://doi.org/10.1039/C3SM52607K>.
- (9) Osuji, C. O. Alignment of Self-Assembled Structures in Block Copolymer Films by Solvent Vapor

- Permeation. *Macromolecules* **2010**, *43* (7), 3132–3135. <https://doi.org/10.1021/MA100066E>.
- (10) Shirai, M.; Tsunooka, M. Photoacid and Photobase Generators: Chemistry and Applications to Polymeric Materials. *Prog. Polym. Sci.* **1996**, *21* (1), 1–45. [https://doi.org/10.1016/0079-6700\(95\)00014-3](https://doi.org/10.1016/0079-6700(95)00014-3).
- (11) Takahashi, Y.; Kodama, S.; Ishii, Y. Visible-Light-Sensitive Sulfonium Photoacid Generators Bearing a Ferrocenyl Chromophore. *Organometallics* **2018**, *37* (11), 1649–1651. https://doi.org/10.1021/ACS.ORGANOMET.8B00203/SUPPL_FILE/OM8B00203_SI_001.PDF.
- (12) Jeong, J.; Kim, T.; Cho, W.-J.; Chung, I. Synthesis and Decomposition Performance of a Polymeric Foaming Agent Containing a Sulfonyl Hydrazide Moiety. *Polym. Int.* **2012**, *62* (7), n/a-n/a. <https://doi.org/10.1002/pi.4398>.
- (13) Jeong, J.; Yang, J.; Ha, C. S.; Cho, W. J.; Chung, I. Synthesis and Characterization of Polymeric Foaming Agent Containing Sulfonyl Hydrazide Moiety. *Polym. Bull.* **2012**, *68* (5), 1227–1238. <https://doi.org/10.1007/s00289-011-0600-2>.
- (14) Iseki, M.; Suzuki, Y.; Tachi, H.; Matsumoto, A. Design of a High-Performance Dismantlable Adhesion System Using Pressure-Sensitive Adhesive Copolymers of 2-Hydroxyethyl Acrylate Protected with Tert-Butoxycarbonyl Group in the Presence of Cross-Linker and Lewis Acid. *ACS Omega* **2018**, *3* (11), 16357–16368. https://doi.org/10.1021/ACSOMEGA.8B02371/SUPPL_FILE/AO8B02371_SI_001.PDF.
- (15) Tyrode, E.; Rutland, M. W.; Bain, C. D. Adsorption of CTAB on Hydrophilic Silica Studied by Linear and Nonlinear Optical Spectroscopy. *J. Am. Chem. Soc.* **2008**, *130* (51), 17434–17445. https://doi.org/10.1021/JA805169Z/SUPPL_FILE/JA805169Z_SI_001.PDF.

Appendix: Supporting Information

A.1 Matlab Codes for the SEC peak normalization

```
clear
clc
%% Import data
fileloc="C:\Users\MPE6\Desktop\Podchara Rattanakawin\2020 synthesis\pr149";
filename="pr149";
file=fileloc+"\ "+filename+".xlsx";
sheet="ptba3h";
x=[linspace(0,30,18001)]';
yraw=xlsread(file,sheet,'b1:b54001');

%% baseline settings
xstart=13;
xend=19;

%% Convert y to same x
y=zeros(18001,1);
for i=1:18001
    y(i)=yraw((i-1)*3+1);
end

%% baseline correction (1 point)
xendloc=find(x==xend);
xstartloc=find(x==xstart);
ystart=y(xstartloc);
yblcor=y-ystart;

%% normalization find peak between start and end of baseline
yfindpeak=zeros(xendloc:1);
for j=1:xendloc
    yfindpeak(j)=yblcor(j);
end
```

```

ymax=max(yfindpeak);
ynorm=yblcor/ymax;

% plot(x,ynorm)
%% write to excel
xlswrite(file,y,sheet,"c1:c18001")
xlswrite(file,x,sheet,"e1:e18001")
xlswrite(file,ynorm,sheet,"f1:f18001")

```

A.2 Matlab Codes for the TEM image FFT analysis

```

clear
clc

%% import rgb image(use imagej to convert resize image)
image1= "ps-50-chcl340cslo-80c5min_i029-rgb-1008nmpix";
imagenamename=image1+".jpg";
sem1 =imread(imagenamename);
scale=1.008 %scale of image pix/nm

%% convert image to gray image + reconfig
semgs=rgb2gray(sem1);
sem2= double(semgs)/256;
image(semgs)

%% perform FFT transform on image
fft=fft2(sem2);
fft=abs(fftshift(fft));%format so that the image is according to the pixel
coordinate
for fftx1= 348:353 % reduce effect of center pixel on brightness
    for ffty1= 348:353
        fft(fftx1,ffty1)=1;
    end
end
end

```

```

%% Plot and save
fftcop2=fft(251:450,251:450);% copy only data at the center
fftcop2=fftcop2.^1;
figure(1)
imagesc(fftcop2);
x0=0;
y0=0;
width=20;
height=20;
set(gcf,'units','centimeters','position',[x0,y0,width,height])
savenam1=imager1+".png";
saveas(gcf,savenam1)

%% radial average function
function profile = radialAverage(IMG, cx, cy, w)
    % computes the radial average of the image IMG around the cx,cy point
    % w is the vector of radii starting from zero
    [a,b] = size(IMG);
    [X, Y] = meshgrid( (1:a)-cx, (1:b)-cy);
    R = sqrt(X.^2 + Y.^2);
    profile = [];
    for i = w % radius of the circle
        mask = (i-1<R & R<i+1); % smooth 1 px around the radius
        values = (1-abs(R(mask)-i)) .* double(IMG(mask)); % smooth based on
distance to ring
        % values = IMG(mask); % without smooth
        profile(end+1) = mean( values(:) );
    end
end

%% radial average
prof=zeros(1010,2);
for fftx= 1:1010
    prof(fftx,1)=fftx/10;
    if fftx<10
        prof(fftx,2)=0;
    end
end

```

```

        else
            prof(fftx,2)=log10(radialAverage(fftcop2,101,101,fftx/10));
        end
    end
end

%% 1D profile smoothing
order1 = 3;
framelen1= 21;
profsg= sgolayfilt(prof(:,2),order1,framelen1);

%% plot profile
figure(2)
plot(prof(:,1),profsg)
x0=0;
y0=0;
width=15;
height=10;
set(gcf,'units','centimeters','position',[x0,y0,width,height])
savename2=imager1+"-profile.png";
saveas(gcf,savename2)

%% plot profile i-q
figure(3)
profq=prof(:,1).*2*pi().*scale/length(fft);
plot(profq,profsg)
x0=0;
y0=0;
width=15;
height=10;
xlabel('\itq [nm-1]')
ylabel('\itI [-]')
xlim([0.05 profq(length(profq))])
ylim([profsg(length(profsg))-0.1 max(profsg)+0.1])
set(gcf,'units','centimeters','position',[x0,y0,width,height])
savename2=imager1+"-profile-iq.png";
saveas(gcf,savename2)

```


A.3 Estimation of the gas pressure inside the cells

The pressure of the gas inside the cells created in Chapter 3 were determined based on 2 major assumptions: the isobutene behaves as an ideal gas, and the gas is completely converted into the cells. The gas pressure inside the cells (P_g) could be estimated from Equation A.1, where n_g , V_g , T and R are the amount of gas, total volume of the cells, foaming temperature and gas constant.¹ The total volume of the gas could be estimated from the cell size and cell density as previously discussed in Chapter 3 using Equation 3.4 and Equation 3.5. The amount of gas could be estimate from the weight loss (Δm) measured by isothermal at different temperatures and time using Equation A.2, where the polymer density (ρ_p) is 1.25 g/cm³ and the isobutene molecular weight ($M_{w, \text{isobutene}}$) is 56 g/mol.

The pressure of the gas is summarized in Table A.1. At 80 °C for 1-10 minutes foaming, P_g increased from 411.7 to 2266.6 MPa. These values are higher than the elastic modulus (G') at 80 °C, $G' = 385.2$ MPa, and indicates that further expansion is expected to increase with time. While this expansion was observed initially from 1 to 5 minutes with V_g of 2.4×10^{-2} to 3.7×10^{-2} cm³_{gas}/cm³_{polym}, the expansion decreased to 3.3×10^{-2} cm³_{gas}/cm³_{polym} after 10 minutes foaming. This indicates that the isobutene does not completely convert to the cells, and some portion of the gas diffused out.

For nanocellular foams created at 90 and 100 °C for 5 minutes, the pressure significantly decreased when compared to 80 °C. This is most likely due to easier cell expansion due to the softening of the polymer matrix at higher foaming temperatures. As previously discussed in Chapter 3, due to the limited amount of isobutene gas that can be created from PtBA cylindrical morphologies, no significant change in the gas volume was observed for 90 and 100 °C foamed samples.

$$P_g = \frac{n_g RT}{V_g} \quad (\text{A.1})$$

$$n_g = \frac{\Delta m \rho_p}{M_{w, \text{isobutene}}} \quad (\text{A.2})$$

Table A.0.1 Gas pressure inside the cell estimation for nanocellular foams created from PMMA-b-PtBA with $M_n = 59000$ and $\phi_{\text{PtBA}} = 31$ wt%.

Condition	d ^[a] (nm)	N ^[a] (cell/cm ³)	V_g (cm ³ _{gas} /cm ³ _{polym})	Δm ^[b] (g _{gas} /g _{polym})	n_g (mol _{gas} /cm ³ _{polym})	P_g (MPa)
80°C 1 min	18.0	0.78×10^{16}	2.4×10^{-2}	0.015	3.4×10^{-4}	411.7
80°C 5 min	17.0	1.43×10^{16}	3.7×10^{-2}	0.078	17.3×10^{-4}	1358.0
80°C 10 min	16.1	1.54×10^{16}	3.3×10^{-2}	0.117	26.1×10^{-4}	2266.6
90°C 5 min	25.0	1.71×10^{16}	14.0×10^{-2}	0.093	20.1×10^{-4}	440.9
100°C 5 min	25.9	1.69×10^{16}	15.4×10^{-2}	0.107	24.0×10^{-4}	478.0

^[a] Cell size and cell densities estimate from SEM images in Figure 3.9 and Figure 3.15 (c-d)

^[b] TGA weight loss measurements from Figure 3.18

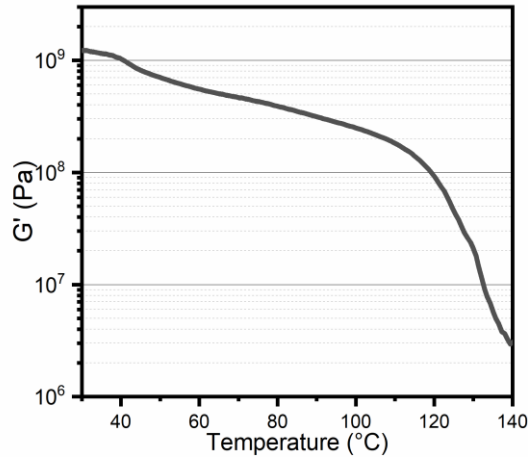


Figure A.0.1 Temperature scan of the elastic modulus (G') of PMMA-b-PtBA without PAG. (Torsion-mode experiments with strain of 0.3 % at frequency of 0.63 rad/s)

Using the gas pressure inside the cells, the growth rate of the bubbles could also be estimated using Equation A.3, where R is the bubble radius, η^* is the complex viscosity of the polymer, P_g and P_f are the pressure inside the cell and the foaming pressure ($P_f = 100325$ Pa) and γ_p is the surface tension of the polymer.¹ The rate of bubble growth (dR/dt) is summarized in Table A.2, where bubble growth is expected for these foaming conditions since $dR/dt > 0$. As previously discussed, this indicates that some isobutene gas diffused out of the foams during the foaming process.

$$\frac{dR}{dt} = \frac{1}{4\eta^*} [(P_g - P_f)R - 2\gamma_p] \quad (\text{A.3})$$

Table A.0.2 Cell growth rate (dR/dt) estimation for nanocellular foams created from PMMA-b-PtBA with $M_n = 59000$ and $\phi_{\text{PtBA}} = 31$ wt%.

Condition	P_g (MPa)	η^* [a] (Pa/s)	γ_p [b] (mN/m)	dR/dt (nm/s)
80°C 1 min	411.7	6.50×10^8	23.73	0.13
80°C 5 min	1358.0	6.50×10^8	23.73	0.43
80°C 10 min	2266.6	6.50×10^8	23.73	0.69
90°C 5 min	440.9	5.21×10^8	23.22	0.25
100°C 5 min	478.0	4.13×10^8	22.71	0.35

[a] Complex viscosity from torsion-mode rheometer measurements in Figure 3.18

[b] Surface tension estimated from $\gamma_{p,\text{PMMA}}$ and $\gamma_{p,\text{PtBA}}$ at different temperatures²

A.4 References

- (1) Xu, D.; Pop-Iliev, R.; Park, C. B.; Fenton, R. G. Fundamental Study of CBA-Blown Bubble Growth and Collapse Under Atmospheric Pressure. *J. Cell. Plast.* **2005**, *41* (6), 519–538.
<https://doi.org/10.1177/0021955X05059031>.
- (2) Brandrup, J.; Immergut, E. H.; Grulke, E. A. *Polymer Handbook*, 4th ed.; John Wiley and Sons Inc.: USA, 1999.

List of Figures and Tables

Figures

Figure 1.1 Schematic of (a) chemical and (b) physical foaming processes	5
Figure 1.2 Cell morphology of polymer foams: (a) closed-cell and (b) open-cell structure	6
Figure 1.3 Strategies for creating nanocellular foams; homogeneous nucleation, heterogeneous nucleation and templated systems.....	9
Figure 1.4 Schematic of the UV induced chemical foaming process with (a) homopolymer/ random copolymers (Kojima et al. ⁸⁴) and (b) self-assembled block copolymers (this study). (c) Acid catalyzed tert-Butyl ester deprotection reaction.	12
Figure 2.1 a) Reversible activation and b) degenerative chain transfer mechanisms in RDRP polymerization	23
Figure 2.2 Emulsion TERP polymerization.....	23
Figure 2.3 Chemical structure of the CTA-1 (a) and the (TeMe) ₂ (b) for homogeneous TERP polymerization.....	24
Figure 2.4 Chemical structure of the CTA-2 (a) and the (TeR) ₂ -2 (b) for emulsion TERP polymerization.....	24
Figure 2.5 Homogeneous TERP polymerization of PS-b-PtBMA. Styrene polymerization under (a) Azo-initiated thermal condition (b) thermal condition. tBMA polymerization under (c) Azo-initiated thermal, (d) thermal, (e) photo-irradiated conditions. Reprinted with permission from Rattanakawin et al., <i>J. Photopolym. Sci. Technol.</i> , 2018 , 31 (5), 647-650. DOI: 10.2494/photopolymer.31.647. Copyright ©2018. Society of Photopolymer Science and Technology (SPST).....	25
Figure 2.6 Emulsion TERP polymerization of PMMA-b-PtBA under (a) photo-irradiation and (b) Azo-initiated thermal conditions.	26
Figure 2.7 Removal of CTAB from PMMA-b-PtBA: (a) extraction with warm NaCl aqueous solution and CHCl ₃ , and (b) preparative GPC. (c) The elution time for the polymer, CTAB and other small molecule contaminants during the preparative GPC purification.	27
Figure 2.8 Monomer conversion by the homogeneous TERP polymerization of PS-b-PtBMA: (a) ¹ H MNR spectra after the PS polymerization, (b) ¹ H MNR spectra after the PtBMA polymerization	28
Figure 2.9 Monomer conversion by the emulsion TERP polymerization of PMMA-b-PtBA: (a) ¹ H MNR spectra after the PtBA polymerization, (b) ¹ H MNR spectra after the PMMAA polymerization	29
Figure 2.10 ¹ H NMR of PMMA-b-PtBA (a) before and (b) after the purification by preparative GPC.....	29
Figure 2.11 Molecular weight change with monomer conversion for (a) PS and (b) PtBMA for Case 1. The dashed line shows the theoretical M_n vs. monomer conversion relationship.	31
Figure 2.12 SEC traces for PS-b-PtBMA synthesized by homogeneous TERP polymerization: (a) Case 1, (b) Case 2, (c) Case 3, (d) Case 4 and (e) Case 5. Reprinted with permission from Rattanakawin et al., <i>J. Photopolym. Sci. Technol.</i> , 2018 , 31 (5), 647-650. DOI: 10.2494/photopolymer.31.647. Copyright ©2018. Society of Photopolymer Science and Technology (SPST).....	32

Figure 2.13 Molecular weight change with monomer conversion for (a) PtBA and (b) PMMA for Case 6. The dashed line represents the theoretical M_n vs. monomer conversion relationship.	33
Figure 2.14 SEC traces for PMMA-b-PtBMA synthesized by emulsion TERP polymerization using the photo-initiated conditions: (a) Case 6, (b) Case 7, (c) Case 8, (d) Case 9, (e) Case 10 and (f) Case 11	34
Figure 2.15 (a) DSC 2 nd heating curves for PMMA-b-PtBA synthesized using photo-irradiated conditions. (b) Relationship between the PtBA weight fraction and the T_g of PMMA-b-PtBA with similar M_n (Case 7-11).....	35
Figure 2.16 Effect of the unreacted tBA monomers during the PMMA polymerization	35
Figure 2.17 SEC traces for PtBA synthesized by emulsion TERP polymerization using Azo-initiated thermal conditions with (a) 0.3, (b) 0.5 and (c) 1.0 equivalent ACVA to the CTA	36
Figure 2.18 SEC traces for PMMA-b-PtBA synthesized by emulsion TERP polymerization using the Azo-initiated thermal conditions: (a) Case 12, (b) Case 13 and (c) Case 14	37
Figure 2.19 DSC 2 nd heating curves for PMMA-b-PtBA synthesized by Azo-initiated thermal conditions.	38
Figure 3.1 (a) Process flow for the UV-induced chemical foaming of self-assembled block copolymer, and (b) acid-catalyzed tert-butyl ester deprotection reaction. Reprinted with permission from Rattanakawin et al., <i>ACS Macro Lett.</i> , 2020 , 9 (10), 1433-1438. DOI: 10.1021/acsmacrolett.0c00475. Copyright ©2020. American Chemical Society.	43
Figure 3.2 Temperature profile for the DSC measurement with heating and cooling rate were 10 °C/min.	45
Figure 3.3 Cell structure analysis by ImageJ: (a) original SEM image and (b) overlay of the analyzed SEM image .	46
Figure 3.4 SAXS profile of as-cast PMMA-b-PtBA films. The black triangles indicate the scattering peaks at $q/q^* = 1, 2$ and $\sqrt{7}$, where the first peak (q^*) is 0.190 nm ⁻¹ . The insert shows a schematic of hexagonally packed cylinders. Reprinted with permission from Rattanakawin et al., <i>ACS Macro Lett.</i> , 2020 , 9 (10), 1433-1438. DOI: 10.1021/acsmacrolett.0c00475. Copyright ©2020. American Chemical Society.....	48
Figure 3.5 Characterization of the self-assembled PMMA-b-PtBA morphology by TEM: (a)TEM image, (b) 2D-FFT image, and (c) 1D-FFT profile. The darker and brighter domains in the TEM corresponds to the PtBA and PMMA rich domains, respectively. The 1D-FFT profile (c) was obtained by radial averaging the 2D-FFT profile (b), and the black triangle in (c) indicates the peak where $q^* = 0.196$ nm ⁻¹ . Reprinted with permission from Rattanakawin et al., <i>ACS Macro Lett.</i> , 2020 , 9 (10), 1433-1438. DOI: 10.1021/acsmacrolett.0c00475. Copyright ©2020. American Chemical Society.	49
Figure 3.6 DSC 2 nd heating curve of PMMA-b-PtBA without PAG. Reprinted with permission from Rattanakawin et al., <i>ACS Macro Lett.</i> , 2020 , 9 (10), 1433-1438. DOI: 10.1021/acsmacrolett.0c00475. Copyright ©2020. American Chemical Society.	50
Figure 3.7 TGA thermograph of PMMA-b-PtBA films after 3600 mJ/cm ² UV-irradiation: (a) dynamic thermogravimetry from 40 to 120 °C, and (b) isothermal thermogravimetry at 80 °C. Reprinted with permission from Rattanakawin et al., <i>ACS Macro Lett.</i> , 2020 , 9 (10), 1433-1438. DOI: 10.1021/acsmacrolett.0c00475. Copyright ©2020. American Chemical Society.	51

Figure 3.8 Optical microscope images of PMMA-b-PtBA films: (a) as-cast and (b) foamed at 80 °C for 10 minutes. (The size of the films is 7 × 7 × 0.15 mm.) Reprinted with permission from Rattanakawin et al., <i>ACS Macro Lett.</i> , 2020 , 9 (10), 1433-1438. DOI: 10.1021/acsmacrolett.0c00475. Copyright ©2020. American Chemical Society.	51
Figure 3.9 SEM images of PMMA-b-PtBA films foamed at 80 °C for (a) 0, (b) 1, (c) 5 and (d) 10 minutes. Reprinted with permission from Rattanakawin et al., <i>ACS Macro Lett.</i> , 2020 , 9 (10), 1433-1438. DOI: 10.1021/acsmacrolett.0c00475. Copyright ©2020. American Chemical Society.	52
Figure 3.10 Effects of the foaming time at 80 °C on cell size (grey) and cell density (red). Reprinted with permission from Rattanakawin et al., <i>ACS Macro Lett.</i> , 2020 , 9 (10), 1433-1438. DOI: 10.1021/acsmacrolett.0c00475. Copyright ©2020. American Chemical Society.	53
Figure 3.11 Density of PMMA-b-PtBA films foamed at 80 °C for 1-10 minutes. The orange bar and green bars respectively represent the density obtained from pycnometry and one estimated from the SEM observations. Reprinted with permission from Rattanakawin et al., <i>ACS Macro Lett.</i> , 2020 , 9 (10), 1433-1438. DOI: 10.1021/acsmacrolett.0c00475. Copyright ©2020. American Chemical Society.	54
Figure 3.12 FTIR spectrums of the PMMA-b-PtBA films foamed at 80 °C for 0-10 minutes: (a) full FTIR spectra between 1000 – 3500 cm ⁻¹ and (b) FTIR spectra of CH ₃ bond of the tert-butyl ester group in PtBA. Reprinted with permission from Rattanakawin et al., <i>ACS Macro Lett.</i> , 2020 , 9 (10), 1433-1438. DOI: 10.1021/acsmacrolett.0c00475. Copyright ©2020. American Chemical Society.	55
Figure 3.13 SEM images of PMMA-b-PtBA films with PAG concentration of (a) 2.5, (b) 5 and (c) 10 wt% polymer, foamed at 80 °C for 5 minutes. Reprinted with permission from Rattanakawin et al., <i>ACS Macro Lett.</i> , 2020 , 9 (10), 1433-1438. DOI: 10.1021/acsmacrolett.0c00475. Copyright ©2020. American Chemical Society.	56
Figure 3.14 Effects of the PAG concentration on the cell size (grey) and cell density (red) of PMMA-b-PtBA foamed at 80 °C for 5 minutes. The cell size and densities were obtained by analyzing the SEM images shown in Figure 3.13.	56
Figure 3.15 SEM images of PMMA-b-PtBA films foamed at (a) 70, (b) 80, (c) 90, (d) 100, (e) 110 and (f) 120 °C for 5 minutes. Reprinted with permission from Rattanakawin et al., <i>ACS Macro Lett.</i> , 2020 , 9 (10), 1433-1438. DOI: 10.1021/acsmacrolett.0c00475. Copyright ©2020. American Chemical Society.	58
Figure 3.16 Effects of the foaming temperature on the cell size (grey) and cell density (red) of PMMA-b-PtBA foamed at a temperature in the range of 80-120 °C for 5 minutes.	58
Figure 3.17 Temperature scan of the complex viscosity (η^*) of PMMA-b-PtBA without PAG. (Torsion-mode experiments with strain of 0.3 % at frequency of 0.63 rad/s). Reprinted with permission from Rattanakawin et al., <i>ACS Macro Lett.</i> , 2020 , 9 (10), 1433-1438. DOI: 10.1021/acsmacrolett.0c00475. Copyright ©2020. American Chemical Society.	59
Figure 3.18 Isothermal TGA thermographs of PMMA-b-PtBA at 80-100°C for 60 minutes. (The insert shows the decomposition behavior of PMMA-b-PtBA at shorter heating time.)	59

Figure 3.19 SEM images of PMMA-b-PtBA films foamed at (a,c,e) 110, and (b,d,f) 120 °C for (a,b) 1, (c,d) 2 and (e,f) 5 minutes.....	60
Figure 3.20 Optical microscope images of PMMA-b-PtBA foamed at 130 °C for 5 minutes. (The size of the films is 5 × 8 × 0.15 mm.).....	60
Figure 3.21 Schematic image of the UV penetration depth evaluation based on the foamed/non-foamed interface...61	
Figure 3.22 Cross-section SEM images of as-cast PMMA-b-PtBA film with thickness of 450 μm: (a) low magnification and (b-d) high magnification. (a): the observation location of the higher magnification SEM images, (b): top, (c): center and (d): bottom of the film.....	62
Figure 3.23 Cross-section SEM images of PMMA-b-PtBA film with a thickness of 450 μm foamed at 80°C for 5 minutes: (a) low magnification and (b-f) high magnification. (a): the observation location of the higher magnification SEM images, (b): UV-irradiation surface, (c): middle of the foamed layer and (d): foamed/non-foamed interface, (e) non-foamed layer and (e) bottom of the film.....	63
Figure 4.1 Evaluation of the observed PtBA-rich domain fraction: (a) original TEM image and (b) cropped and binarized TEM image used for the analysis.....	69
Figure 4.2 Analysis of the cell structure of nanocellular PMMA-b-PtBA tubes: (a) original SEM image and (b) overlay of the analyzed SEM image.....	70
Figure 4.3 Estimation of the sample density by a flotation method.....	71
Figure 4.4 TEM images of as-cast PMMA-b-PtBA with $\phi_{\text{PtBA}} =$ (a) 31, (b) 52, and (c) 67 wt%. The bright and dark domains in the TEM image corresponds to the PMMA and PtBA rich domains, respectively.	72
Figure 4.5 SAXS profile of as-cast PMMA-b-PtBA films with $\phi_{\text{PtBA}} =$ 31, 52, and 67 wt%. The positions of scattering peaks are marked by black triangles, where the scattering vectors of the first-order Bragg peak (q^*) are 0.190, 0.219, and 0.170 nm ⁻¹ for $\phi_{\text{PtBA}} =$ 31, 52, and 67 wt%, respectively.	72
Figure 4.6 SEM images of as-cast PMMA-b-PtBA with $\phi_{\text{PtBA}} =$ (a) 31, (b) 52, and (c) 67 wt%.....	74
Figure 4.7 SEM images of foamed PtBA-b-PMMA with different PtBA weight fractions (ϕ_{PtBA}): (a-c) 31 wt%, (d-f) 52 wt% and (g-i) 66 wt%. ((a, d, g) foamed at 80, (b, e, h) at 90 and (c, f, i) at 100 °C, foaming time = 5 minutes.).....	74
Figure 4.8 Isothermal TGA thermographs of PMMA-b-PtBA after UV-irradiation for PMMA-b-PtBA with $\phi_{\text{PtBA}} =$ 31, 51 and 67 wt% at 100°C.	75
Figure 4.9 TEM images of self-assembled morphology of symmetric PtBA-b-PMMA with different M_n of (a) 25,500, (b) 73,800, (c) 117,300, and (d) 233,200. The bright and dark domains correspond to the PMMA and PtBA rich domains, respectively.	76
Figure 4.10 (a) SAXS profiles of the symmetric PtBA-b-PMMA with $M_n =$ 25,500, 73,800, 117,300, and 233,200. The black triangle: scattering peaks, where the first-order Bragg peak (q^*) was 0.259, 0.142, 0.090, and 0.048 nm ⁻¹ at $M_n =$ 25,500, 73,800, 117,300, and 233,200, respectively. (b) The lamella l_0 estimated from the SAXS profile as a function of M_n	77

Figure 4.11 SEM images of as-cast PMMA-b-PtBA with $M_n =$ (a) 25,500, (b) 73,800, (c) 117,300 and (d) 233,200.	78
Figure 4.12 SEM images of foamed PtBA-b-PMMA with different M_n : (a-c) 25,500, (d-f) 73,800, (g-i) 117,300 and (j-l) 233,200. ((a, d, g, j) foamed at 80, (b, e, h, k) at 90 and (c, f, i, l) at 100 °C, foaming time = 5 minutes.) ..	79
Figure 4.13 Cell structure at the edge of a microtome sample of PMMA-b-PtBA with $M_n = 117,300$: (a) SEM image and (b) a schematic image of the SEM observation.....	80
Figure 5.1 Transmittance of nanocellular foams created from cylindrical PMMA-b-PtBA self-assembled template with $M_n = 59000$ and $\phi_{PtBA} = 31$ wt%. The foaming was conducted at 80 °C for 1-10 minutes.	87
Figure 5.2 Schematic for chemical foaming of self-assembled block copolymers with thermally liable functional groups	88
Figure A.0.1 Temperature scan of the elastic modulus (g') of PMMA-b-PtBA without PAG. (Torsion-mode experiments with strain of 0.3 % at frequency of 0.63 rad/s)	96

Tables

Table 1.1 Outline of each main chapter in this thesis	13
Table 2.1 Homogeneous TERP polymerization of PS-b-PtBMA. Reprinted with permission from Rattanakawin et al., <i>J. Photopolym. Sci. Technol.</i> , 2018 , 31 (5), 647-650. DOI: 10.2494/photopolymer.31.647. Copyright ©2018. Society of Photopolymer Science and Technology (SPST).....	31
Table 2.2 Emulsion TERP polymerization of PMMA-b-PtBA under photo-irradiated conditions	33
Table 2.3 Glass transition temperatures for PMMA-b-PtBA synthesized using photo-irradiated conditions	35
Table 2.4 Emulsion TERP polymerization of PtBA with different ACVA concentrations	36
Table 2.5 Emulsion TERP polymerization of PMMA-b-PtBA under the Azo-initiated thermal conditions	37
Table 2.6 Glass transition temperatures for PMMA-b-PtBA synthesized using Azo-initiated thermal conditions	38
Table 2.7 Emulsion TERP polymerization of PMMA-b-PtBA under the Azo-initiated thermal conditions	39
Table 4.1 Specification of PtBA-b-PMMA with different molecular weights and PtBA weight fraction (ϕ_{PtBA}).	68
Table 4.2 Change in density, expansion ratio, and void fraction of PMMA-b-PtBA with $\phi_{PtBA} = 31$ and 52 wt% foamed at 80-100 °C for 5 minutes. The density measurements were only conducted for as-cast and nanocellular foams.	75
Table 4.3 χN for PtBA-b-PMMA with $M_n = 25,500, 73,800, 117,300$ and 233,200 estimated using Equation (4.1)..	76
Table 4.4 Change in cell width, density, and expansion ratio of PMMA-b-PtBA with different M_n foamed at 80- 100 °C for 5 minutes.....	80
Table A.0.1 Gas pressure inside the cell estimation for nanocellular foams created from PMMA-b-PtBA with $M_n =$ 59000 and $\phi_{PtBA} = 31$ wt%.	95
Table A.0.2 Cell growth rate (dR/dt) estimation for nanocellular foams created from PMMA-b-PtBA with $M_n = 59000$ and $\phi_{PtBA} = 31$ wt%.	96

Acknowledgement

This research was conducted at the Materials Process Engineering (MPE) Laboratory, Kyoto University, Graduate School of Engineering, Department of Chemical Engineering, and was only accomplished with the help and support of numerous people.

I would like to express my deepest gratitude to my advisor Prof. Masahiro Ohshima, for his guidance during my six years from a research student to Ph.D. in Kyoto University. Since coming to Japan, you have always supported me and made me feel welcomed. Under your tutelage, I have gained significant experience in research relating to polymer science and material processing. Furthermore, you have always encouraged me to think independently and try out new things. Your education policies and hands-on research approach have allowed me to grow as a responsible researcher.

I am extremely grateful to my co-advisor Dr. Kenji Yoshimoto. Whenever I struggled with my research, you were always available for consulting and always provided me with insightful comments. Your knowledge of block copolymer self-assembly, nanotechnology, and photolithography has been the foundation of this thesis. Apart from research-related topics, you have also provided me with great advice regarding my daily life, job applications and always pushed me towards leading a healthy lifestyle.

Furthermore, I would like to thank the present and previous staff at the MPE Laboratory: Assoc. Prof. Shinsuke Nagamine, Assist. Prof. Yuta Hikima, and Project-Specific Assist. Prof. Long Wang. Working with Assoc. Prof. Nagamine, Assist. Prof. Hikima and Assist. Prof. Wang has been extremely fruitful, yielding a great understanding of the material property before and after the foaming process. Their constructive comments have provided a better understanding of the foaming process proposed in this thesis.

I would like to express my sincere gratitude towards the staff and students of Yamago Laboratory, Kyoto University, Institute of Chemical Research: Prof. Shigeru Yamago, Assoc. Prof. Masatoshi Tosaka, Dr. Weijia Fan, and Mr. Yuhan Jiang, for their guidance during my polymerization and self-assembly experiments. From our collaboration, I was able to gain a better understanding of polymer synthesis and evaluation. Even though I am not a part of your research group, you have always helped and warmly welcomed me to your laboratory.

Additionally, I would like to express my deepest appreciation to Prof. Teruaki Hayakawa, Dr. Alvin Chandra and Dr. Kevin Wylie of the Department of Material Science and Engineering, Tokyo Institute of Technology, and Dr. Ryohei Kikuchi of the Ookayama Materials Analysis Division, Tokyo Institute of Technology. Their insight and help with the evaluation of self-assembled block copolymers are crucial to the development of the proposed foaming process.

I would also like to acknowledge the staff at NanoHub, Kyoto University, for their assistance with the evaluation of the structure of the nanocellular foams. Furthermore, the discussions relating to nanotechnologies and the semiconductor industries have been beneficial towards my future career.

I would like to thank Mrs. Maki Yamamoto for her help with scholarship and office-related procedures, which allowed me to conduct my research smoothly. I am also grateful to the former and current members of the MPE laboratory for their discussions, friendship, and support throughout the years. I will truly cherish the time we spent together.

Last but not least, I would like to give my heartfelt appreciation to my family. Throughout the six years in Kyoto University, their encouragement and support has allowed me to pursue my Ph.D. degree.

Podchara Rattanakawin

Materials Process Engineering Laboratory, Department of Chemical Engineering
Graduate School of Engineering, Kyoto University

List of Achievements

Publication

Peer-reviewed Full Papers

- 1) **Podchara Rattanakawin**, Weijia Fan, Shigeru Yamago, Kenji Yoshimoto, Masahiro Ohshima
“Synthesis of Photocleavable Block Copolymers for UV Induced Foaming”
Journal of Photopolymer Science and Technology (Impact Factor: 0.858, 2020), Vol. 31, Issue 5, pp. 647-650, 2018.5
DOI: 10.2494/photopolymer.31.647 (**Chapter 2**)
- 2) **Podchara Rattanakawin**, Kai Yamamura, Kenji Yoshimoto, Masahiro Ohshima
“Development and Optimization of UV-Induced Chemical Foaming Process”
Journal of Photopolymer Science and Technology (Impact Factor: 0.858, 2020), Vol. 32, Issue 5, pp. 693-698, 2019.4
DOI: 10.2494/photopolymer.32.693
- 3) **Podchara Rattanakawin**, Kenji Yoshimoto, Yuta Hikima, Alvin Chandra, Teruaki Hayakawa, Masatoshi Tosaka, Shigeru Yamago, Masahiro Ohshima
“Highly Ordered Nanocellular Polymeric Foams Generated by UV-Induced Chemical Foaming”
ACS Macro Letters (Impact Factor: 6.903, 2020), Vol. 9, Issue 10, pp. 1433-1438, 2020.8
DOI: 10.1021/acsmacrolett.0c00475 (**Chapter 3**)
- 4) **Podchara Rattanakawin**, Kenji Yoshimoto, Yuta Hikima, Shinsuke Nagamine, Yuhan Jiang, Masatoshi Tosaka, Shigeru Yamago, Masahiro Ohshima
“Control of the Cell Structure of UV-induced Chemically Blown Nanocellular Foams by Self-Assembled Block Copolymer Morphology”
Macromolecules (Impact Factor: 5.985, 2020), Submitted (**Chapter 4**)

Peer-reviewed International Conference Proceedings

- 1) **Podchara Rattanakawin**, Weijia Fan, Kenji Yoshimoto, Shigeru Yamago, Masahiro Ohshima, “Chemical Foaming of Self-Assembled Block Copolymers” Proceeding of 29th Annual Meeting of the Japan Society of Polymer Processing, 2018.6
- 2) **Podchara Rattanakawin**, Kenji Yoshimoto, Masahiro Ohshima, “Nanocellular Chemical Foam of Thin Film using Blowing Agent Embedded Polymers”, Proceeding of The SPE FOAMS® 2019 Conference, 2019.10

Presentation

International Conferences

- 1) **Podchara Rattanakawin**, Weijia Fan, Shigeru Yamago, Kenji Yoshimoto, Masahiro Ohshima, “Synthesis of Photocleavable Block Copolymers for UV Induced Foaming”, The 35th International Conference of Photopolymer Science and Technology, 2018.6
- 2) **Podchara Rattanakawin**, Kai Yamamura, Kenji Yoshimoto, Masahiro Ohshima, “Development and Optimization of UV-Induced Chemical Foaming Process”, The 36th International Conference of Photopolymer Science and Technology, 2019.6
- 2) **Podchara Rattanakawin**, Kenji Yoshimoto, Masahiro Ohshima, “Nanocellular Chemical Foam of Thin Film using Blowing Agent Embedded Polymers”, SPE FOAMS® 2019 Conference, 2019.10

Domestic Conferences

- 1) **Podchara Rattanakawin**, Weijia Fan, Kenji Yoshimoto, Shigeru Yamago, Masahiro Ohshima, “Chemical Foaming of Self-Assembled Block Copolymers” 29th Annual Meeting of the Japan Society of Polymer Processing, 2018.6

Awards

- 1) SIIT 4-Years Continuing Scholarship, Sirindhorn International Institute of Technology, Thailand, 2011.4-2015.3
- 2) Certificate of Academic Excellence, Professor Thab Nilanithi Foundation, Thailand, 2012.8
- 3) Academic Excellence Award, The Engineering Institute of Thailand, 2015.3
- 4) MEXT Scholarship, Ministry of Education, Culture, Sports, Science and Technology (MEXT), 2016-2019
- 5) Super Global University Scholarship, Ministry of Education, Culture, Sports, Science and Technology (MEXT), 2019-2022
- 6) Best Poster Award, SPE FOAMS® 2019 Conference, 2019.10